Theoretical Investigations of Prototypical Chemical Systems

by

Jared D. Weidman

(Under the Direction of Henry F. Schaefer III)

Abstract

Quantum chemical studies have been carried out on prototypical gas-phase molecular systems relevant to atmospheric, combustion, and organometallic chemistry. Numerous processes in atmospheric and combustion chemistry produce vinoxy radicals. To understand the fate of these radicals and to provide reliable energies needed for kinetic modeling, we have examined the reactions of the unsubstituted vinoxy radical and the 1-methylvinoxy (acetonyl) radical with O_2 using highly reliable theoretical methods. Geometries were obtained using coupled cluster theory with singles, doubles, and perturbative triple excitations [CCSD(T)]. Energetics were computed to chemical accuracy using the focal point approach involving perturbative treatment of quadruple excitations [CCSDT(Q)] and basis sets as large as cc-pV5Z. In addition, the vinoxy radical + O_2 entrance channel has been studied with multireference methods for the first time. Vinoxy radical + O_2 reactions produce peroxy radicals ($ROO^{\bullet}$), and the unimolecular isomerization pathways of these molecules are explored. Computational studies have also been performed on transition metal carbenes, systems that are widely useful in organometallic chemistry. The prototypical

transition metal methylene complexes of metals in groups 6, 8, and 10 were studied with a variety of DFT functionals. Though none of these complexes has yet been synthesized experimentally, spectroscopic observation of several of these molecules should be possible.

INDEX WORDS: atmospheric chemistry, combustion, coupled cluster theory, focal point approach, organometallics

Theoretical Investigations of Prototypical Chemical Systems

by

Jared D. Weidman

B.S., Calvin College, 2016

A Dissertation Submitted to the Graduate Faculty of the

University of Georgia in Partial Fulfillment of the Requirements for the Degree.

Doctor of Philosophy

Athens, Georgia

2020

Theoretical Investigations of Prototypical Chemical Systems

by

Jared D. Weidman

Major Professor: Henry F. Schaefer III

Committee: Gary E. Douberly

Steven E. Wheeler

Electronic Version Approved:

Ron Walcott

Interim Dean of the Graduate School

The University of Georgia

May 2020

Dedication

In memory of my mother

Contents

Chapter 1

Introduction and Literature Review

1.1 Introduction

For decades, computational quantum chemistry has been a useful tool for theorists and experimentalists alike for understanding and predicting chemical phenomena. The ongoing challenge in computational quantum chemistry is obtaining accurate predictions for increasingly large molecular systems. In general, the computational cost associated with modeling a system increases rapidly as the system size is increased. Computational cost also increases rapidly as the desired accuracy of the computation increases. In order to obtain predictions for large systems without having to perform the expensive computations required, computational chemists often seek to model the full system using a prototype. The prototype system is typically a simplified version of the real-life system where everything has been stripped away except for the most fundamental, chemically-relevant parts.

The subsequent chapters in this text describe computational studies performed on prototypical chemical systems relevant to combustion, atmospheric chemistry, and organometallic chemistry. Each molecular system was chosen in order to model a real-life chemical system while still re-

maining computationally feasible. The following sections in this chapter provide an overview of the relevant theories and methods that pertain to these studies.

1.2 Schrödinger Equation

The goal of computational quantum chemistry is to solve the time-independent Schrödinger equation[1]

$$\hat{H}\Psi = E\Psi. \tag{1.1}$$

where $\hat{H}$ is the Hamiltonian operator, E is the energy, and Ψ is the wavefunction. For a molecule, the Hamiltonian consists of kinetic energy, nuclear-electron attraction, nuclear-nuclear repulsion, and electron-electron repulsion terms. This equation is unsolvable for all but the simplest of systems, so approximations must be made in order to obtain solutions. One common approximation is the Born-Oppenheimer approximation,[2] which separates the nuclear and electronic degrees of freedom. The Born-Oppenheimer approximation introduces a number of useful concepts, including molecular structure and the potential energy surface (PES). A PES is a multidimensional function that describes the energy of the molecular system as a function of the nuclear coordinates. The stationary points (minima, first-order saddle points, etc.) of a PES correspond to reactants, products, and transition states for chemical reactions. Thus, PESs are highly sought after entities for describing chemical reactions.

1.3 Hartree-Fock Theory

The most conceptually basic way of solving the Schrödinger equation is via Hartree-Fock theory.[3] The Hartree-Fock solution to the Schrödinger equation is the minimum-energy solution where the wavefunction consists of a single Slater determinant. A Slater determinant is a mathematical expression for the wavefunction that ensures its antisymmetry. Since electrons are fermions, the Pauli principle states that the wavefunction must be antisymmetric with respect to the exchange of electrons,[4] and the Slater determinant is a form of the wavefunction that ensures this property. This single determinant approximation has the overall effect of treating electron correlation (the instantaneous repulsion of electrons) in an average way. Thus, Hartree-Fock theory is generally only able to obtain qualitative rather than quantitative accuracy for typical molecular systems. However, Hartree-Fock theory is still used today as a starting point for more accurate treatments of electron correlation, such as coupled cluster theory.

1.4 Coupled Cluster Theory

Hartree-Fock theory, in general, is not able to obtain quantitative accuracy for most chemical systems. This is because Hartree-Fock theory does not include a complete treatment of electron correlation. That is, Hartree-Fock theory does not give complete freedom for electrons to instantaneously avoid each other. Methods that build upon Hartree-Fock theory to include more electron correlation are known as post-Hartree-Fock methods. Coupled cluster (CC) theory is one such post-HF method that has found widespread use in computational quantum chemistry due to its high-accuracy capabilities.[5,6]

Coupled cluster theory uses an exponential ansatz for the wavefunction.

$$|\Psi\rangle = e^T |\Phi\rangle \tag{1.2}$$

Here, Φ is some reference wavefunction, usually taken to be the Hartree-Fock wavefunction. The T operator is defined in the following manner:

$$T = T_1 + T_2 + T_3 + \cdots \tag{1.3}$$

where T_1 is the operator for all possible single excitations, T_2 is for double excitations, and so on. If the full T operator is used, all possible excitations are generated, and the result is equivalent to full configuration interaction (FCI). In practice, the T operator is truncated to a particular excitation level, since each additional excitation level adds orders of magnitude to the computational cost. For example, choosing $T = T_1 + T_2$ is coupled cluster with singles and doubles (CCSD), and choosing $T = T_1 + T_2 + T_3$ yields CCSDT. A triples correction to CCSD can be derived using perturbation theory arguments. This method is known as CCSD(T).[7] The CCSD(T) method (with a sufficient basis set such as cc-pVTZ) is hailed as the "gold standard" of quantum chemistry due to its high accuracy and relatively low computational cost compared to other *ab initio* methods. For many chemical systems, particularly organic systems, the CCSD(T) method is capable of achieving "chemical accuracy" (± 1 kcal mol^{-1}).

1.5 Focal Point Analysis

The goal of solving the Schrödinger equation is to obtain the exact electronic energy. Obtaining the exact electronic energy requires including all possible electron correlation (FCI) along with a complete basis set (CBS). In practice, the FCI energy is impossible to compute for all but the

smallest ($\approx$ a dozen electron) systems, and a complete (i.e. infinite) basis set is unattainable. As a result, it is desirous to be able to approximate the FCI/CBS energy using less expensive computations. One way to achieve an accurate approximation of the FCI/CBS energy is the focal point method.[8,9]

The focal point method works by computing several single-point energies using various correlation method and basis set combinations. The electronic energy in the FCI and CBS limits is then obtained by performing extrapolations using these energies. The focal point method takes advantage of the fact that including higher order correlation terms tend to have increasingly small effects on the energy. For most systems, the correction to the CCSD(T) energy provided by CCSDTQ, CCSDTQP, etc. becomes vanishingly small as more excitations are included. Thus, the effect of including higher-order excitations can usually be approximated by computing a correction term with a high-level CC method and a relatively small basis set. In addition, the use of increasingly large basis sets produces increasingly small changes to the energy. In particular, the Dunning-type cc-pVXZ (X = T, Q, 5, etc.) basis sets[10] exhibit this property due to their systematic design. The CBS limit can then be approximated by computing energies with a series of increasingly large basis sets and extrapolating the results to the CBS limit. Many different formulas exist for performing these CBS extrapolations.[11–14] Combining these extrapolation procedures for the FCI and CBS limits provide a useful approximation for the FCI/CBS energy, a computation that is generally infeasible.

1.6 Multireference Methods

Coupled cluster methods such as CCSD(T) are sufficient for accurately describing many chemical reactions. However, there are many chemically-relevant systems for which coupled-cluster meth-

ods break down. Examples of such systems include bond breaking reactions, transition metal complexes, and resonance-stabilized systems. For these systems, a single determinant is insufficient for accurately describing the ground state wavefunction. As seen in Equation 1.2, coupled cluster theory is based on generating excitations from a reference determinant $|\Phi\rangle$. In cases where this reference determinant does not adequately describe the true electron configuration of the system, truncated coupled cluster theory is insufficient. This type of electron correlation that is not adequately described by single-reference methods is called static correlation. Methods that utilize multiple reference determinants in order to better capture static correlation are known as multireference methods. Examples of such methods are complete active space self-consistent field theory (CASSCF),[15] second order multiconfigurational perturbation theory (CASPT2),[16] and multireference configuration interaction (MRCI).[17]

The multireference methods CASPT2 and MRCI are based upon a CASSCF reference wavefunction similarly to how the single reference methods MP2 and CI use HF references. The CASSCF method takes as input a partitioning of the molecular orbitals into 3 distinct subspaces: core, active, and virtual. Core orbitals are always doubly occupied, active orbitals may be occupied or unoccupied, and virtual orbitals are always unoccupied. The CASSCF method then does a full CI computation in the space of the active orbitals. This procedure produces a wavefunction that is a linear combination of determinants, where the most important determinants have a larger contribution. If the active space is chosen appropriately, the CASSCF method provides a good reference wavefunction for which to do further computations with more dynamic correlation. Since the active space is defined by the user prior to the computation, much care is generally needed to ensure the active space chosen is appropriate for the chemistry being modeled.

1.7 Density Functional Theory

While wavefunction-based methods such as coupled cluster theory are appealing due to their potential for sub-chemical accuracy, the computational expense of these methods increases drastically with the size of the system studied. For example, the CCSD(T) method has a formal scaling of $\mathcal{O}(N^7)$, where N is the system size. As a result, the CCSD(T) method becomes intractable for systems with more than ≈50 electrons. Since many chemically-interesting systems (transition metal complexes, pharmaceuticals, biomolecules) are larger than this limit, relatively inexpensive methods are needed that can handle these systems with reasonable accuracy. Density functional theory (DFT) is one such method that has shown to be useful for these kinds of larger systems. As a result, DFT is the most used quantum-chemical method today by a large margin.

The origins of DFT are in the Hohenberg-Kohn theorems of 1964,[18] which, among other things, show that there exists a functional that provides a mapping of the electron density to the total energy of the system. However, while this functional was proved to exist, its exact form is unknown. The typical DFT method used today is Kohn-Sham DFT (KS-DFT).[19] KS-DFT introduces molecular orbitals into the problem, which produces equations that are much easier to solve than equations involving only the electron density. However, KS-DFT does not avoid the problem of not knowing the exact functional.

Many approximate functionals exist that attempt to model the exact functional in KS-DFT. Many of these functionals include empirical parameters chosen to match experimental results. Perhaps the most famous DFT functional is the B3LYP method, which consists of Becke's 1988 exchange functional[20] and the correlation functional of Lee, Yang, and Parr.[21] Other popular functionals include the Minnesota functionals of Truhlar and coworkers (M06, M06-L, M06-2X,

etc.)[22] and the BP86 functional that uses Becke's exchange functional and the correlation functional of Perdew.[23] Because of the empiricism inherent in most DFT functionals, these methods are generally not capable of the accuracy of *ab initio* methods such as coupled cluster theory. However, DFT is still widely used due to its highly favorable accuracy/cost ratio.

Chapter 2

High-Level Theoretical Characterization of the Vinoxy Radical + O_2 Reaction[1]

[1]Reproduced from Weidman, J. D.; Allen, R. T.; Moore, K. B. and Schaefer, H. F. *J. Chem. Phys.* **2018**, *148*, 184308, with the permission of AIP Publishing.

Abstract

Numerous processes in atmospheric and combustion chemistry produce the vinoxy radical ($^{\bullet}CH_2CHO$). To understand the fate of this radical and to provide reliable energies needed for kinetic modeling of such processes, we have examined its reaction with O_2 using highly reliable theoretical methods. Utilizing the focal point approach, the energetics of this reaction and subsequent reactions were obtained with the CCSD(T) method extrapolated to the CBS limit. These extrapolated energies were appended with several corrections including a treatment of full triples and connected quadruple excitations, i.e., CCSDT(Q). In addition, this study models the initial vinoxy radical + O_2 reaction for the first time with multireference methods. We predict a barrier for this reaction of approximately 0.4 kcal mol^{-1}. This result agrees with experimental findings but is in disagreement with previous theoretical studies. The vinoxy radical + O_2 reaction produces a 2-oxoethylperoxy radical, which can undergo a number of unimolecular reactions. Abstraction of a β-hydrogen (a 1,4-hydrogen shift) and dissociation back to reactants are predicted to be competitive to each other due to their similar barriers of 21.2 and 22.3 kcal mol^{-1}, respectively. The minimum-energy β-hydrogen abstraction pathway produces a hydroperoxy radical (QOOH) that eventually decomposes to formaldehyde, CO, and $^{\bullet}OH$. Two other unimolecular reactions of the peroxy radical are α-hydrogen abstraction (38.7 kcal mol^{-1} barrier) and $HO_2^{\bullet}$ elimination (43.5 kcal mol^{-1} barrier). These pathways lead to glyoxal + $^{\bullet}OH$ and ketene + $HO_2^{\bullet}$ formation, respectively, but they are expected to be uncompetitive due to their high barriers.

2.1 Introduction

The vinoxy radical [$^{\bullet}CH_2CHO$] and substituted species such as the acetonyl radical [$^{\bullet}CH_2COCH_3$] are produced during important atmospheric and combustion chemistry processes.[24,25] One impor-

tant process involves alkene ozonolysis in the troposphere. It has been extensively shown that the ozonolysis of alkenes—a process that produces vinoxy radicals as an intermediate—is a primary contributor to nighttime production of $^{\bullet}OH$, an important oxidant.[26–32] The initial cycloaddition of ozone to an alkene yields a primary ozonide that ultimately decomposes to produce a Criegee intermediate (H_2COO). Tautomerization of the Criegee intermediate leads to vinyl hydroperoxide, which then decomposes to a vinoxy radical and $^{\bullet}OH$.[33,34] The latter pathway is the most energetically favorable decomposition of the Criegee intermediate.[24] Alternative pathways for vinoxy radical formation include the reactions of $^{\bullet}OH$ or O_2 with ethylene oxide,[35,36] $^{\bullet}OH$ with acetylene,[37] and $O(^3P)$ with ethylene and propene.[38] Understanding the fate of the vinoxy radical is thus necessary for understanding these impactful processes.

Upon formation, the vinoxy radical may undergo a number of bimolecular reactions with small molecules present in the atmosphere and in combustion engines. The vinoxy radical undergoes a fast reaction with $NO_2^{\bullet}$ that may play a role in atmospheric smog cycles.[39,40] Experiments have shown that the vinoxy radical also reacts readily with $NO^{\bullet}$.[41] However, the most likely oxidation pathway of the vinoxy radical is that with O_2 due to the relative abundance of O_2 in the atmosphere.[42]

In addition to the bimolecular reactions described above, there are two potential pathways for unimolecular decomposition of the vinoxy radical that may compete with the reactions investigated in our study. The first is dissociation into ketene and $H^{\bullet}$, and the second involves an initial rearrangement to form the acetyl radical followed by decomposition to $^{\bullet}CH_3$ and CO. The former pathway is predicted to dominate with a branching ratio of around 2:1.[40] The vinoxy radical is expected to be a short-lived intermediate due to its fast reactions with O_2 and $NO^{\bullet}$ in addition to its proneness for unimolecular decomposition.[43]

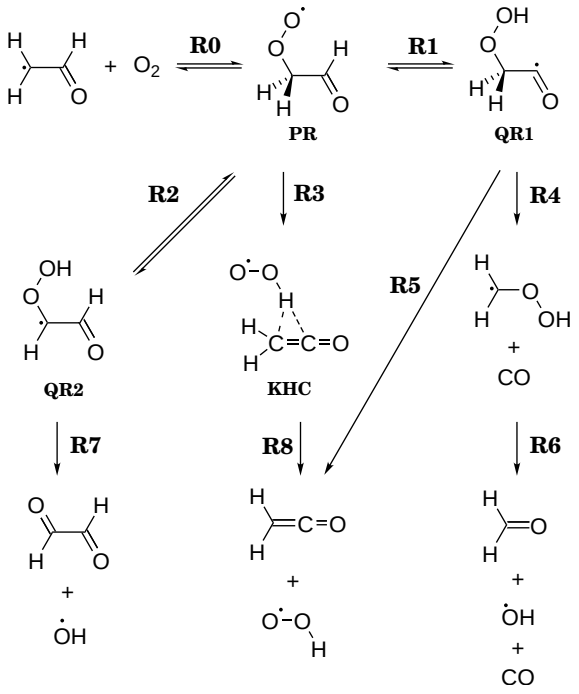

Figure 2.1: Reaction scheme for the vinoxy radical + O_2 system.

2.2 Vinoxy Radical Background

Though this study only considers the simplest of vinoxy radicals, the chemistry discussed herein (Figure 2.1) can be applied to substituted vinoxy radicals with larger R groups. Therefore, the highly reliable results in this study can be helpful for modeling general vinoxy radical oxidation by O_2. In the ground electronic state of the vinoxy radical, the unpaired electron is understood to be primarily localized on the carbon.[44–46] The oxidation of the vinoxy radical begins with the addition of O_2 to the carbon-centered radical, forming an oxoalkylperoxy radical (**PR**).

$$^{\bullet}CH_2CHO + O_2 \longrightarrow \underset{\textbf{PR}}{CHOCH_2OO^{\bullet}} \qquad (\textbf{R0})$$

These oxoalkylperoxy species belong to the very important class of peroxy radicals ($RO_2^{\bullet}$), which are of critical importance to combustion and atmospheric chemistry.[47] Nearly every organic species emitted to the atmosphere forms a peroxy radical at some point in its oxidation, a result of the fast addition of O_2 to alkyl radicals formed from alkane oxidation by $^{\bullet}OH$.[48] Peroxy radicals in the troposphere have been shown to oxidize $^{\bullet}NO_x$ species, leading to the formation of ozone, which is harmful to plant and animal life.[49] During combustion, peroxy radicals may undergo rearrangement to form QOOH, species whose decomposition leads to autoignition due to chain branching.[50]

Once formed, the oxoalkylperoxy radical **PR** can either dissociate back to the reactants or undergo a number of unimolecular reactions. Herein, we consider the three most likely paths. The first involves a hydrogen abstraction from the β-carbon (a 1,4-hydrogen shift) and is labeled reaction **R1**. The β-carbon here is the formyl carbon, and this label follows from the α-carbon being the one bonded to the peroxy moiety. This reaction produces a hydroperoxyalkyl radical (QOOH), labeled **QR1**, as shown below.

$$\underset{\textbf{PR}}{CHOCH_2OO^{\bullet}} \longrightarrow \underset{\textbf{QR1}}{^{\bullet}COCH_2OOH} \qquad (\textbf{R1})$$

Similar to reaction **R1**, species **PR** can also undergo a hydrogen abstraction from the α-carbon (a 1,3-hydrogen shift) to produce a different QOOH radical, **QR2**, via reaction **R2**. Reaction **R2** passes through a highly strained four-membered ring transition state. Therefore, this reaction is expected to be less favorable than **R1** which passes through a five-membered ring transition state.

$$\underset{\textbf{PR}}{CHOCH_2OO^{\bullet}} \longrightarrow \underset{\textbf{QR2}}{CHO^{\bullet}CHOOH} \quad \textbf{(R2)}$$

The third pathway combines β-proton abstraction with heterolytic C–O bond cleavage, ultimately resulting in concerted $HO_2^{\bullet}$ elimination and the formation of ketene. This pathway first produces an intermediary ketene-$HO_2^{\bullet}$ complex (**KHC**) via reaction **R3**.

$$\underset{\textbf{PR}}{CHOCH_2OO^{\bullet}} \longrightarrow \textbf{KHC} \quad \textbf{(R3)}$$

Following the β-hydrogen abstraction reaction **R1**, species **QR1** can undergo C–C bond cleavage to produce $^{\bullet}CH_2OOH$ and CO via reaction **R4**. Alternatively, **QR1** can undergo $HO_2^{\bullet}$ elimination via C–O bond cleavage to produce ketene via reaction **R5**.

$$\underset{\textbf{QR1}}{^{\bullet}COCH_2OOH} \longrightarrow {}^{\bullet}CH_2OOH + CO \quad \textbf{(R4)}$$

$$\underset{\textbf{QR1}}{^{\bullet}COCH_2OOH} \longrightarrow HO_2^{\bullet} + CH_2CO \quad \textbf{(R5)}$$

Reaction **R4** is followed by O–O bond cleavage, reaction **R6**, that leads to $^{\bullet}OH$, formaldehyde, and CO.

$$^{\bullet}CH_2OOH \longrightarrow {}^{\bullet}OH + CH_2O \quad \textbf{(R6)}$$

For the α-hydrogen abstraction pathway, Cleavage of the O–O bond in **QR2** results in the production of glyoxal (OCHCHO) and $^{\bullet}OH$ via reaction **R7**.

$$\underset{\textbf{QR2}}{CHO^{\bullet}CHOOH} \longrightarrow OCHCHO + {}^{\bullet}OH \quad \textbf{(R7)}$$

Finishing the $HO_2^\bullet$ elimination pathway, species **KHC** dissociates into $HO_2^\bullet$ and ketene via reaction **R8**.

$$\mathbf{KHC} \longrightarrow HO_2^\bullet + CH_2CO \qquad (\mathbf{R8})$$

The earliest experiments on the addition of O_2 to the vinoxy radical were conducted in the 1980's by Gutman and Nelson[41] and Lorenz et al.[42] Using laser-induced fluorescence (LIF) to monitor the disappearance of vinoxy radical, rate constants were determined for the vinoxy radical + O_2 reaction as a function of temperature and pressure. The reaction was found to have a small positive pressure dependence and a slightly negative temperature dependence, suggesting a recombination mechanism to form an alkylperoxy radical (**PRa** via **R0**). In addition, $^\bullet$OH was found to be a product of this reaction, suggesting that the peroxy radical formed undergoes rapid isomerization via 1,3- or 1,4-hydrogen shifts followed by unimolecular decomposition.

Using cavity ring-down spectroscopy, Zhu and Johnston found that glyoxal was also produced from the vinoxy radical + O_2 reaction system at room temperature and pressures ranging from 2.5–400 Torr.[36] The rate of appearance of glyoxal was not comparable to the rate of disappearance of the vinoxy radical, suggesting that glyoxal is formed from the decomposition of peroxy radicals produced by reaction **R0**. Using two quasi-static reactors and a discharge flow reactor, Delbos et al. studied this system over larger temperature and pressure ranges (298–660 K, 0.001–50 bar) than had been done previously, and they obtained thermodynamic and kinetic parameters.[51] The $^\bullet$OH radical was once again found to be a product.

2.3 Previous Theoretical Studies

Several theoretical studies exist on the vinoxy radical + O_2 system. Lee and Bozzelli studied the β-hydrogen abstraction and $HO_2^\bullet$ elimination pathways with the CBS-Q method.[52] They found the β-hydrogen abstraction pathway to be favorable over $HO_2^\bullet$ elimination by 28 kcal mol^{-1}. In addition, a barrier of 3.0 kcal mol^{-1} was predicted for the addition of O_2 to the vinoxy radical. Their study examines additional pathways started by reactions **R1** and **R3** through to the products of **R5**, **R6**, and **R8**. Kuwata and coworkers[53,54] studied the oxidation of the unsubstituted vinoxy radical in addition to the analogous reactions of methyl substituted vinoxy radicals. At the CBS-QB3 level of theory, they report a 4.3 kcal mol^{-1} barrier for O_2 addition to the vinoxy radical. They also predicted a 19.5 kcal mol^{-1} barrier for β–hydrogen abstraction, illustrating its favorability over α–hydrogen abstraction, which had a barrier of 39.1 kcal mol^{-1}. From RRKM simulations of reaction **R1**, the Kuwata group predicts that the relative amount of **QR1** versus collisionally-stabilized **PR** falls off slowly with increasing pressure. At 1 atm, around 25% of **PR** molecules are predicted to undergo unimolecular isomerization to **QR1**, indicating that the β-hydrogen abstraction pathway leads to $^\bullet$OH production at these pressures.

Delbos et al.[51] complemented their experimental study on this reaction with an RRKM analysis using computations from several post-HF methods. They predict a barrier for O_2 addition to the vinoxy radical of 4.7 kcal mol^{-1} from the CCSD(T)/cc-pVTZ//QCISD/6-311G(d, p) method. At the same level of theory, the β–abstraction pathway for the peroxy radical is predicted to be favorable over decomposition to reactants by 2.2 kcal mol^{-1}. However, the authors report significant spin contamination of the unrestricted Hartree-Fock references used to treat the vinoxy radical + O_2 transition state, suggesting their post-HF results may not be reliable for this species. Barker and

coworkers studied the vinoxy radical + O_2 surface as it fits into the overall oxidation of acetylene and but-2-yne. Using the B3LYP/6-311G(3df, 2p) method, a 2.7 kcal mol^{-1} barrier was found for peroxy radical formation.[55] The barrier for α–abstraction pathway was predicted to be 41.0 kcal mol^{-1} using ΔG_{298K} values. Their master equation simulations predict that the vinoxy radical formed undergoes rapid unimolecular decomposition to ketene + $^{\bullet}H$ or $^{\bullet}CH_3$ + CO such that peroxy radical formation and its subsequent reactions are negligible.[43]

To understand how the vinoxy radical + O_2 reaction mechanisms interplay with important combustion and atmospheric processes, accurate energetics and kinetics are needed for good modeling. We intend to address these problems using highly accurate *ab initio* computations. Optimized geometries and vibrational frequencies for all species in this system were obtained at the CCSD(T)/ANO1 level, while energies were computed at the CCSD(T)/CBS level of theory. Furthermore, previous theoretical studies on the vinoxy radical + O_2 system reported a barrier ranging from 2.7–12.0 kcal mol^{-1} for the initial addition reaction to form a peroxy radical.[50–55] In contrast, experiments done on this system report minimal barriers of up to 0.7 kcal mol^{-1}.[56] In addition, the reactions of methyl–substituted vinoxy radicals have been shown to be barrierless.[50,56] While the addition of O_2 to the vinoxy radical is a bond forming process that may possess significant multireference character, none of these theoretical studies has utilized multireference methods. Because of this discrepancy between theory and experiment, we have mapped out the potential energy surface of reaction **R0** using a multireference treatment.

2.4 Theoretical Methods

2.4.1 Geometries and Vibrational Frequencies

Optimized equilibrium geometries were obtained with the CFOUR 1.0 electronic structure package[57,58] using coupled-cluster theory with single, double, and perturbative triple excitations [CCSD(T)]. These computations used the ANO1 basis set of Almlöf and Taylor for all atoms. The ANO1 basis set refers to a truncation (H: [4s2p1d]; Li-Ne: [4s3p2d1f]) of the full atomic natural orbital (ANO) basis set.[59] The ANO1 basis set is comparable to the Dunning cc-pVTZ basis set but with more Gaussian primitives, allowing it to be typically more accurate for vibrational frequencies.[60] The 1*s* orbitals of carbon and oxygen atoms were not correlated in all post-HF methods (i.e. a "frozen-core" approximation was used). For open-shell species, a restricted open-shell Hartree-Fock (ROHF) reference[61,62] was used in order to prevent spin contamination. An RHF reference was also used for the few closed-shell species. During geometry optimizations, the RMS force was converged to $10^{-8}\ E_{\mathrm{H}}\ a_0^{-1}$. The HF densities, CC amplitudes, and CC lambda equations were converged to 10^{-10}. Harmonic vibrational frequencies were obtained at the same level of theory using finite differences of the CCSD(T) energy gradients. These frequencies were used to characterize stationary points as minima or transition states. The lowest energy pathways corresponding to transition states were confirmed using the intrinsic reaction coordinate (IRC) method at the UKS-B3LYP/cc-pVTZ level, as implemented in the software package GAMESS 2014.[63,64]

2.4.2 Energetics

Electronic energies relative to the vinoxy radical and O_2 reactants (ΔE_{e}) were computed for all optimized structures using the focal point approach (FPA) of Allen and coworkers.[8,9,65,66] CCSD(T)/CBS

energies were obtained by extrapolating the HF energy and the MP2, CCSD, and CCSD(T) correlation energies, computed using the cc-pVXZ (X = T, Q, 5) basis sets. The Hartree-Fock extrapolations were done using the $E_{\text{HF}} = A + Be^{-CX}$ functional form,[67] and for the correlation energy methods, $E_{\text{corr}} = A + BX^{-3}$ was used.[13] MOLPRO 2010.1 was used for these energy computations.[68]

Several corrections were then added to ΔE_{e} to account for approximations used in the above energy computations. To correct for the frozen core approximation, a core-valence correction (Δ_{CORE}) was performed for each species by computing the difference between the all-electron and frozen-core CCSD(T)/cc-pCVQZ energies. To account for the clamped nuclei approximation, a diagonal Born-Oppenheimer correction (Δ_{DBOC}) was done at the HF/ANO1 level of theory. Scalar relativistic corrections (Δ_{REL}) were computed at the all-electron CCSD(T)/cc-pCVTZ level using a second-order direct perturbation theory (DPT2) approach.[69] To account for the energetic contributions of full triple and perturbative quadruple excitations to these energies, a CCSDT(Q) correction ($\Delta_{\text{T(Q)}}$) was computed as the difference between the CCSDT(Q)/ANO0 and CCSD(T)/ANO0 energies. The CCSDT(Q)/B ansatz for the ROHF references was used, as recommended by Martin.[70] Lastly, to obtain relative enthalpies at zero Kelvin (ΔH_{0K}), a relative zero-point vibrational energy correction (Δ_{ZPVE}), computed at the CCSD(T)/ANO1 level, was appended to the corrected ΔE_{e}. Δ_{CORE} was computed with MOLPRO 2010.1; Δ_{REL}, Δ_{DBOC}, and Δ_{ZPVE} with CFOUR 1.0; and $\Delta_{\text{T(Q)}}$ with MRCC 2015.[71] All single point energies and corrections were converged to 10^{-10} E_{H}.

2.4.3 O_2 Addition Pathway

The pathway for the addition of O_2 to the vinoxy radical was further examined with multireference methods to determine the existence of a barrier for this reaction. More specifically, we

are interested in the ground-state energetics of the reaction: $CHO^{\bullet}CH_2$ ($^2A''$) + O_2 ($^3\Sigma_g^-$) $\rightleftharpoons$ $CHOCH_2OO^{\bullet}$ (^2A). All multireference computations were performed with MOLPRO 2010.1. The reference wave function was computed using the complete active-space SCF method (CASSCF).[72,73] A CASSCF(9 e^-, 6 orb.) space was used, consisting of the occupied π-space (3 e^-, 2 orb.) of the vinoxy radical and the π-space (6 e^-, 4 orb.) of O_2. Constrained optimizations were done by starting with the lowest energy $CHOCH_2OO^{\bullet}$ species and varying the C–O_2 bond length from 1.5 to 3.0 Å in 0.1 Å increments. Geometry optimizations were done using second-order multiconfigurational perturbation theory (CASPT2) and a cc-pVTZ basis set.[10,74–77] A level shift of 0.30 was employed to avoid intruder states. Gradients for these geometry optimizations were converged to 10^{-4} E_H a_0^{-1}.

To obtain more accurate energies for each structure along these curves, we adapt a procedure employed by Klippenstein, Goldsmith, Douberly, and coworkers to study the propargyl peroxy radical.[78,79] The energies were first computed on the optimized CASPT2 structures as a quartet state at the CCSD(T)/cc-pVQZ level of theory ($E^{Qt}_{CC/QZ}$).[80] Unlike the doublet wave function, the high-spin quartet wave function is largely single reference in character, allowing for reliable use of the highly accurate CCSD(T) method. The quartet-doublet splitting energy was then computed using multireference configuration interaction with single and double excitations, and appended by the Davidson correction (MRCISD+Q).[81,82] The cc-pVTZ basis was used for these multireference computations. To obtain energies for the doublet ground state (E^{Db}_{total}), the quartet-doublet splitting energy was subtracted from $E^{Qt}_{CC/QZ}$. These energies were all computed using MOLPRO 2010.1. The full computation can be written as

$$E_{\text{total}}^{\text{Db}} = E_{\text{CC/QZ}}^{\text{Qt}} - \left(E_{\text{MRCI/TZ}}^{\text{Qt}} - E_{\text{MRCI/TZ}}^{\text{Db}} \right). \tag{1}$$

2.5 Results and Discussion

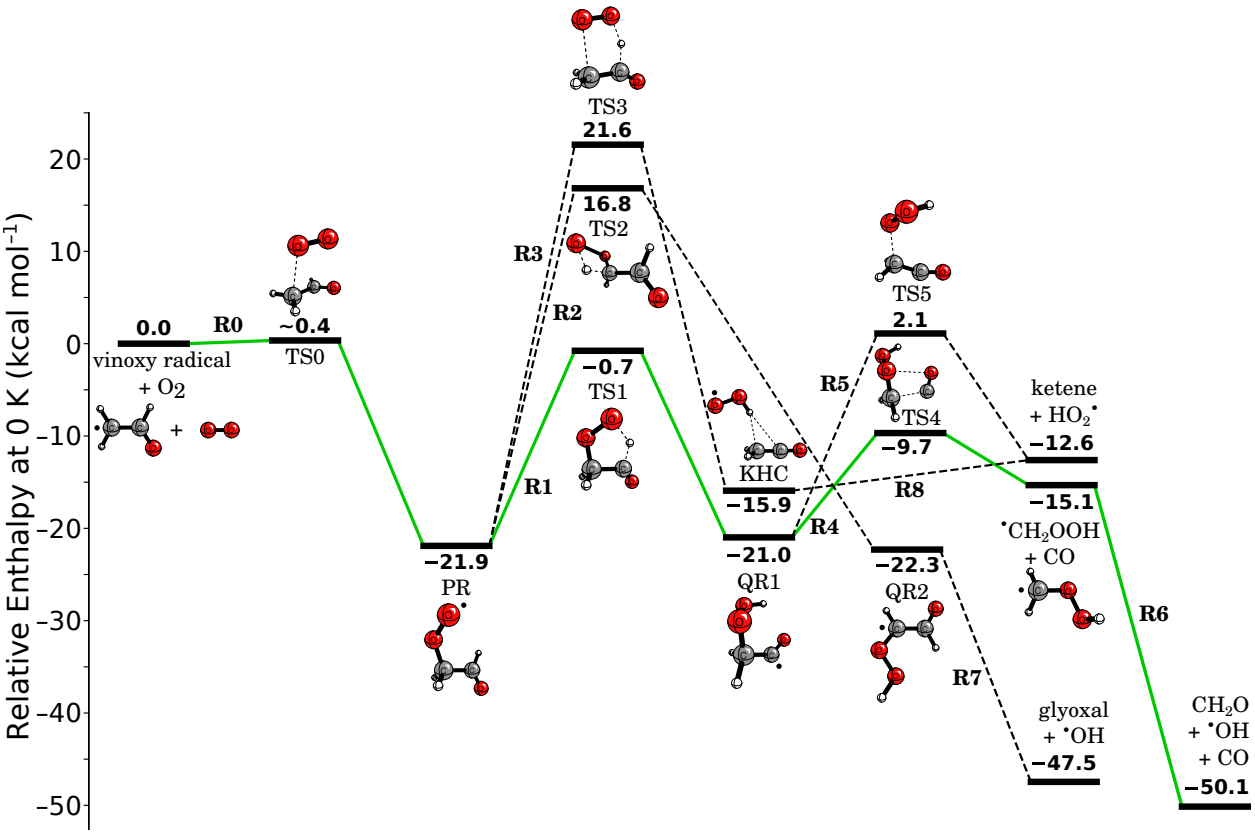

Figure 2.2: Potential energy surface for the full vinoxy radical + O_2 reaction mechanism studied here along with the relevant structures. Energies were computed at the CCSD(T)/CBS level, as shown in Tables A.1-A.19 in the Appendix. The minimum energy pathway is displayed in green. In cases where multiple conformers exist, only the lowest energy conformer is shown.

The potential energy surface for the vinoxy radical reaction with O_2 is shown in Figure 2.2. The focal point tables that demonstrate the convergence of these energies at the CBS limit are given in the Appendix in addition to all of the ZPVE and energy correction values. The relative energies of all species demonstrate convergence to within 0.2 kcal mol^{-1} for all species. Convergence is

also reached at the full CI limit, as evidenced by the $\Delta_{T(Q)}$ values, which are generally less than 0.5 kcal mol^{-1}. This convergence indicates that the results obtained here would not be significantly affected by increasing the basis set size or the amount of dynamic electron correlation included.

2.5.1 Vinoxy Radical + O_2 Reaction Barrier

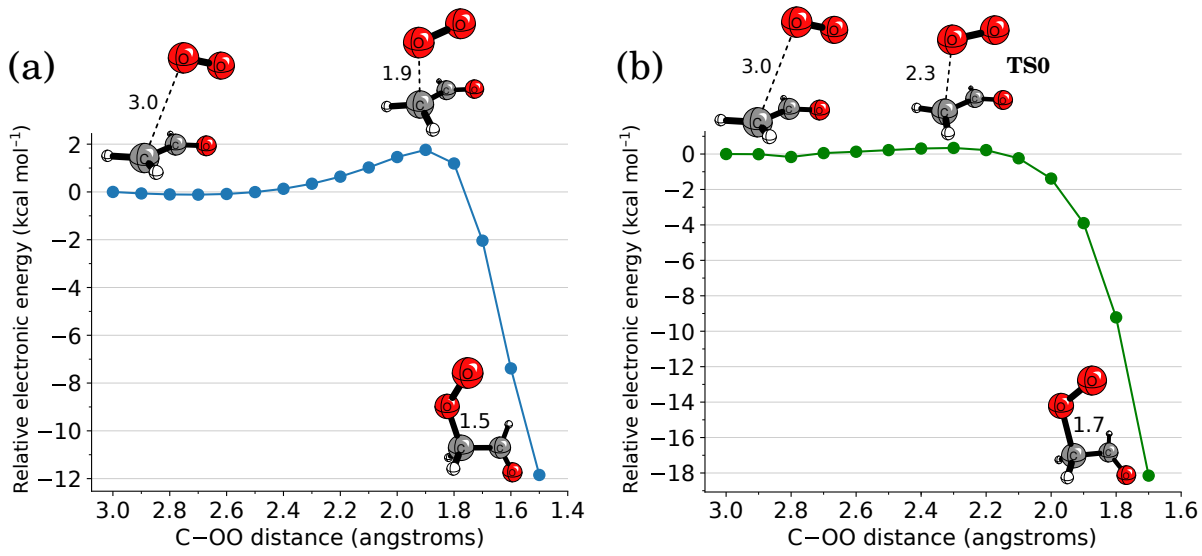

Figure 2.3: Two theoretical methods for constrained optimization energies (kcal mol^{-1}) for the addition of O_2 to the vinoxy radical, forming the 2-oxoethylperoxy radical (**PR**). The C–OO bond distance was varied in 0.1 Å increments while all other geometric parameters were optimized. (a) From CASPT2/cc-pVTZ optimizations; (b) From CCSD(T)/cc-pVQZ + MRCISD+Q/cc-pVTZ (see Equation 1) at the CASPT2 optimized structures. Note this curve (b) ends at 1.7 Å, because we experienced issues converging the quartet state below this distance. Also, note that curve (b) is much flatter than that in part (a).

We have examined reaction **R0** with multireference methods to provide more reliable predictions for the dissociation barrier. Previous theoretical predictions[50–55] on this system span 2.7 to 12.0 kcal mol^{-1} for the value of the barrier height for O_2 addition. Constrained CASPT2/cc-pVTZ optimizations were computed in 0.1 Å increments along the C–OO bond distance over a range from 3.0 to 1.5 Å. Note that the CCSD(T)/ANO1 optimized equilibrium C–OO bond distance for

the 2-oxoethylperoxy radical product (**PR**) is 1.44 Å. This 1.5 Å range of C-OO distances likely contains the transition state, since Kuwata and coworkers reported a transition state structure with a C–OO bond distance of 2.14 Å at the B3LYP/6-311G(2d,d,p) level of theory.[54] The CASPT2 curve is shown in Figure 2.3a.

As O_2 approaches the vinoxy radical, the CASPT2 electronic energy curve reaches a maximum at 1.9 Å. The energy then starts to decrease as the 2-oxoethylperoxy radical (**PR**) is formed. The difference in the energies at the peak (1.9 Å) and at the reactant limit (3.0 Å) suggest a barrier of no more than 2 kcal mol^{-1} for reaction **R0** at the CASPT2 level of theory. The source of this barrier could be attributed to some combination of the C–OO bond breaking, or rotation of the formyl group (as O_2 approaches the vinoxy radical, rotation about the C–C bond orients the formyl group into the staggered conformation of species **PR**). From the opposite viewpoint, any pre-reactive, $CH_2CO \cdots O_2$ van der Waals complex apparently creates only a shallow well that has to be ascended to form the bond.

To obtain a more reliable prediction of the energy difference, energies were computed on the CASPT2 geometries at a higher level of theory using the method from Equation 1. This method involves computing the quartet state at the CCSD(T)/cc-pVQZ level and subtracting from that the quartet-doublet splitting at the MRCISD+Q/cc-pVTZ level to obtain a more accurate doublet energy. The results from these energy computations are shown in Figure 2.3b. A clear barrier peak is not observed since the curve remains flat. The difference in the “peak" (at 2.3 Å) and dissociation limit (3.0 Å) in Figure 2.3b coincide with a barrier of approximately 0.4 kcal mol^{-1}. This result agrees with experimental studies that place the barrier at 0.2–0.7 kcal mol^{-1},[51,56] while strongly contrasting previous theoretical studies.[50–55]

From comparing Figure 2.3a and Figure 2.3b, it is clear that the value of the barrier is very sensitive to the level of theory used. The estimated barrier height using the single-point energy method of Equation 1 is a quarter of the value obtained using CASPT2.

The leading CASSCF(9, 6)/cc-pVTZ coefficients steadily increase as the C–O bond is formed: C_0 = 0.63 at C–OO = 3.0 Å; C_0 = 0.72 at C–OO = 2.5 Å; C_0 = 0.85 at C–OO = 2.0 Å; and C_0 = 0.91 at C–OO = 1.5 Å. This trend indicates that the system has significant multireference character beyond the first few points near the equilibrium geometry of species **PR**. This undoubtedly stems from limitations of single reference methods to treat the breaking and forming of the C–OO bond. Previous theoretical studies[51,54,55] that predict the barrier to be around an order of magnitude larger than the 0.4 kcal mol^{-1} obtained here likely do so because they did not use multireference methods.

2.5.2 Peroxy Radicals

The product of reaction **R0** is the 2-oxoethylperoxy radical (**PR**), of which there are four possible conformers (**PRa**–**PRd**) that lie around 19-22 kcal mol^{-1} below the reactants. These conformers are shown in Figure 2.4. The lowest energy conformer **PRa** has a ΔH_{0K} of -21.9 kcal mol^{-1}. The latter energy is in the middle of the -18.1 to -24.5 kcal mol^{-1} range reported in previous theoretical studies (note that the -18.1 value is at 298 K).[52,55] We assert that the large span of literature results shows why our theoretical work is helpful. Our result aligns well with the -23.2 ± 1 kcal mol^{-1} result concluded from the experiments of Delbos et al.[51]

The four conformers in Figure 2.4 are distinguished by the orientation of the formyl group and the rotation of the peroxy moiety, the latter of which dictates the molecular symmetry. The formyl group can be rotated such that the oxygen atom is oriented *cis* or *trans* to the peroxy group.

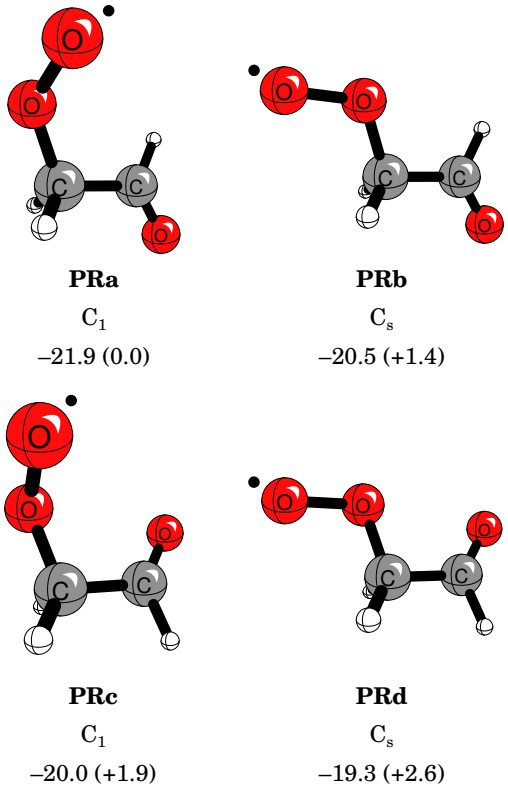

Figure 2.4: Conformers of the peroxy radical (**PR**) formed from the vinoxy radical + O_2 addition (**R0**). The ΔH_{0K} values relative to separated vinoxy radical + O_2 are given, and ΔH_{0K} relative to the lowest energy conformer (**PRa**) are provided in parentheses. See Tables A.1-A.4 in the Appendix for the computed energies. All energies in kcal mol^{-1}.

In terms of symmetry, the peroxy moiety can be rotated such that it lies in a plane of symmetry or out of the plane. These rotations produce C_s and C_1 symmetry, respectively. The unpaired electron is oriented perpendicular to the plane of the C–O–O moiety and primarily localized on the terminal oxygen. For the C_s conformers, this structure corresponds to the $^2A''$ electronic state, and the C_1 conformers are of ^2A symmetry. Of these two conformational degrees of freedom, C_1 symmetry generally is lower in energy than the corresponding C_s conformer, and the *trans* location of the aldehyde oxygen atom is lower in energy than the *cis* counterpart (likely because there is less steric repulsion). The overall lowest energy conformer is then the *trans* C_1 peroxy

radical labeled **PRa**. The fact that the four conformers all lie within a few kcal mol^{-1} of each other indicates that the peroxy radical can interconvert between conformers pretty readily.

The peroxy radical can undergo a number of unimolecular reactions (**R1**–**R3**) in addition to simply dissociating back to the reactants (**R0**). The barriers for each of these processes are given in Table 2.1, and the optimized structures for the transition states for reactions **R1**–**R3** are shown in Figure 2.5. The next three sections explore how the peroxy radical proceeds through these transition states and what mechanisms occur afterwards.

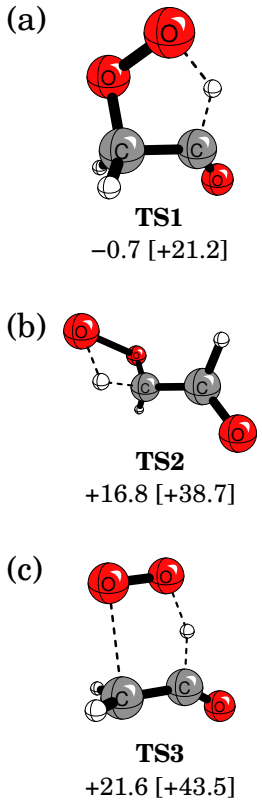

Figure 2.5: Transition states corresponding to the (a) β–hydrogen abstraction (**R1**), (b) α–hydrogen abstraction (**R2**), and (c) $HO_2^\bullet$ elimination (**R3**) reactions of the peroxy radical **PR**. The ΔH_{0K} values relative to separated vinoxy radical + O_2 are given. Values in brackets are barriers with respect to the lowest energy peroxy radical conformer, **PRa**. See Tables A.5-A.7 for computed energies. All energies in kcal mol^{-1}.

Table 2.1: Barriers for reactions involving peroxy radical **PR** (kcal mol^{-1}). Theoretical energies are at 0 K and include ZPVE corrections.

Source	Method	**R0**	**R1**	**R2**	**R3**
This work	CCSD(T)/CBS	22.3	21.2	38.7	43.5
Lee & Bozzelli[52]	CBSQ	27.3	21.2	···	45.5
Kuwata et al.[54]	CBS-QB3	27.3	19.5	39.1	···
Barker et al.[55]	B3LYP/6-31G(3df,2p)	20.7	19.9	40.6	···
Delbos et al.[51]	Experiment	23.4 $\pm$1	19.6 $\pm$1	···	···

2.5.3 β-Hydrogen Abstraction Pathway

The lowest energy barrier corresponds to β-hydrogen abstraction (**R1**) at 21.2 kcal mol^{-1}. The transition state structure (**TS1**) is shown in Figure 2.5a. We predict that peroxy radical dissociation (**R0**) has a similar barrier of 22.3 kcal mol^{-1}. Therefore, these pathways are expected to compete with each other. These results are in contrast with those of Kuwata and coworkers who predict the dissociation barrier to be almost 8 kcal mol^{-1} higher than that of β-hydrogen abstraction at the CBS-QB3 level.[54] Over half of this difference in energy can be attributed to the C–OO dissociation barrier that is 4.3 kcal mol^{-1} above that of the reactants predicted by Kuwata and coworkers. The rest is the 2 kcal mol^{-1} difference in our barrier height to **TS1**. In their RRKM/master equation simulations, Kuwata and coworkers predict 100% conversion of the 2-oxoethylperoxy radical (**PR**) to the hydroperoxy radical **QR1** at 0 torr. The relative yield of **QR1** slowly decreases with increasing pressure to 25% at 760 torr. The **PR** and **QR1** yield curves intersect at around 300 torr, after which collisional stabilization of **PR** becomes favorable over conversion to **QR1** through **TS1**. These results may vary significantly if the barriers for reactions **R1** and **R0** are similar, as our work predicts. Since dissociation is also the entropically favorable pathway versus β-hydrogen abstraction, **R0** may be more predominant at higher temperatures than previous studies suggest.

Our predicted barrier height of 21.2 kcal mol^{-1} for **R1** is among the highest of the values reported in the literature (see Table 2.1). This value is about 1.6 kcal mol^{-1} higher than the 19.6 ± 1 kcal mol^{-1} found experimentally by Delbos and coworkers.[51]

The ΔH_{0K} value of −0.7 kcal mol^{-1} reported for transition state **TS1** excludes an unphysically large Δ_{DBOC} of 0.9 kcal mol^{-1}. All other Δ_{DBOC} values computed here were at or less than 0.1 kcal mol^{-1}. This large correction demonstrates a breakdown of the Born-Oppenheimer approximation for this structure and may be an artifact of a nearby surface crossing.[83] Theoretical studies on ethyl, propyl, and tert-butyl radical + O_2 systems report similarly large Δ_{DBOC} values for the corresponding β-hydrogen abstraction transition states due to nearby conical intersections.[84–86]

The β-hydrogen abstraction reaction of the 2-oxoethylperoxy radical (**PR**) produces a hydroperoxy radical (QOOH), **QR1**. The unpaired electron of **QR1** is localized on the β-carbon. There are four conformers of **QR1**, labeled **QR1a–QR1d**, and they are shown in Figure 2.6. This study is the first to report four conformers for **QR1**. Kuwata and coworkers previously found two conformers that correspond to our **QR1a** and **QR1c**.[54] Other theoretical studies report only a single conformer that is analogous to our **QR1b** and therefore incorrectly assumed to be the lowest energy conformer.[52,55] Our finding for the relative energy of **QR1c** being 1.9 kcal mol^{-1} above **QR1a** agrees reasonably with the CBS-QB3 value of 1.7 kcal mol^{-1} obtained by Kuwata and coworkers.

The ΔH_{0K} values for **QR1** range from −21.0 kcal mol^{-1} for the lowest energy conformer to −18.8 kcal mol^{-1} for the highest. The four **QR1** conformers can be classified based on the orientation of the formyl group and the orientation of the –OOH hydrogen. The formyl group can be oriented *cis* or *trans* to the hydroperoxy moiety, and the hydrogen can be oriented *toward* or *away* from the formyl group. The two lowest energy conformers **QR1a** and **QR1b** exhibit orientations of

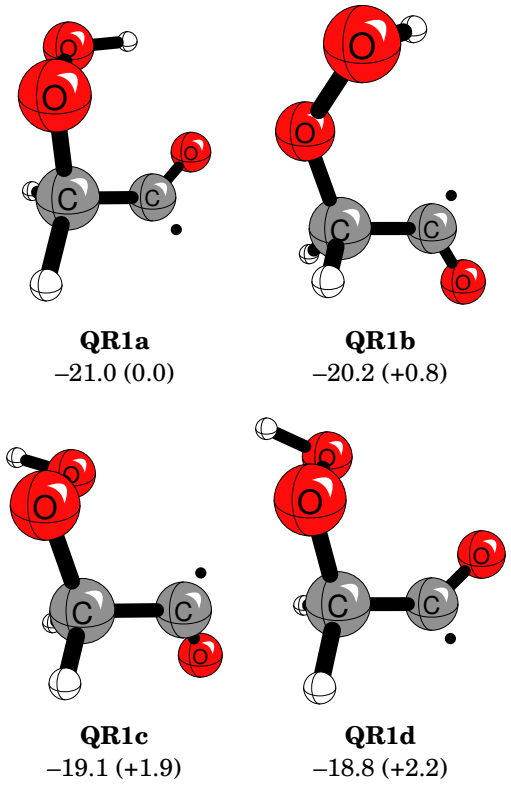

Figure 2.6: Conformers of the hydroperoxy radical **QR1** formed from reaction **R1**. The ΔH_{0K} values relative to separated vinoxy radical + O_2 are given, and ΔH_{0K} relative to the lowest energy conformer (**QR1a**) are provided in parentheses. See Tables A.8-A.11 for the computed energies. All energies in kcal mol^{-1}.

the hydroperoxy hydrogen toward the formyl group. These conformations introduce energy lowering interactions between the hydroperoxy hydrogen and an atom from the formyl group. For **QR1a** there is an O–H$\cdots$O hydrogen bond with a distance 2.36 Å between the formyl oxygen and hydroperoxy hydrogen. For **QR1b**, there is an attractive O–H$\cdots$*n* interaction between the hydroperoxy hydrogen and the unpaired electron on the formyl carbon. Similar to the four peroxy radical conformers, the **QR1** conformers all are within a few kcal mol^{-1} of each other. Therefore, the conformers can be expected to readily interconvert. The lowest energy conformer here (–21.0 kcal mol^{-1}) is a few kcal mol^{-1} higher in energy than the –21.9 kcal mol^{-1} reported by Kuwata and coworkers and the –23.2 reported by Lee and Bozzelli for the lowest energy conformer.[52,54] Barker and coworkers' less reliable prediction of –14.0 kcal mol^{-1} for the relative energy of **QR1** is significantly higher than energies obtained in ours and other theoretical studies.[55]

Species **QR1** (see Figure 2.6) may additionally undergo further unimolecular reactions. One pathway involves the elimination of CO (**R4**) via **TS4**, which has a barrier of 11.3 kcal mol^{-1}. Another pathway involves $HO_2^{\bullet}$ elimination (**R5**) via **TS5**, resulting in the production of ketene and has a barrier of 23.0 kcal mol^{-1}. The transition states for these reactions are shown in Figure 2.7. Reaction **R4** is expected to be much more competitive compared to **R5**, due to having an 11.7 kcal mol^{-1} lower barrier. As such, only the CO elimination pathway is expected to contribute. **R4** produces the short-lived $^{\bullet}CH_2OOH$ (Figure 2.8) which quickly decomposes to form formaldehyde and $^{\bullet}OH$ (**R6**). Kuwata and coworkers found a transition state at the CBS-QB3 level for reaction **R6** that is 0.7 kcal mol^{-1} *lower* in energy than the reactants for this reaction.[54] Their result may arise from errors in the DFT treatments used for this bond breaking process. This "transition state energy" suggests that **R6** is essentially barrierless. Zhu and Johnston have observed formaldehyde as a product of the overall vinoxy radical + O_2 system,[36] and $^{\bullet}OH$ was observed as a product by

Gutman and Nelson[41] and by Lorenz et al.[42] Indeed our results show that formaldehyde and $^{\bullet}$OH are products of the minimum-energy pathway for the vinoxy radical + O_2 system. Formaldehyde, carbon monoxide, and $^{\bullet}$OH together lie 29.2 kcal mol^{-1} below **QR1a** and 50.1 kcal mol^{-1} below the original vinoxy radical and O_2 reactants. These three molecules appear to be the major kinetic and thermodynamic products of this system.

The $HO_2^{\bullet}$ elimination pathway from **QR1** via **TS5** lies 11.7 kcal mol^{-1} higher than the minimum energy pathway's **TS4** but still only 2.7 kcal mol^{-1} higher than **TS1**. Thus, a peroxy radical with enough energy to overcome the **R1** barrier could reasonably be expected to also overcome that of **R5**. Reaction **R4** is still a much more favorable pathway than **R5** due to the significantly lower barrier.

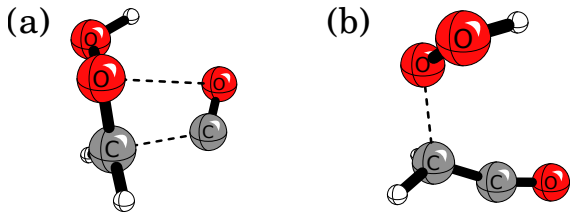

TS4
–9.7 [+11.3]

TS5
+0.4 [+23.0]

Figure 2.7: Optimized structures of the transition states for reactions (a) **R4** and (b) **R5**. The ΔH_{0K} values relative to separated vinoxy radical + O_2 are given in kcal mol^{-1}. Values in brackets are barriers with respect to **QR1a**, the lowest energy conformer of the hydroperoxy radical produced from **R1**. See Tables A.12-A.13 for the computed energies.

2.5.4 α—Hydrogen Abstraction Pathway

The **R2** reaction barrier through **TS2** is 38.7 kcal mol^{-1}, placing it 17.5 kcal mol^{-1} higher than that for **R1** and 16.8 kcal mol^{-1} higher than separated vinoxy radical + O_2. This pathway is therefore not expected to contribute except in cases of high temperature. The transition state (**TS2**) for this reaction involves a highly strained four-membered ring structure. This ring strain is the

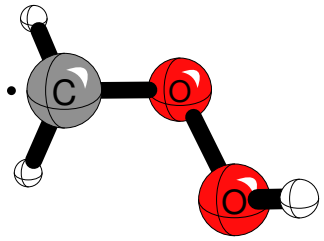

$^{\bullet}CH_2OOH$
–15.3

Figure 2.8: Optimized structure for the product of the CO elimination reaction **R4**, which will likely dissociate quickly into formaldehyde and $^{\bullet}OH$. The ΔH_{0K} value for separated $^{\bullet}CH_2OOH$ + CO relative to separated vinoxy radical + O_2 is given in kcal mol^{-1}. See Table A.14 in the Appendix for the computed energy.

primary reason the barrier for this reaction is so much higher in energy than **TS1**, which exhibits a five-membered ring structure. The product of **R2**, the QOOH radical **QR2**, has a ΔH_{0K} of −22.3 kcal mol^{-1}, which is 1.3 kcal mol^{-1} below **QR1a**. Despite the thermodynamic favorability of **QR2** relative to **QR1**, it is kinetically limited because of the relatively high barrier for α-hydrogen abstraction. **QR2** has one conformer, a planar C_s structure, shown in Figure 2.9. The unpaired electron of **QR2** is localized on the α-carbon and out of the plane of the molecule, giving it a $^2A''$ ground state. Other conformers of **QR2** found preliminarily at lower levels of theory (M06-2X/def2-TZVP) initially yielded a C_1 structure. However, they eventually converge to this single C_s conformer at the CCSD(T)/ANO1 level of theory.

Other theoretical studies report only one conformer of **QR2** as well..[54,55] Kuwata and coworkers predict **QR2** to have a relative energy of −23.6 kcal mol^{-1} compared to the vinoxy radical + O_2 reactants at the CBS-QB3 level. Their minimum energy structure is C_1 symmetric due to a rotation about the C–OOH bond that places the –OH group out of the plane of the rest of the molecule. Barker and coworkers predict a relative energy of (−24.4 kcal mol^{-1}) for **QR2** with the B3LYP/6-

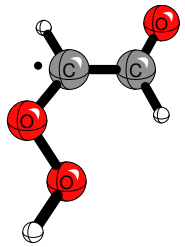

QR2
–22.3

Figure 2.9: Optimized structure for the QOOH radical product of reaction **R2**. The ΔH_{0K} value relative to separated vinoxy radical + O_2 is given in kcal mol^{-1}. See Table A.15 for the computed energy.

31G(3df,2p) method. They report a planar C_s symmetric structure oriented in such a way that the –OOH hydrogen and the formyl oxygen are rotated to be close to each other. We expect a conformer with this orientation to have O–O repulsion that would raise this conformer's energy above **QR2**. In general, we do not rule out the possibility that more conformers exist for this molecule.

QR2 can undergo O–O bond fission to produce glyoxal and $^{\bullet}OH$. Herein, we have assumed that the O–O bond of **QR2** breaks similarly to that of the $^{\bullet}CH_2OOH$ species discussed in Section 2.5.3. Glyoxal has been experimentally observed by Zhu and Johnston as being produced in the vinoxy radical + O_2 reaction.[36] While the pathway through **R2** leads to glyoxal, the high **R2** barrier indicates that the glyoxal observed in the experiments is likely produced from other secondary reactions of the vinoxy radical + O_2 system.

2.5.5 $HO_2^{\bullet}$ Elimination Pathway

The highest energy unimolecular pathway for the peroxy radical considered here is the $HO_2^{\bullet}$ elimination pathway via **TS3** (see Figure 2.5c). This reaction has a barrier of 43.5 kcal mol^{-1},

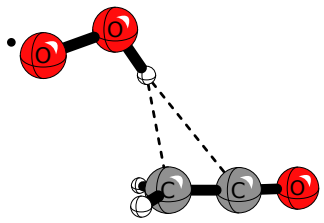

KHC
–15.9

Figure 2.10: Optimized structure for the product of reaction **R3**, the ketene-$HO_2^\bullet$ complex (**KHC**). This complex dissociates to ketene and $HO_2^\bullet$, which together lie 3.3 kcal mol^{-1} above the complex. The ΔH_{0K} value relative to separated vinoxy radical + O_2 is given in kcal mol^{-1}. See Table A.16 for the computed energy.

22.2 kcal mol^{-1} above that for **R1** and 4.7 kcal mol^{-1} above that for **R2**. Hence, like **R2**, this pathway would only contribute at higher temperatures. **TS3** takes a C_s structure wherein there is a simultaneous β–hydrogen abstraction and C–OO bond fission. The product of reaction **R3**, the ketene–$HO_2^\bullet$ complex (**KHC**) has a ΔH_{0K} of –15.9 kcal mol^{-1}. This intermediary **KHC** is characterized by an intermolecular OH/π bond between the $HO_2^\bullet$ hydrogen and the C=C π bond of ketene. This interaction lowers the energy of this molecule 3.3 kcal mol^{-1} below that of fully dissociated ketene and $HO_2^\bullet$. While it may be expected that a complex between $HO_2^\bullet$ and ketene would involve an O–H$\cdots$O hydrogen bond, the O–H$\cdots\pi$ hydrogen bonded **KHC** intermediate was the species located by our IRC computations. Considering the relatively high barriers for this $HO_2^\bullet$ formation pathway, as well as the pathway discussed in Section 2.5.3, $HO_2^\bullet$ elimination from the vinoxy radical + O_2 system is overall very unlikely to occur.

2.6 Conclusions and Outlook

We have studied at high levels of theory the mechanism for the reaction of O_2 with the vinoxy radical. Geometries and vibrational frequencies were obtained at the CCSD(T)/ANO1 level. Energies were obtained to within chemical accuracy through the use of CCSD(T)/CBS energies appended with corrections for quadruple excitations. The barrier for the initial O_2 addition was studied for the first time using multireference methods. Our predicted barrier of approximately 0.4 kcal mol^{-1} is consistent with the experimental results available for the unsubstituted and methyl-substituted vinoxy radicals. This result is in contrast to other theoretical studies on this system, which predict barriers of 2-12 kcal mol^{-1}. A 2-oxoethylperoxy radical is formed from O_2 addition to vinoxy radical. Subsequently, β-hydrogen abstraction (21.2 kcal mol^{-1} barrier, compared to 19.6 from experiment[51]) is expected to be the most energetically favorable pathway, although it also is expected to be competitive to dissociation to reactants (22.3 kcal mol^{-1} barrier). The β-hydrogen abstraction pathway will then most likely lead to the production of formaldehyde, $^{\bullet}$OH, and CO. The competitiveness between β-hydrogen abstraction and dissociation disagrees with previous theoretical studies that predict β-hydrogen abstraction to be favorable by 6–8 kcal mol^{-1}.[52,54]

The RRKM/master equation results of Kuwata and coworkers that predicted significant β-hydrogen abstraction at pressures up through 1 atm will be affected by these results. Expected yields of $^{\bullet}$OH from this system would be significantly reduced if the 2-oxoethylperoxy radical is as prone to dissociation as we predict. The $\alpha-$hydrogen abstraction and $HO_2^{\bullet}$ elimination pathways are not competitive—except in cases of extremely high temperature—due to both having barriers around 40 kcal mol^{-1} above the peroxy radical. These results are in agreement with conclusions from previous experiments that glyoxal is not a primary product of the vinoxy radical + O_2 reaction.

The results obtained in this study should be essential for further kinetic studies on the vinoxy radical system that require reaction barriers to be known to chemical accuracy.

Though elimination of $HO_2^\bullet$ from the peroxy radical is an extremely unfavorable pathway for the vinoxy radical system, $HO_2^\bullet$ elimination pathways are generally preferable for alkyl radical systems.[85] If an α-hydrogen from the vinoxy radical were substituted for a methyl group, a concerted $HO_2^\bullet$ elimination using one of the methyl hydrogens would be possible. This $HO_2^\bullet$ elimination pathway would be analogous to an $HO_2^\bullet$ elimination from an alkyl system, meaning that this pathway could potentially compete more favorably with β-hydrogen abstraction than would $HO_2^\bullet$ elimination from the aldehydic hydrogen. This reaction can bee seen in methyl-substituted vinoxy species, such as the 2-methylvinoxy radical. This additional pathway for the vinoxy radical has so far not been studied in the literature.

Chapter 3

Energetics and Mechanisms for the Acetonyl Radical + O_2 Reaction[1]

[1]Reproduced from Weidman, J. D.; Turney, J. M.; and Schaefer, H. F. *J. Chem. Phys.* **2020**, *152*, 114301, with the permission of AIP Publishing.

Abstract

The acetonyl radical ($^{\bullet}CH_2COCH_3$) is relevant to atmospheric and combustion chemistry due to its prevalence in many important reaction mechanisms. One such reaction mechanism is the decomposition of Criegee intermediates in the atmosphere that can produce acetonyl radical and OH. In order to understand the fate of the acetonyl radical in these environments and to create more accurate kinetics models, we have examined the reaction system of acetonyl radical with O_2 using highly reliable theoretical methods. Structures were optimized using coupled cluster theory with singles, doubles, and perturbative triples [CCSD(T)] with an atomic natural orbital (ANO0) basis set. Energetics were computed to chemical accuracy using the focal point approach involving perturbative treatment of quadruple excitations [CCSDT(Q)] and basis sets as large as cc-pV5Z. The addition of O_2 to acetonyl radical produces the acetonylperoxy radical, and multireference computations on this reaction suggest it to be barrierless. No submerged pathways were found for the unimolecular isomerization of the acetonylperoxy radical. Besides dissociation to reactants, the lowest energy pathway available for the acetonylperoxy radical is a 1-5 H shift from the methyl group to the peroxy group through a transition state that is 3.3 kcal mol^{-1} higher in energy than acetonyl radical + O_2. The ultimate products from this pathway are the enol tautomer of acetonyl radical along with O_2. Multiple pathways are considered that lead to OH formation; however, all of these pathways are predicted to be energetically inaccessible excepting high temperatures.

3.1 Introduction

The acetonyl radical ($^{\bullet}CH_2COCH_3$), also known as the 1-methylvinoxy radical, is an important intermediate in atmospheric and combustion chemistry processes. In the atmosphere, its parent acetone is one of the most abundant organic gasses.[87–89] Besides photolysis, the major sink of

acetone is reaction with OH, which produces the acetonyl radical and H_2O.[87,90,91] Vinoxy radicals such as acetonyl radical are also produced from ozonolysis of alkenes.[26,28] The ozonolysis of alkenes produces Criegee intermediates, whose lowest energy decomposition pathway forms vinoxy radicals.[24,92] In combustion, vinoxy radicals are also produced from the oxidation of alkenes and alkynes.[35,37,38,93–95] In both the atmospheric and combustion environments, reactions with O_2 are likely. An accurate understanding of the reaction of O_2 with acetonyl radical is essential for understanding the fate of the acetonyl radical in these environments.

The acetonyl radical has two possible resonance structures, one with the unpaired electron on the primary carbon and the second where the unpaired electron is on the oxygen. Experimental findings indicate that acetonyl radical exhibits the reactivity of a carbon-centered radical.[96] While some disagreement exists in the literature regarding the degree of resonance stabilization in acetonyl radical,[96–99] the most recent theoretical studies predict a resonance stabilization of 4-5 kcal mol^{-1}.[100,101] In a similar manner as in alkyl radical + O_2 reactions, O_2 can add to the carbon radical center to produce acetonylperoxy radical ($^{\bullet}OOCH_2COCH_3$) via reaction **R0**.

$$^{\bullet}CH_2COCH_3 + O_2 \longrightarrow \underset{\textbf{PR}}{^{\bullet}OOCH_2COCH_3} \qquad \textbf{R0}$$

Experiments[56,96,102–104] have found that reaction **R0** is essentially a radical-radical recombination process, but this reaction is slower than the analogous alkyl radical reactions such as *n*-propyl + O_2. This difference in reaction rate has been explained to be due to the resonance stabilization of acetonyl radical.[56,96]

The acetonylperoxy radical (**PR**) is a member of an important class of compounds, peroxy radicals ($ROO^{\bullet}$), that play a crucial role in atmospheric and combustion chemistry.[24,25,48,105,106]

In particular, peroxy radicals can undergo intramolecular hydrogen shift reactions to form hydroperoxyalkyl radicals (QOOH). These elusive QOOH species have been shown to be important in autoignition and aerosol formation.[25,48,107] Many properties and reactions of **PR** have been reported in the literature.[102,108–114] Herein, only unimolecular isomerizations from **PR** are considered. The existing experimental studies have not reported any products stemming from reactions of **PR**.[56,96,102–104] These studies have all been performed at room temperature, so no low-lying isomerization pathways are expected for the acetonyl radical + O_2 system. In contrast, the unsubstituted vinoxy radical has been found to lead to OH formation upon reacting with O_2.[42,51]

The corresponding reactions of the unsubstituted[115] and 2-methylvinoxy[116] with O_2 have recently been examined theoretically, and the reader is directed to those references for further information on these closely related systems. In the parent vinoxy and 2-methylvinoxy radical systems, the lowest energy isomerization pathway of the peroxy radical is a 1-4 hydrogen shift from the formyl group to the peroxy group. The computed enthalpies at 0 Kelvin for these systems placed the transition state around 1 kcal mol^{-1} below the separated reactants. No other submerged transition states stemming from the peroxy radicals were found for either system, which indicate the system will have a strong preference towards this 1-4 H shift pathway in tropospheric and low-temperature combustion environments. For the acetonyl radical + O_2 system, the corresponding hydrogen shift reaction is not available as there is no formyl hydrogen available for abstraction. This lack of a relatively weakly-bound formyl hydrogen in the acetonyl peroxy system raises the question of whether an accessible isomerization pathway exists for this system.

The only existing theoretical studies on the acetonyl + O_2 system were published between 2005 and 2008 and used a variety of DFT and composite methods. In 2005, Kuwata et al. studied the vinoxy, acetonyl, and 2-methylvinoxy radicals' reactions with O_2 using the CBS-QB3 method.[54]

They report a barrier of 2.4 kcal mol^{-1} in enthalpy at zero Kelvin for the entrance channel addition of O_2 to acetonyl to form acetonylperoxy radical. The lowest energy isomerization pathway of the acetonylperoxy radical was found to be a 1-5 H shift from the methyl group. The transition state for this reaction was computed to be 1.1 kcal mol^{-1} higher than the energy of the reactants, and 26.1 kcal mol^{-1} from the peroxy radical. This reaction leads to the formation of a hydroperoxyacyl radical (QOOH), but further reactions of this species were not considered, due to the relatively high barrier of the 1-5 H shift reaction from the peroxy radical. Master equation simulations found isomerization of the acetonylperoxy to be negligible at all pressures studied. In contrast, the vinoxy and 2-methylvinoxy radicals were found to have submerged hydrogen shift pathways stemming from their analogous peroxy radical, and these lower barriers led to significant isomerization of the analogous peroxy radicals at 1 atm.

Hassouna et al. in 2006 studied the acetonyl + O_2 system using the B3LYP method with a 6-311+G(3df,2p) basis set.[103] The entrance channel was computed to have a barrier of around 2.0 kcal mol^{-1} of enthalpy at 298.15 K. A direct hydrogen abstraction reaction from acetonyl by O_2 to form $HO_2^{\bullet}$ and CH_2COCH_2 was predicted to have a much higher barrier (20+ kcal mol^{-1}), and this pathway was not considered further. The 1-5 H shift reaction of the acetonylperoxy radical was predicted to have a substantial barrier that lies 7.3 kcal mol^{-1} above acetonyl + O_2. Further unimolecular reactions of the hydroperoxyacyl radical formed by this reaction were not studied, likely due to this high barrier of formation.

Kovács et al. performed computations on the acetonyl + O_2 system using a variety of methods including BB1K, B3LYP, QCISD, and QCISD(T) with basis sets up to cc-pVTZ.[104] While no specific energies or structures are given, they report a “low, but well-defined" barrier for the addition of O_2 to acetonyl. The barrier for the 1-5 H shift reaction of the acetonylperoxy radical was com-

puted to be higher relative to reactants than the entrance channel barrier. Further unimolecular isomerizations of the hydroperoxyacyl radicals were studied, and the lowest energy pathway was computed to be a hydrogen shift from the peroxy group to the ketone oxygen, producing the enol-acetonylperoxy radical. A C-OO bond cleavage leads to the production of enol-acetonyl radical + O_2, and these products were predicted to be higher in energy than the acetonyl + O_2 reactants. Other unimolecular reactions of the hydroperoxyacyl radical were an OH shift to the $^{\bullet}CH_2$ to form the 2-hydroxy-acetyl-methoxy radical, and an O–O cleavage reaction to form 3-oxetanone and OH.

El-Nahas et al. studied the acetonyl radical + O_2 system using the CBS-QB3 method.[112] They report a submerged barrier for the addition of O_2 to acetonyl of around –0.7 kcal mol^{-1} of enthalpy at 298.15 K. The El-Nahas finding of a submerged barrier for this reaction is the only theoretical study to do so. In addition, they report a submerged barrier for the 1-5 H shift reaction stemming from the acetonylperoxy radical, again being the only theoretical study to do so. The lowest energy pathway of the hydroperoxyacyl radical formed was predicted to be the O–O cleavage reaction to produce 3-oxetanone, and this reaction was found to have a barrier around 9.8 kcal mol^{-1} higher than reactants. Additional reactions of the hydroperoxyacyl radical studied include the OH transfer reaction to form 2-hydroxy-acetyl-methoxy, and a C–C cleavage reaction that leads to ketene, formaldehyde, and OH. The H-shift reaction from the hydroperoxy moiety to the ketone oxygen was not studied.

There is currently no consensus in the literature regarding the qualitative nature of key features of the acetonyl + O_2 potential energy surface. The transition state for O_2 addition to acetonyl has been predicted to be as high as several kcal mol^{-1} and as low as -0.7 kcal mol^{-1} relative to reactants. In addition, the lowest subsequent isomerization pathway, a 1-5 H-shift from the

methyl group to the peroxy group, is predicted to be anywhere from -1.0 to $+7.3$ kcal mol^{-1} relative to acetonyl + O_2. The wide discrepancies in these barrier heights lead to ambiguities regarding whether the acetonylperoxy radical should be expected to undergo isomerization reactions or simply dissociate back to acetonyl radical + O_2 in atmospheric and low-temperature combustion environments. As small shifts in these relative barrier heights lead to large shifts in kinetics predictions, the accurate description of reaction energetics for this system is lacking in the literature.

In addition, there seems to be no consensus on what the overall products are for the lowest energy isomerization pathway for this system. Kovács et al. have predicted enol-acetonyl + O_2 to be the final products, while El-Nahas et al. predict 3-oxetanone + OH. No existing theoretical study has considered these two possible pathways together. A better understanding of the products of the acetonyl + O_2 system will help produce more reliable atmospheric and combustion models.

In this study, we report a description of the acetonyl + O_2 reaction and subsequent isomerizations from highly-reliable *ab initio* theoretical methods near the correlation and complete basis set limits. The geometries of all important structures have been obtained using coupled-cluster theory, and the focal point approach is used to compute energetics to chemical accuracy. Multireference methods are used to describe the O_2 addition channel in order to accurately model this strongly-correlated radical-radical recombination process.

3.2 Theoretical Methods

3.2.1 Conformer Search

Conformer searches were performed on each intermediate in this study. A sequence of increasingly sophisticated methods was used to best estimate the number of conformers and their energies for each species. First, constrained energy scans were performed at the B3LYP/6-31G* level of theory. In these scans, each dihedral angle in the molecule was varied in 15 degree increments. For each local minimum found in the constrained potential energy surface, geometry optimizations were performed at the M06-2X/def2-TZVP level of theory. The unique local minima found from these DFT optimizations were subjected to single point energy computations at the CCSD(T)/cc-pVTZ level of theory with an ROHF reference. The lowest energy conformer from these energy computations was chosen for the coupled-cluster geometry optimization and energy computations described later in the Methods section. In cases where multiple conformers were within a few kcal mol^{-1} in energy as determined by the CCSD(T)/cc-pVTZ energies, multiple conformers were subjected to the higher level optimizations and energies. The DFT computations used in the conformer searches were done using the ORCA 4.0 software package.[117] The CCSD(T) single point energy computations on the conformers were performed using MOLPRO 2010.[68]

3.2.2 Geometries and Vibrational Frequencies

Each lowest energy stationary point located by the conformer search process was optimized at the CCSD(T)/ANO0 level of theory. The ANO0 basis set refers to a truncation of the full atomic natural orbital basis set of Almlöf and Taylor,[59] and it is comparable to a DZ Dunning-type basis but with more Gaussian primitives. An ROHF reference was used for the open-shell species to prevent spin

contamination. Structures were converged to an RMS force of 10^{-8} E_{H}/a_0. These optimizations were performed using the CFOUR software package.[57] Harmonic vibrational frequencies were obtained at the same level of theory using finite differences of analytic energy gradients. These vibrational frequencies were used to confirm stationary points as minima or transition states from the number of imaginary modes. The minima reported here have 0 imaginary modes, and the transition states (first-order saddle points) have 1 imaginary mode. Intrinsic reaction coordinate (IRC) computations were done at the B3LYP/cc-pVTZ level of theory to connect transitions states with their corresponding reactants and products. These IRC computations were completed using GAMESS 2014.[63,64]

To assess the error involved in using the ANO0 basis set for the geometry optimizations and frequency computations, a select few molecules in this study were subjected to a geometry optimization and harmonic frequency computation at the CCSD(T)/ANO1 level of theory. These computations were done via finite differences of energies using the OPTKING module of PSI4 to generate displacements and Molpro to compute the CCSD(T)/ANO1 energies. These higher-level geometries and frequencies were found to have only minimal effects ($\sim$0.1 kcal mol^{-1}) on the relative energies, so the ANO0 basis set was determined to be sufficient for this system.

3.2.3 Energetics

Higher-level energy computations were performed on each stationary point. The focal point approach (FPA) of Allen and coworkers was used to monitor the convergence of the energies in the full configuration interaction and complete basis set limits.[8,9] The Dunning cc-pVXZ (X = T, Q, 5) basis sets were used to extrapolate the Hartree–Fock energies to the CBS limit using the three point extrapolation formula $E_{\mathrm{HF}} = A + Be^{-CX}$.[67] The MP2, CCSD, and CCSD(T) energies

were extrapolated using the cc-pVXZ (X = T, Q) basis sets via the two point extrapolation formula $E_{\text{corr}} = A + BX^{-3}$.[13] Each of these energy computations was computed using MOLPRO 2010.[68,118]

Several corrections were appended to the electronic energy obtained from the extrapolations in order to account for approximations used in the energy computations. To estimate the effects of higher order excitations, a full triples and perturbative quadruples correction ($\Delta_{\text{T(Q)}}$) was computed. This correction estimates the effect of full triples at the CCSDT/6-31G* level of theory, while perturbative quadruples were estimated at the CCSDT(Q)/6-31G level. The use of these tiny basis sets for these computations is necessitated due to computational cost. A recent study on the equally-large 2-methylvinoxy radical + O_2 system found that CCSDT(Q)/6-31G was sufficient to estimate the contribution of perturbative quadruples.[116] The $\Delta_{\text{T(Q)}}$ corrections were all on the order of tenths of kcal mol^{-1} for the 2-methylvinoxy system, which is similar to the small $\Delta_{\text{T(Q)}}$ corrections reported for the unsubstituted vinoxy radical at the CCSDT(Q)/ANO0 level of theory.[115] These computations were performed using MRCC.[71]

To correct for the frozen core approximation, a core correction (Δ_{core}) was utilized at the CCSD(T)/cc-pCVTZ level by computing the difference between all-electron and frozen-core total energies for each species. This correction was computed using MOLPRO 2010. To account for the Born–Oppenheimer approximation, a diagonal Born–Oppenheimer correction (Δ_{DBOC}) was computed at the HF/ANO0 level of theory using CFOUR. Scalar relativistic effects were approximated using a relativistic correction (Δ_{rel}). This correction used the spin-free one-electron exact two component (X2C) method[119] with a fully decontracted cc-pCVDZ basis set. The PSI4 1.2 software package was used for this computation.[120] The zero-point vibrational energy correction, Δ_{ZPVE}, was computed from harmonic vibrational frequencies at the CCSD(T)/ANO0 level of theory using CFOUR. From all of these energy computations and corrections, enthalpies at zero Kelvin

(ΔH_{0K}) were computed for each species relative to separated acetonyl radical and O_2 as ΔH_{0K}= ΔE_e+ $\Delta_{T(Q)}$+ Δ_{core}+ Δ_{rel}+ Δ_{DBOC}+ Δ_{ZPVE}.

The focal point approach is used so that the ΔH_{0K} values may be obtained to chemical accuracy ($\pm$ 1 kcal mol^{-1}). In other words, the energies reported here are not expected to change by more than 1 kcal mol^{-1} if higher-level corrections are included. The "$\pm$1 kcal mol^{-1}" range used here should not be interpreted as a statistical uncertainty on these reported energies but rather an (often generous) accuracy threshold which the focal point approach has been demonstrated to achieve for systems of similar size and type.[85,86,115,116] For molecules where this accuracy expectation may break down (e.g. due to multireference character), a discussion of this potential source of error is provided in the text.

3.2.4 Entrance channel treatment

The radical-radical recombination reaction for the addition of O_2 to acetonyl radical is expected to have significant multireference character, a property that motivates the use of multireference methods for this reaction in order to predict the barrier as reliably as feasible. First, a series of constrained geometry optimizations were performed at the CASPT2/cc-pVTZ level of theory. In these geometry optimizations, the C–OO bond distance was varied from 1.6 to 3.0 Å, and all other coordinates were relaxed. This region of bond lengths can be expected to have the transition state for our system, as evidenced by previous studies that report transition states with C–OO bond lengths at around 2.2-2.3 Å.[54,112] A CAS(9 e$^-$, 7 orb.) reference was used for all multireference computations. This active space consists of the π space (6,4) of O_2 and the π space (3,3) of the acetonyl radical. This active space has been found to work well for the 2-methylvinoxy radical + O_2 system.[116] To compute the energies of these geometries, we use a composite coupled-cluster and

multireference configuration interaction method that has been used to study the corresponding O_2 addition reactions of other resonance-stabilized radicals.[79,115,116] This method consists firstly of CCSD(T) computations with a large cc-pVQZ basis set on the high-spin quartet state of the system. From this CCSD(T) quartet energy is then subtracted the quartet-doublet splitting energy computed using MRCISD+Q with a cc-pVTZ basis set.

$$E^{\mathrm{Db}}_{\mathrm{total}} = E^{\mathrm{Qt}}_{\mathrm{CC/QZ}} - \left(E^{\mathrm{Qt}}_{\mathrm{MRCI/TZ}} - E^{\mathrm{Db}}_{\mathrm{MRCI/TZ}} \right). \tag{1}$$

For the sake of brevity, we will refer to this method as $CC^{(q)}$+$MR^{(d,q)}$ throughout this paper. All of these entrance channel computations were performed using MOLPRO 2010.[68,72–74,76,77,81,82]

3.3 Results and Discussion

The potential energy surface containing the most significant computed structures for the acetonyl radical + O_2 system is shown in Figure 3.1. The following subsections examine the predicted reaction pathways in detail, starting with the entrance channel before progressing through peroxy radical isomerizations and final product formation.

3.3.1 Entrance Channel

Previous studies have demonstrated the necessity and effectiveness of multireference methods for related vinoxy + O_2 reactions.[115,116] These studies concluded that vinoxy radical + O_2 reactions are essentially barrierless, similar to how alkyl radical + O_2 reactions are barrierless.[86,121,122] Because of the wide discrepancy in the literature regarding the existence of a barrier for the **R0** entrance

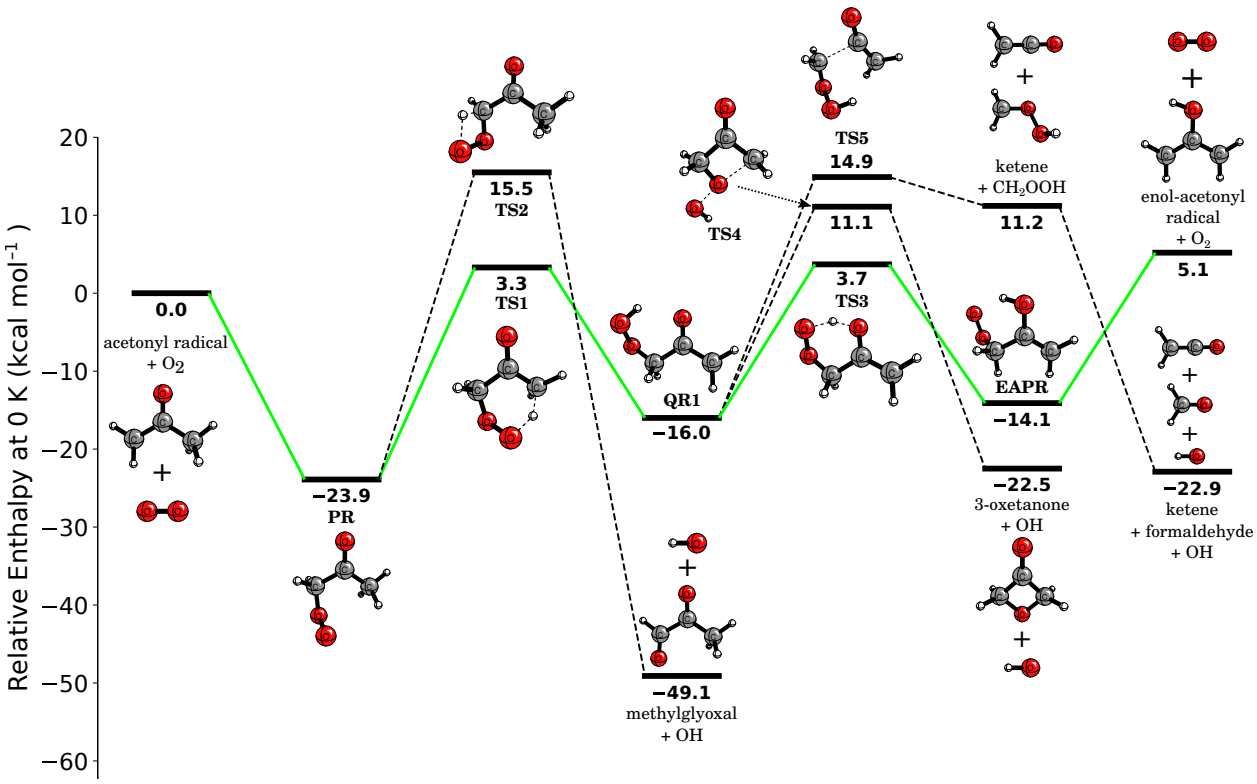

Figure 3.1: Abridged potential energy surface for the acetonyl radical + O_2 reaction. Relative enthalpies at zero Kelvin were computed as $\Delta H_{0\text{K}} = \Delta E_e + \Delta_{\text{T(Q)}} + \Delta_{\text{core}} + \Delta_{\text{rel}} + \Delta_{\text{DBOC}} + \Delta_{\text{ZPVE}}$. All structures were optimized at the CCSD(T)/ANO0 level of theory. The predicted minimum energy isomerization pathway of **PR** is shown in green. In cases where multiple conformers exist, only the lowest energy structure is shown. Some post-reaction complexes and IRC-connected conformers have been omitted for succinctness and to facilitate comparison with previous literature. See Figure B.1 in the Appendix for a potential energy surface with all relevant species shown.

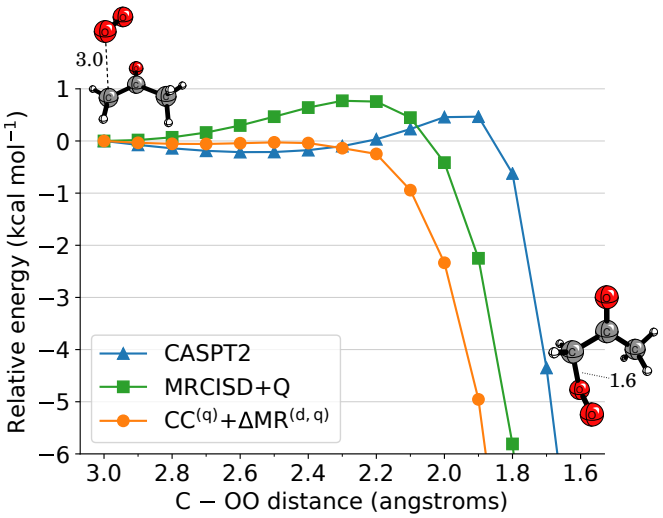

Figure 3.2: Three theoretical methods for energies (kcal mol^{-1}) of the addition of O_2 to the acetonyl radical, forming the acetonylperoxy radical (**PR**). Energies were computed using structures obtained at the CASPT2/cc-pVTZ level of theory. For the optimizations, the C–OO bond distance was varied in 0.1 Å increments, while all other geometric parameters were optimized. For each curve, energies are computed relative to the energy at 3.0 Å.

channel, multireference computations were performed for this reaction. Results are shown in Figure 3.2.

At the CASPT2/cc-pVTZ level of theory, the entrance channel is characterized by the shallow well of a van der Waals complex with a C–OO bond length of around 2.5 Å. From this complex, there is a barrier of around 0.7 kcal mol^{-1} to form **PR**. The transition state has a C-OO bond length of around 1.9 Å at this level of theory. At the MRCISD+Q/cc-pVTZ level of theory, a barrier of about 0.8 kcal mol^{-1} is found, and the transition state occurs at the longer C-OO bond length of 2.3 Å. Finally, the CC$^{(q)}$+MR$^{(d,q)}$ method, the most sophisticated treatment of static and dynamic correlation used, predicts the reaction to be barrierless. The energy curve at this level of theory is essentially flat in the region from 3.0 to 2.4 Å, and no evidence is seen for either a van der Waals complex or a reaction barrier. This result agrees with previous studies that found

barrierless entrance channels for the analogous vinoxy radical + O_2 reactions using multireference methods.[115,116] This result is in contrast to previous theoretical studies which predict significant barriers for this reaction using DFT or single-reference *ab initio* methods.[54,103,104]

Another possible entrance channel involves a direct hydrogen abstraction by O_2 of a methyl hydrogen to form HO_2 and the CH_2COCH_2 diradical. We do not consider this pathway here due to the computations of Hassouna et al. which place the barrier for this reaction at nearly 25 kcal mol^{-1} above reactants.[103] Alternatively, the HO_2 elimination channel could produce the cyclic species cyclopropanone (CH_2COCH_2). Preliminary computations on this pathway found that the products cyclopropanone + HO_2 together lie around 15 kcal mol^{-1} above the acetonyl radical + O_2 reactants. While a transition state could not be located for this reaction, its energy would be assumed to be even higher than 15 kcal mol^{-1}, so this pathway was not explored further.

3.3.2 The acetonylperoxy radical (PR)

The addition of O_2 to acetonyl radical via reaction **R0** produces the acetonylperoxy radical **PR** ($^{\bullet}OOCH_2COCH_3$), which lies 23.9 kcal mol^{-1} below separated reactants. This well-depth for **PR** is slightly lower in magnitude than the literature values of -25.0 and -26.3 kcal mol^{-1} predicted by Kuwata et al. and El-Nahas et al., respectively, both at a CBS-QB3 level of theory. A total of four conformers of **PR** were found at the CCSD(T)/ANO0 level of theory. They are shown in Figure 3.3.

The conformers are distinguished by two dihedral angles. The first corresponds to the peroxy group either being in the plane or out of the plane of the carbons, producing conformers of C_s or C_1 symmetry, respectively. The second is the peroxy group being either cis or trans with respect to the ketone oxygen. For the lowest energy conformer, **PRa**, the peroxy group is rotated out of the

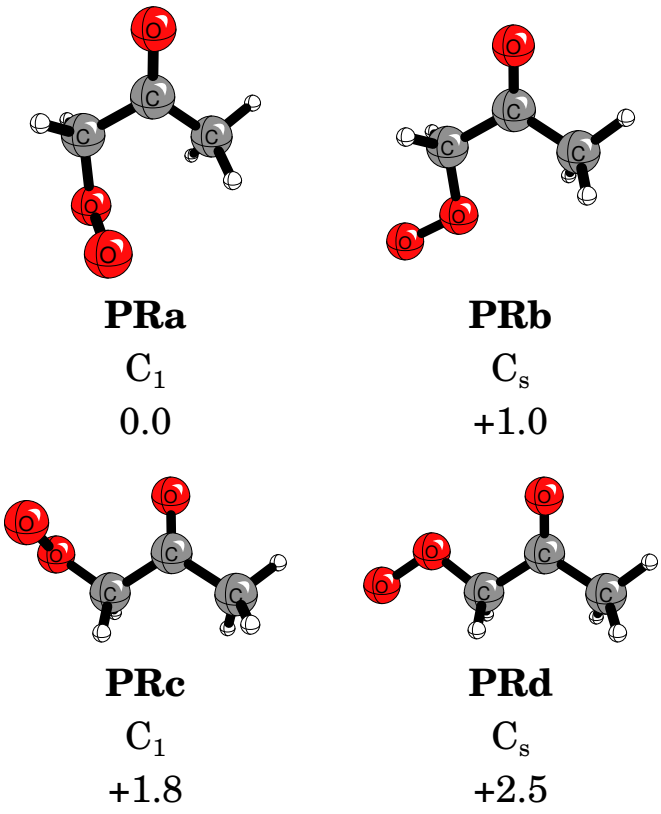

Figure 3.3: Conformers of the acetonylperoxy radical **PR**. Molecular point group symmetry labels are given along with relative energies (kcal mol^{-1}) compared to the lowest energy conformer, **PRa**. Geometries were computed at the CCSD(T)/ANO0 level of theory. Relative energies were computed at the CCSD(T)/CBS level of theory and include ZPVE corrections. Conformer **PRa** has a ΔH_{0K} of -23.9 kcal mol^{-1} compared to separated acetonyl radical + O_2 at the FPA level of theory.

Table 3.1: Focal point table for **PRa**, the lowest energy conformer of the acetonylperoxy radical **PR**. Energies (kcal mol^{-1}) are relative to the acetonyl radical + O_2 reactants.

	HF	$+\delta$MP2	$+\delta$CCSD	$+\delta$CCSD(T)	NET
cc-pVDZ	-23.47	$+17.27$	-16.21	-0.35	$[-22.76]$
cc-pVTZ	-23.79	$+14.40$	-16.81	-0.66	$[-26.86]$
cc-pVQZ	-23.38	$+13.41$	-17.06	-0.77	$[-27.81]$
cc-pV5Z	-23.28	$[+13.06]$	$[-17.15]$	$[-0.81]$	$[-28.19]$
CBS LIMIT	$[-23.25]$	$[+12.69]$	$[-17.24]$	$[-0.85]$	$[-28.66]$
$\Delta H_{0K} = \Delta E_e + \Delta_{T(Q)} + \Delta_{core} + \Delta_{rel} + \Delta_{DBOC} + \Delta_{ZPVE}$					
$= -28.66 + 0.55 - 0.06 + 0.09 - 0.03 + 4.25 = \mathbf{-23.9}$					

plane of the carbons and trans with respect to the ketone oxygen. All four conformers are within a few kcal mol^{-1} of energy from the lowest conformer which suggests **PR** may interconvert readily between conformers in a low temperature combustion environment. The four **PR** conformers reported here and their energetic ordering coincide with the four conformers found for the peroxy radical in the unsubstituted vinoxy radical + O_2 system.[115] Conformers **PRa**, **PRc**, and **PRd** have been reported previously by Kuwata et al.,[54] and **PRa** and **PRd** have been reported by El-Nahas et al. Conformer **PRb** has not been reported in the literature.

The ΔH_{0K} of **PR** obtained via the focal point approach is shown in Table 3.1 as an example of this method. Good convergence is achieved in both the full configuration interaction (FCI) and complete basis set (CBS) limits. The $\Delta_{T(Q)}$ correction of 0.55 kcal mol^{-1} is typical for the minima reported in this study, and its value suggests that including additional correlation will not significantly change the energy. Though the relatively small 6-31G* and 6-31G basis sets were used to compute this $\Delta_{T(Q)}$ correction due to computational cost, the analysis by Davis et al. found that these approximations still qualitatively describe the magnitude of this correction.[116] Overall, the convergence of the energy as demonstrated in Table 3.1 suggests that this result is converged to within chemical accuracy ($\pm$ 1 kcal mol^{-1}).

3.3.3 The 1-5 H shift reaction from PR

The acetonylperoxy radical **PR** may undergo a number of unimolecular isomerizations in an analogous manner as the well-studied isomerizations of alkylperoxy radicals.[86,122] The reactivity available for **PR** is most closely related to that of the *n*-propylperoxy radical ($^{\bullet}OOCH_2CH_2CH_3$) due to the available hydrogens in the α and γ locations relative to the peroxy group. However, the lack of hydrogens available in the β position relative to the peroxy group in **PR** largely affects the availability of low-lying pathways. In particular, the HO_2 elimination reaction involving a β-hydrogen—a submerged pathway for *n*-propylperoxy[86]— is unavailable for **PR**.

Compared with the unsubstituted vinoxy radical + O_2 system and the 2-methylvinoxy + O_2 system, **PR** lacks a formyl hydrogen in the β position. An abstraction of this hydrogen, a 1-4 H shift, is predicted to be the lowest energy pathway for these related systems,[115,116] but this pathway is unavailable for **PR**.

The lowest pathway found stemming from **PR** is a 1-5 H shift from the methyl group to form the primary QOOH radical **QR1**. The transition state for this reaction, **TS1**, is 3.3 kcal mol^{-1} higher in energy compared to separated acetonyl radical + O_2. It is shown in Figure 3.4. This transition state is characterized by a six-membered ring that is formed as the hydrogen is transferred.

The elevated enthalpy of **TS1** relative to separated reactants is intriguing in light of the results from the vinoxy + O_2 and *n*-propyl + O_2 systems. For the unsubstituted vinoxy + O_2 and 2-methylvinoxy + O_2 systems, a 1-4 H shift from the formyl group, passing through a 5-membered ring transition state, is submerged by around 1 kcal mol^{-1} compared to separated reactants. The 1-5 H shift reaction for the acetonyl + O_2 system could be expected to be even lower in energy

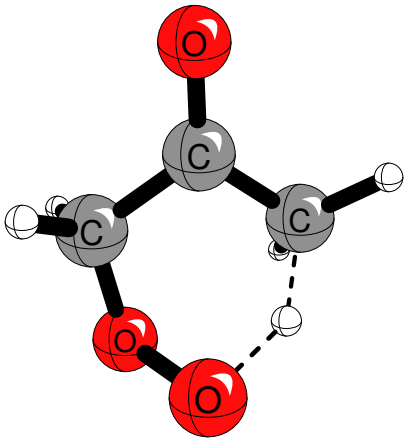

TS1
+3.3
(+27.1)

Figure 3.4: Structure of **TS1**, the transition state for the 1-5 H shift reaction from acetonylperoxy radical **PR** forming hydroperoxyacyl radical **QR1**. The geometry was optimized at the CCSD(T)/ANO0 level of theory. The enthalpy at zero Kelvin relative to reactants is given, and the enthalpy relative to **PR** is given in parentheses.

due to requiring a less-strained 6-membered ring transition state. However, the raised energy of **TS1** is indicative of the relatively stronger C–H bond in a methyl group compared to a C–H bond in a formyl group.

For the *n*-propyl radical + O_2 system, the analogous 1-5 H shift transition state is submerged relative to separated reactants by nearly 8 kcal mol^{-1}. The unfavorability of **TS1** compared to this transition state could be explained by the fact that the central carbon in **TS1** is sp^2 hybridized due to the C=O double bond. Meanwhile, the central carbon in the *n*-propyl + O_2 system is sp^3 hybridized. This hybridization of the central carbon in **TS1** leads to it having increased strain on the C–C–C backbone to form the 6-membered ring required for the 1-5 H shift, and this increased strain leads to the heightened relative enthalpy for **TS1**.

The focal point table for **TS1** is given in Table 3.2. An unphysically large Δ_{DBOC} of $+0.78$ kcal mol^{-1} was computed for this molecule. Anomalously large values for Δ_{DBOC} have been reported for many similar H-shift transition states of peroxy radicals.[85,86,115,116] As this value of Δ_{DBOC} is expected to be an artefact of a nearby conical intersection,,[86] we exclude it from the energy computation of **TS1**. Regarding the convergence of the energy of **TS1** to the full CI limit, there is found to be a large contribution to the energy at the CCSD(T) level of theory. With a cc-pVQZ basis set, the CCSD(T) contribution to the relative energy is -4.22 kcal mol^{-1}. This large magnitude of energy change on its own may suggest that higher order excitations are necessary in order to accurately compute a relative energy for **TS1**. However, the $\Delta_{\text{T(Q)}}$ of $+0.34$ kcal mol^{-1} is quite small, indicating that the computed relative energy is converged at the full CI limit. Similar behavior regarding large CCSD(T) contributions was found for the analogous transition state for the *n*-propyl + O_2 reaction. The 1-5 H shift transition state for *n*-propyl + O_2 has a CCSD(T)/cc-pVQZ correction of -4.40 kcal mol^{-1}, but the CCSDT(Q)/6-31G* correction is only -0.03 kcal mol^{-1}.[86] Many transition states for the vinoxy radical + O_2 and 2-methylvinoxy radical + O_2 systems were also found to exhibit large CCSD(T) and tiny CCSDT(Q) corrections.[115,116] Together, these findings suggest that the computed $\Delta H_{0\text{K}}$ of **TS1** is converged to within chemical accuracy. This property of large CCSD(T) contributions to the relative energies and small CCSDT(Q) contributions was found to be prevalent among the transition states in this study.

3.3.4 The hydroperoxyacyl radical (QR1)

The 1-5 H shift reaction of **PR** by way of **TS1** produces the QOOH radical **QR1**. At the CCSD(T)/ANO0 level of theory, a total of three conformers were found, and they are shown in Figure 3.5. The

Table 3.2: Focal point table for **TS1**, the transition state for a 1-5 H shift from the acetonylperoxy radical. Energies (kcal mol^{-1}) are relative to the acetonyl radical + O_2 reactants. An unphysically large Δ_{DBOC} of +0.78 was excluded from the analysis as it may be an artefact of a nearby surface crossing.

	HF	$+\delta$MP2	$+\delta$CCSD	$+\delta$CCSD(T)	NET
cc-pVDZ	31.61	-12.16	-6.36	-2.99	$[+10.09]$
cc-pVTZ	31.19	-17.69	-5.09	-3.99	$[+4.42]$
cc-pVQZ	31.62	-19.32	-4.76	-4.22	$[+3.31]$
cc-pV5Z	31.72	$[-19.90]$	$[-4.65]$	$[-4.31]$	$[+2.87]$
CBS LIMIT	$[+31.75]$	$[-20.51]$	$[-4.52]$	$[-4.39]$	$[+2.32]$
$\Delta H_{0\text{K}} = \Delta E_e + \Delta_{\text{T(Q)}} + \Delta_{\text{core}} + \Delta_{\text{rel}} + \Delta_{\text{DBOC}} + \Delta_{\text{ZPVE}}$					
$= 2.32 + 0.34 + 0.02 + 0.09 + 0.00^* + 0.51 = \mathbf{3.3}$					

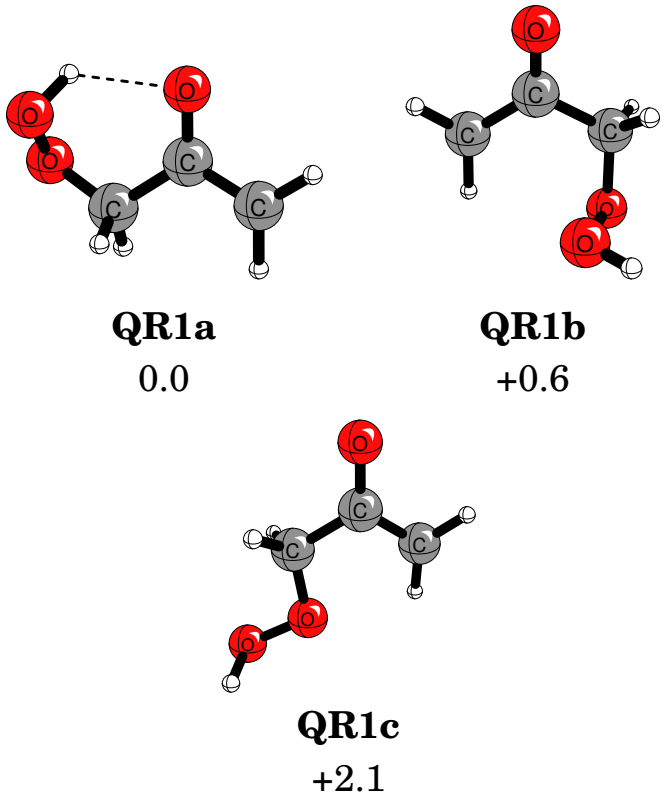

Figure 3.5: Conformers of the QOOH radical **QR1**. Relative enthalpies (kcal mol^{-1}) compared to the lowest energy conformer, **QR1a**, are given. Geometries were computed at the CCSD(T)/ANO0 level of theory. Relative enthalpies were computed at the CCSD(T)/CBS level of theory and include ZPVE corrections at the CCSD(T)/ANO0 level.

lowest energy conformer, **QR1a**, has a ΔH_{0K} of -16.0 kcal mol^{-1} compared to reactants. It is characterized by a hydrogen bond between the hydroperoxy hydrogen and the ketone oxygen with a H–O distance of 2.09 Å.

In the second lowest conformer, **QR1b**, the hydroperoxy moiety is rotated to be anti with respect to the ketone oxygen. The hydroperoxy oxygens are rotated out of the plane of the carbon atoms, and the hydroperoxy hydrogen is oriented away from the ketone oxygen. Conformer **QR1b**, while 0.6 kcal mol^{-1} higher in energy than **QR1a**, is the IRC product of the 1-5 H shift reaction of **PR** through **TS1**. The transition state for the interconversion between **QR1b** and **QR1a** was located at the M06-2X/def2-TZVP level of theory, and the energy of the transition state was found to be only 1.1 kcal mol^{-1} higher than **QR1b**. Thus, the **QR1b** formed from the reaction through **TS1** can be expected to readily convert to the lower energy **QR1a** conformer.

The highest energy conformer found, **QR1c**, is 2.1 kcal mol^{-1} higher in energy than **QR1a**. Similarly to **QR1b**, the hydroperoxy moiety of **QR1c** is rotated to be anti with respect to the ketone oxygen. The hydroperoxy oxygen atoms are rotated to lie nearly in the plane of the carbon atoms, producing a molecule that is close to C_s symmetry but ultimately C_1. Conformers **QR1b** and **QR1c** correspond to the two **QR1** conformers reported by El-Nahas et al.,[112] while no structures in the literature have been reported for the hydrogen-bonded structure **QR1a**, the lowest in energy of the conformers found here.

3.3.5 Reactions stemming from QR1

The hydroperoxyacyl radical **QR1** may undergo further unimolecular isomerization reactions. The four most probable pathways are examined here, and their transition states are shown in Figure 3.6. Similar to the reactions stemming from **PR**, none of the four reactions of **QR1** were

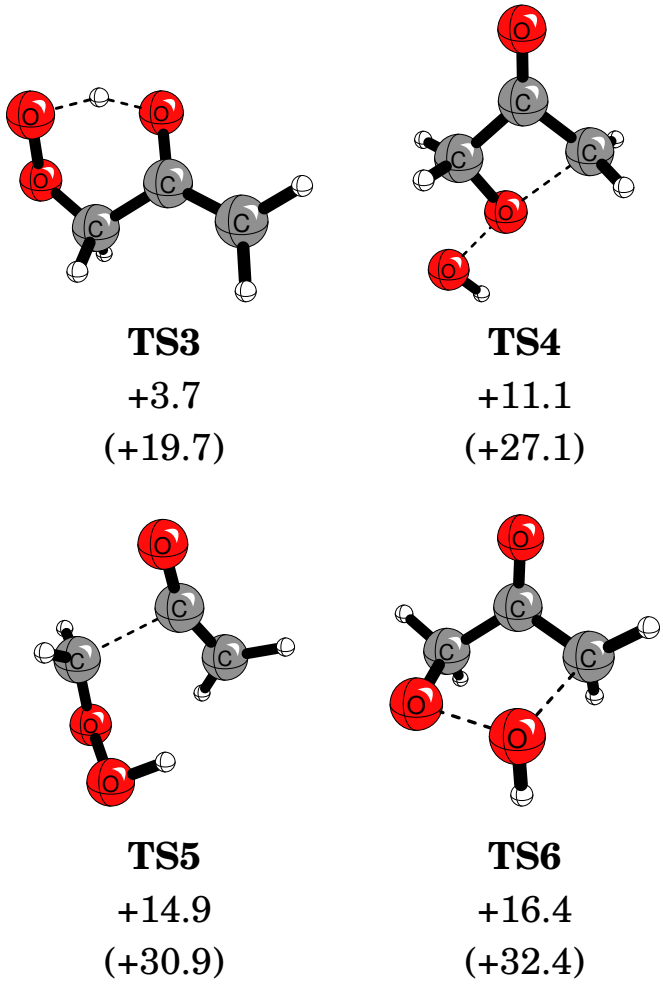

Figure 3.6: Transition states for the unimolecular reactions involving QOOH radical **QR1**. The ΔH_{0K} values relative to reactants are given, and ΔH_{0K} relative to **QR1** are given in parentheses. Geometries were computed at the CCSD(T)/ANO0 level of theory, except for **TS6**, which was computed at the M06-2X/def2-TZVP level.

found to be submerged relative to acetonyl + O_2 reactants. Furthermore, all of these transition states are higher in energy than **TS1**. Thus, the most thermodynamically favorable pathway found for **QR1** is to convert back to **PR**. We also note that **QR1**, as with QOOH radicals in general, may add an additional O_2 to form an $^{\bullet}$OOQOOH species.[25,123] These species are significant in that their degradation forms OH radicals, which can lead to chain propagation of radicals in a low-temperature combustion environment. This O_2 addition pathway is outside the scope of this study and is not considered here.

The lowest energy pathway found is a 1-5 hydrogen shift from the hydroperoxy group to the ketone oxygen. This reaction passes through a 6-membered ring transition state, **TS3**, which has a ΔH_{0K} of 3.7 kcal mol^{-1}. The ΔH_{0K} of **TS3** features a rather large $\Delta_{T(Q)}$ of -1.27 kcal mol^{-1}. This is the largest magnitude $\Delta_{T(Q)}$ of all the molecules considered in this study. This transition state does not have significant multireference character as evidenced by a leading c_0^2 of 0.93 and a T_1 diagnostic value of 0.031, so this correction does not seem to be due to quadruple excitations capturing static correlation effects. Further investigations would be necessary to ascertain why the $\Delta_{T(Q)}$ of **TS3** is so sensitive to the level of dynamic correlation included. Overall, the ΔH_{0K} of **TS3** is the most uncertain ΔH_{0K} value in this study. However, the H-shift pathway through **TS3** is still predicted to be the lowest energy pathway available to **QR1** due to the significantly higher energies of **TS4**, **TS5**, and **TS6**.

The H-shift reaction from **QR1** through **TS3** produces the enol-acetonylperoxy radical, labeled **EAPR**. Species **EAPR** is similar to **PR** except that a hydrogen is shifted from the methyl group to the ketone oxygen, and a C=C double bond forms. A total of 9 conformers were found for this molecule at the M06-2X/def2-TZVP level of theory. The lowest energy conformer was determined by CCSD(T) computations on these DFT structures, and only this lowest energy structure was

subjected to further CCSD(T)/ANO0 geometry optimization and focal point energy computations. This lowest energy conformer, labeled **EAPRa** is shown in Figure 3.7. Conformer **EAPRa** was found to be lower in energy by at least 1.8 kcal mol^{-1} compared to all other conformers of **EAPR**. It is characterized by an OH$\cdots$O hydrogen bond of length 1.974 Å. It is the only conformer found with such a hydrogen bond, which explains why this conformer is lowest in energy.

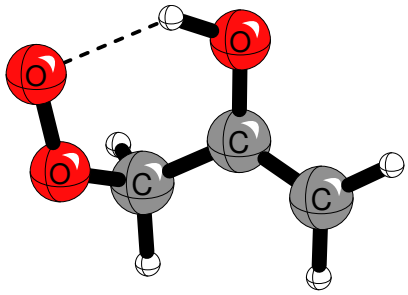

EAPRa
–14.1

Figure 3.7: Structure of the enol-acetonylperoxy radical **EAPRa**, the lowest of nine conformers of **EAPR**. The ΔH_{0K} value relative to acetonyl + O_2 reactants is given. This geometry was computed at the CCSD(T)/ANO0 level of theory.

EAPR can lose O_2 to form the enol-acetonyl radical (2-hydroxypropenyl radical). The enol-acetonyl radical and O_2 together lie 5.1 kcal mol^{-1} above the acetonyl-radical + O_2 reactants. We assume that this dissociation is a barrierless process in a similar manner as the **R0** entrance channel is barrierless. This reaction is the lowest overall product pathway of the acetonyl radical + O_2 system. Thus, the minimum energy isomerization pathway for O_2 addition to acetonyl radical is a keto-enol tautomerization that is catalyzed by O_2.

The second lowest energy pathway from **QR1** is predicted to be an OH elimination reaction that forms 3-oxetanone via **TS4**. The structure of **TS4** is shown in Figure 3.6. With a ΔH_{0K} value of $+11.1$ kcal mol^{-1}, **TS4** is almost eight kcal mol^{-1} higher in energy than **TS3**. Transition state **TS4** is found to be connected to **QR1** conformer **QR1c** from IRC computations. This transition

state was found to be have significant multireference character as evidenced by a leading c_0^2 of 0.72. In light of the multireference nature of this system, the single-reference coupled cluster methods used here may not be expected to be completely reliable for this species. However, we would still not expect a more sophisticated treatment of strong correlation on this system to find that **TS4** is lower in energy than **TS3** due to the large energy difference.

The end products of **TS4** are 3-oxetanone and OH. A post-reaction complex of OH and 3-oxetanone was found at the CCSD(T)/ANO0 level of theory. This complex exhibits a C_{2v} structure with an OH$\cdots$O hydrogen bond of 1.87 Å. This complex is around 5 kcal mol^{-1} lower in energy than separated 3-oxetanone and OH. The 3-oxetanone molecule produced exhibits a 4-membered ring structure, and it is a constitutional isomer of $\beta-$propiolactone. While this reaction also produces the OH radical, its transition state **TS4** is rather high in energy, so we do not predict that OH production via this pathway will be significant except at high temperatures.

The third pathway found stemming from **QR1** involves a C–C bond cleavage to form ketene and CH_2OOH (hydroperoxymethyl radical). This reaction passes through **TS5**, which has a ΔH_{0K} of $+14.9$ kcal mol^{-1} and lies 30.9 kcal mol^{-1} above **QR1**. IRC computations find **TS5** to connected to the **QR1** conformer **QR1b**. **TS5** was found to be moderately singly reference with a c_0^2 of 0.89 and a c_1^2 of only 0.03. This reaction forms a post-reaction complex featuring an OH$\cdots\pi$ bond between the hydroperoxy hydrogen of CH_2OOH and the π system of ketene. This complex is around 4 kcal mol^{-1} lower in energy than separated ketene and CH_2OOH. The hydroperoxymethyl radical will undergo O–O cleavage to form formaldehyde and OH. This dissociation of OH from hydroperoxymethyl is generally considered to be barrierless.[54,115,116] From previous literature regarding the dissociation of α-QOOH radicals,[124] we predict that this dissociation is barrierless, and accordingly no attempts were made to optimize a transition state for this reaction. This

pathway provides another route to the production of OH; however, this pathway is once again hindered by a high activation barrier due to **TS5**.

Several other pathways from **QR1** were considered for inclusion in this study but ultimately not fully characterized due to having high energies and having difficult theoretical properties. A transition state, **TS6**, for OH transfer from the hydroperoxy group to the methyl group was located at the M06-2X/def2-TZVP level. This DFT structure was subjected to the same focal point energetic analysis as the other structures in this study, and it is shown in Figure 3.6. A ΔH_{0K} of 17.6 kcal mol^{-1} was computed for this structure, which means its energy is even higher than the other three transition states from **QR1** included in this study. It also has significant multireference character, as evidenced by a c_0^2 of 0.85. The OH shift reaction via this transition state produces $^{\bullet}OCH_2COCH_2OH$. This molecule has a ΔH_{0K} of -59.7 kcal mol^{-1} and was found to be the lowest energy minimum of all the molecules in this study. Despite being the overall thermodynamic product of the products considered in this study, we still do not predict it to be accessible except at high temperatures. HO_2 elimination pathways from **QR1** to form $^{\bullet}CH_2CO^{\bullet}CH_2$ or cyclopropanone were also considered. However, similarly to the other HO_2 elimination pathways discussed earlier, preliminary computations at the M06-2X/def2-TZVP level predict these pathways to be much higher than the other pathways considered here.

3.3.6 The 1-3 H shift reaction from PR

Acetonylperoxy radical **PR** may also undergo a 1-3 H shift from the α-carbon. This reaction passes through a transition state requiring a four-membered ring, **TS2**, shown in Figure 3.8. Likely due to this highly strained four-membered ring, **TS2** has a substantial ΔH_{0K} of 15.5 kcal mol^{-1}. This high energy places **TS2** over 12 kcal mol^{-1} higher than **TS1**. The overall barrier to this transition

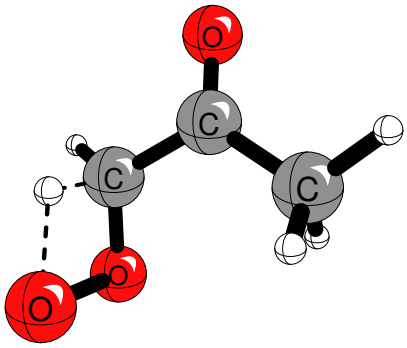

TS2

+15.5

(+39.4)

Figure 3.8: Structure of **TS2**, the transition state for the 1-3 H shift reaction from the acetonylperoxy radical **PR**. The geometry was optimized at the CCSD(T)/ANO0 level of theory. The enthalpy at zero Kelvin relative to reactants is given, and the enthalpy relative to **PR** is given in parentheses.

state from **PR** is 39.4 kcal mol^{-1}. These results agree with findings from previous studies which found high barriers for analogous 1-3 H shift reactions for peroxy radicals.[86,115,116] Due to its high barrier, this pathway is not expected to be competitive to the 1-5 H shift pathway through **TS1** in an atmospheric or low-temperature combustion environment.

The ultimate product of the 1-3 H shift reaction through **TS2** was determined to be methylglyoxal + OH. Together, these lie 49.1 kcal mol^{-1} below the separated reactants. IRC computations at the B3LYP/cc-pVTZ level indicate that **TS2** does not lead to an α-QOOH radical. Instead, OH is eliminated directly after the hydrogen is abstracted. During this elimination, a post-reaction complex of OH and methylglyoxal is formed. This complex is predicted to lie around 4 kcal mol^{-1} lower than methyl-glyoxal and OH from computations at the CCSD(T)/ANO0 level.

Our finding of no α-QOOH formation is in contrast to previous theoretical studies on this system that report α-QOOH intermediates along the 1-3 H shift pathway.[54,103,104,112] This finding

is also different from the very high-level findings of Bartlett et al.[86] for the related *n*-propyl + O_2 system, whereby an α-QOOH radical was found to be the product of the analogous 1-3 shift from the *n*-propylperoxy radical. Bartlett et al. estimated a barrier for OH dissociation of up to 10 kcal mol^{-1} from this α-QOOH species from constrained geometry scans at the CCSD(T)/cc-pVTZ level of theory. Multireference computations by Bartlett et al. were unsuccessful in finding a transition state for OH dissociation due to the complexity of the potential energy surface. This complexity stems from a detected nearby surface crossing in the region of the OH-dissociation of the analogous α-QOOH radical.

These findings for the *n*-propyl + O_2 system suggest that that the region of the potential energy surface following **TS2** is highly complex. Due to the intricate features of the potential energy surface in this region, we do not expect our IRC computations at the B3LYP/cc-pVTZ level of theory to fully characterize this region. Accordingly, efforts were made to optimize α-QOOH structures at the CCSD(T)/ANO0 level of theory, and one conformer was located.

Overall, these findings suggest that the end result of the pathway through **TS2** is the production of methylglyoxal and OH. While the existence of an α-QOOH intermediate is unclear, any α-QOOH species potentially formed would almost certainly immediately dissociate into methylglyoxal and OH. This result follows from the high energy required to go through **TS2**. A recent theoretical study by Anglada et al.[124] does a thorough examination of the unique features of general α-QOOH dissociation. Further theoretical studies are necessary to fully characterize the precise nature of α-QOOH formation and dissociation for the acetonyl radical + O_2 system.

3.4 Conclusions

A close examination has been performed on the acetonyl radical + O_2 reaction system using highly reliable structures and energetics. The relevant structures and their conformers have been optimized at the CCSD(T)/ANO0 level of theory, and the energetics were computed using the focal point method. Chemical accuracy was achieved via coupled-cluster computations with excitations up to CCSDT(Q) and basis sets up to cc-pV5Z.

Multireference computations were used to analyze the addition reaction of O_2 to acetonyl radical. No barrier to O_2 addition was found, in agreement with recent literature on similar vinoxy radical + O_2 systems but in disagreement with previous literature on the acetonyl radical + O_2 system. Because of this lack of barrier, the overall lowest energy pathway available for the acetonylperoxy radical is simply dissociating back to reactants.

No submerged unimolecular isomerization pathways for the acetonylperoxy radical were found. Besides dissociation, the lowest energy isomerization reaction is a 1-5 H shift from the methyl group to the peroxy group. The transition state for this reaction is 27.1 kcal mol^{-1} higher than the acetonylperoxy radical and 3.3 kcal mol^{-1} higher in energy than the acetonyl radical + O_2 reactants. This reaction forms a primary hydroperoxyacyl (QOOH) radical, and this species can undergo a 1-5 H shift to form the enol tautomer of the acetonylperoxy radical. Dissociation of O_2 from the enol-acetonylperoxy radical produces the enol-acetonyl radical, which is 5.1 kcal mol^{-1} higher in energy than acetonyl radical.

While the unsubstituted vinoxy and 2-methylvinoxy radical + O_2 systems feature submerged pathways that lead to OH production, no such features were found for acetonyl radical + O_2. Several pathways were identified that lead to the production of OH, but all of these pathways are

not expected to be significant in an atmospheric or low-temperature combustion setting due to high energetic barriers.

Chapter 4

The Prototypical Transition Metal Carbenes[1]

[1]Reprinted with permission from Weidman, J. D.; Estep, M. L.; and Schaefer, H. F. *J. Phys. Chem. A.* **2018**, *122*, 6570-6577. Copyright 2018 American Chemical Society.

Abstract

Transition metal carbenes are useful in organometallic chemistry due to their demonstrated use as catalysts in carbon-carbon bond forming reactions. Yet, the prototypical transition metal carbenes—consisting of a single metal center doubly bonded to a methylene ligand and surrounded by carbonyls—have been elusive to experimental synthesis. This theoretical work examines the structures and properties of nine prototypical transition metal carbenes. Optimized values for M=CH_2 bond lengths, dissociation energies, and vibrational frequencies are reported. The M=CH_2 bond distances range from 1.81 Å (Ni) to 2.05 Å (Pd). The M=CH_2 dissociation energies fall in the range of 16.4 kcal mol^{-1} (Pd) to 92.3 kcal mol^{-1} (Os). The spectroscopic observation of several of these molecules should be possible.

4.1 Introduction

Transition metal carbenes have gained considerable interest in the organometallic chemistry community due to their usefulness in the synthesis of many organic compounds. These complexes have had widespread use as catalysts in olefin metathesis processes,[125] and they have been used in alkene cyclopropanation and carbonyl alkenation reactions.[126] Transition metal carbenes are generally categorized as Fischer carbenes[127] or Schrock carbenes[128] based on their bonding characteristics.

The bonding in Fischer-type transition metal carbenes is often understood in terms of the Dewar-Chatt-Duncanson (DCD) model (Figure 4.1a).[129] In this model, the double bond between the metal and ligand can be considered the result of σ donation from the carbon to the metal and π back-donation from the metal to the carbon. The bonding in Schrock carbenes, meanwhile, can be understood as a traditional double bond where both the metal and carbon share two σ and two

π electrons (Figure 4.1b). Schrock carbenes are more accurately described as alkylidenes due to this bonding character.

Figure 4.1: Schematic of the typical bonding patterns in (a) Fischer carbenes and (b) Schrock carbenes.

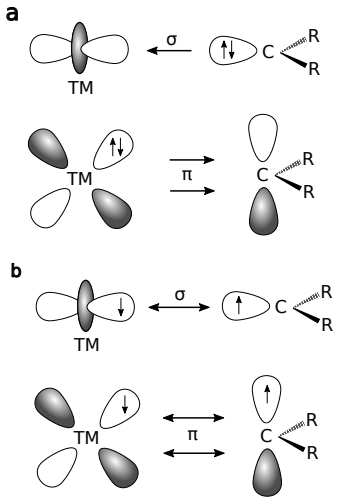

This work considers prototypical transition metal carbenes—the simplest possible transition metal carbenes, in the expectation that they should be experimentally viable. With these guidelines in mind, the simplest realistic transition metal carbenes would consist of the simplest carbene ligand, methylene, attached to a single metal center in a neutral complex that obeys the eighteen electron rule.[130,131] These prototypical carbenes would be of the form $(CO)_5M{=}CH_2$, $(CO)_4M{=}CH_2$, or $(CO)_3M{=}CH_2$, where M is a metal from group 6, 8, or 10, respectively. Transition metal carbonyl complexes are well-known both theoretically and experimentally,[132–135] making carbonyl ligands a logical choice to occupy the rest of the coordination sphere. The molecules that were initially studied in this research include $(CO)_5Cr{=}CH_2$, $(CO)_4Fe{=}CH_2$, and $(CO)_3Ni{=}CH_2$. We further consider second and third-row transition metals of groups 6, 8, and 10, namely $(CO)_5Mo{=}CH_2$, $(CO)_5W{=}CH_2$, $(CO)_4Ru{=}CH_2$, $(CO)_4Os{=}CH_2$, $(CO)_3Pd{=}CH_2$, and $(CO)_3Pt{=}CH_2$.

None of the transition metal carbenes investigated in this study has been synthesized experimentally. This is likely due to the high reactivity of the carbene carbon; the two hydrogens offer minimal steric hindrance to approach of potential coreactants.[130] Transition metal carbenes have been synthesized with larger R groups on the carbon.[136,137] Further, many molecules have been reported with M=CH_2 bonds. These are generally Schrock-type transition metal carbenes with ligands other than carbonyls surrounding the metal center. Schrock in 1975 isolated and characterized the first transition-metal methylene complex, Ta($\eta^5-C_5H_5)_2-(CH_3)(CH_2)$.[128] In 2015, Chen and coworkers proposed a complex with a Ni=CH_2 double bond as an intermediate in a nickel-catalyzed cyclopropanation scheme.[138] A 2017 study by Levine, Tilley, and Anderson found evidence for short-lived Y=CH_2 and Sc=CH_2 bonds.[139] The first structurally characterized alkilydenes of hexavalent chromium have recently been reported.[140]

The experimental study most closely related to this research is the photoionization mass spectrometry work of Beauchamp and coworkers on gas-phase $(CO)_5Mn^+=CH_2$,[141,142] isoelectronic to $(CO)_5Cr=CH_2$. A very substantial dissociation energy of 104 ± 3 kcal mol^{-1} was reported for this species. It should also be noted that the "naked" cationic M^+-CH_2 complexes of Cr, Fe, and Ni have been made in the gas phase, and experimental values for the bond energies have been reported to be 65 ± 7 kcal mol^{-1}, 96 ± 5 kcal mol^{-1}, and 86 ± 6 kcal mol^{-1}, respectively.[143]

The first theoretical study on one of these prototypical transition metal carbenes was in 1981 when Spangler et al. studied $(CO)_3Ni=CH_2$ at the SCF level of theory.[130] Optimized geometrical parameters for this molecule were compared to those obtained for the naked Ni=CH_2 and the homoleptic carbonyl $Ni(CO)_4$. The minimum energy structure was found to be of C_s symmetry with the CH_2 staggered with respect to all the carbonyls. In 1984, Taylor and Hall[144] used a generalized molecular orbital (GMO) approach to study a number of simple carbene systems, including

$(CO)_5Mo{=}CH_2$. A dissociation energy of 56 kcal mol^{-1} was computed for this complex. The C_{2v} staggered conformation was found to be the lowest energy structure. In 1992, Márquez and Fernández Sanz[145] studied the $(CO)_5Mo{=}CH_2$ complex using the complete active space self-consistent field (CASSCF) method. The system was not found to be significantly multireference, with a leading CAS coefficient (unsquared) of 0.94. In addition to optimized geometries and dissociation energies, Márquez and Fernández Sanz reported potential energy profiles for dissociation.

The most relevant theoretical studies on these transition metal carbene systems were done by the groups of Ziegler and Frenking starting in the mid-1990s. Ziegler and coworkers[146] studied the three group 6 metal complexes (Cr, Mo, W) using the local density approximation (LDA) and a triple-ζ Slater-type orbital (STO) basis set. They reported the effects of including nonlocal density corrections and relativistic effects on the bond lengths and energies. The chromium complex was also included as part of their 1995 study that examined a number of different chromium carbenes and silylenes.[147] The $Cr{=}CH_2$ bond was found to be the shortest of all the $Cr{-}CR_2$ and $Cr{-}SiR_2$ bonds studied, namely 1.88 Å. A later 1996 study by the Ziegler group found that this relatively short bond length is due to a strong energetic match between the metal 3d donor orbital and the acceptor orbital on the methylene carbon.[148]

In 1996, Frenking and coworkers[149] reported an *ab initio* study on the three group 6 (Cr, Mo, W) and three group 10 (Ni, Pd, Pt) transition metal carbene complexes. Optimized geometries were obtained at the MP2/6-31G(p) level of theory, and energies were obtained at the CCSD(T) level. In addition, charge decomposition analysis (CDA) was done to estimate the amount of donation and back-donation occurring from the ligand to the metal and vice versa. The CH_2 ligand was found to be both a strong electron donor and a strong electron acceptor. Vyboishchikov and Frenking (1998) analyzed the bonding of Fischer-type (e.g. $(CO)_5W{=}CR_2$) and Schrock-Type (e.g. $F_4W{=}CR_2$)

complexes of tungsten using the CDA method in addition to Bader's atoms in molecules (AIM) theory and the natural bond orbital (NBO) partitioning scheme.[150] They found that the metal–carbon bonding in the complex $(CO)_5W{=}CH_2$ can be interpreted as a Fischer-type donor-acceptor relationship as opposed to a traditional double bond.

In 2000, Frenking and coworkers studied $(CO)_4Fe{=}CH_2$ using the B3LYP/6-31G(d) method for geometry optimizations and CCSD(T) for energies.[151] The C_{2v} eclipsed structure with equatorial CH_2 was found to lie lower in energy than the C_s axial structure by around 8 kcal mol^{-1}. The $(CO)_4Fe{=}CH_2$ system was also studied in 2001 by Frenking and coworkers as part of a larger study on iron carbenes with various ligands.[152] Frenking and coworkers in 2002 revisited $(CO)_5Cr{=}CH_2$ as part of a larger study on the effects of changing the ligand on transition metal carbene complexes.[153] This study was done using the BP86 functional and a triple-ζ STO basis set. Frenking also published two helpful reviews in the 2000s on the bonding in transition-metal carbene complexes.[129,154] Several other theoretical studies exist that mention one or more of the complexes studied here.[155–158]

The classification of these prototypical transition metal carbenes as Fischer or Schrock carbenes is a bit ambiguous. Methylene is well-known to have a triplet ground state,[159] which taken on its own suggests that a Schrock-type double bond forms in these complexes between a triplet metal carbonyl fragment and a triplet methylene ligand. However, the metal centers studied here are middle to late transition metals with low oxidation states (0), which are more characteristic of the singlet-singlet donation/back-donation bonding of Fischer carbenes. Indeed, the literature generally classifies the carbenes considered here as Fischer carbenes.[146,150]

To date, no theoretical study exists that examines all nine transition metal carbenes considered here. The $(CO)_4Ru{=}CH_2$ and $(CO)_4Os{=}CH_2$ complexes in particular have never been studied theo-

retically. More importantly, none of these complexes has ever been made or studied experimentally. In addition to optimized geometries, M=CH_2 bond properties such as dissociation energies and vibrational frequencies will be predicted here. There is a lack of vibrational frequencies reported in the literature on these complexes, as none of the previous theoretical studies mentioned here report all of these values. Trends in these properties as the metal center is changed will be examined in terms of both top-to-bottom and left-to-right movement on the periodic table. We hope our results on the chemistry of these complexes will motivate experimental investigations.

The primary theoretical method that will be used in this research is density functional theory (DFT). There has been considerable development in DFT methods in the 15 years since the last theoretical studies on transition metal carbenes.[160] In particular, the M06-L, ωB97X, and related functionals have experienced considerable use and have been shown to perform well in numerous applications, including transition metal complexes.[161]

4.2 Theoretical Methods

For this study, we used five different DFT functionals, all of which are well-known and have been used extensively on transition metal systems: B3LYP, BP86, M06-L, ωB97X, and ωB97X-D3. B3LYP is a hybrid generalized gradient approximation (GGA) functional consisting of Becke's three-parameter exchange and the correlation functional of Lee, Yang, and Parr.[20,21] BP86 is a GGA functional consisting of Becke's 1988 exchange functional and Perdew's 1986 correlation functional.[20,23] M06-L, a meta-GGA functional, is from the Minnesota family of functionals and was designed to model transition metal bonding.[162] The ωB97X functional is a hybrid-meta GGA functional.[163] The last functional is ωB97X-D3, which is a re-optimization of ωB97X-D with an improved dispersion correction from Grimme.[164] ωB97X-D, a version of ωB97X with dispersion

effects included, has been shown to perform the best out of 25 functionals studied for geometry optimizations of transition metal complexes.[161] The ωB97X-D3 functional should be a further improvement over those results. The transition metal carbenes studied in this research are not expected to have significant long-range interactions. By comparing the results of ωB97X versus ωB97X-D3, any dispersion effects present can be monitored.

The cc-pVTZ basis set was used for all atoms except the second and third row transition metals, for which a cc-pVTZ-PP basis set was employed.[10] DFT is generally not as sensitive to basis set size as are wavefunction-based methods,[165] so cc-pVTZ should be sufficiently large to obtain reliable results. The use of the cc-pVTZ-PP basis set on the second and third row transition metals is due to the need for effective core potentials (ECPs) for these atoms. The use of ECPs allows for significant speedup in addition to the inclusion of relativistic effects. The relativistic ECPs of the Stuttgart group[166,167] were used in this work.

These computations were performed using the ORCA 4.0 software package.[168] The finest DFT grid setting was used, consisting of a Lebedev 770 point grid, to minimize integration grid errors.[169] For hybrid functionals, the RIJCOSX approximation[170,171] was used to speed up the computation of the Hartree-Fock exchange term.

4.3 Results and Discussion

The following sections explore the optimized geometries, metal-carbene dissociation energies, and metal-carbene stretching frequencies obtained for the nine complexes considered here. All carbene complexes were determined to have singlet ground states. These singlet states generally were found to be at least 20 kcal mol^{-1} lower in energy than the analogous triplet states. The

complex with the closest singlet-triplet splitting was $(CO)_3Pd{=}CH_2$ for which this gap was found to be 2 kcal mol^{-1}.

4.3.1 Optimized Geometries

Figure 4.2: Optimized geometries (B3LYP/cc-pVTZ) of $(CO)_5M{=}CH_2$ (M = Cr, Mo, W) complexes. Relevant geometrical parameters are given in Table 4.1

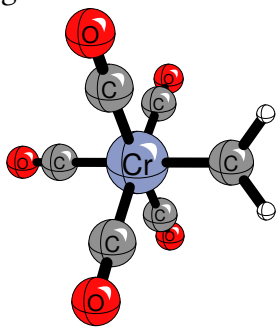

$(CO)_5Cr{=}CH_2$

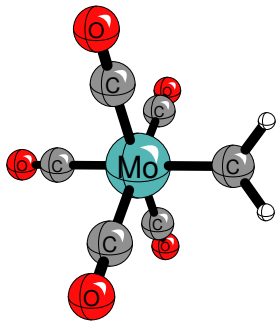

$(CO)_5Mo{=}CH_2$

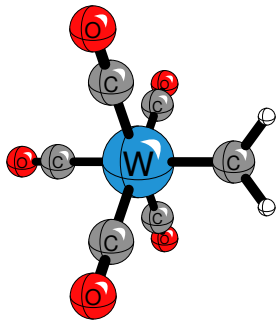

$(CO)_5W{=}CH_2$

Optimized structures for the nine transition metal carbene complexes are shown in Figures 4.2, 4.3, 4.4 for the complexes of metals in groups 6, 8, or 10, respectively. The figures shown were

Figure 4.3: Optimized geometries (B3LYP/cc-pVTZ) of $(CO)_4M{=}CH_2$ (M = Fe, Ru, Os) complexes. Relevant geometrical parameters are given in Table 4.2

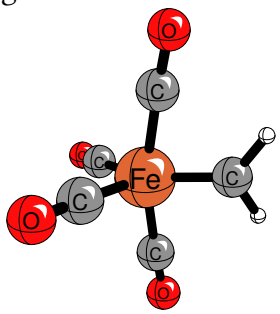

$(CO)_4Fe{=}CH_2$

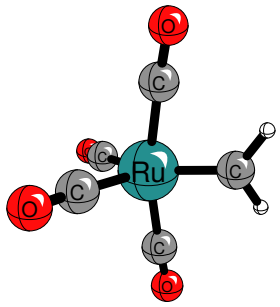

$(CO)_4Ru{=}CH_2$

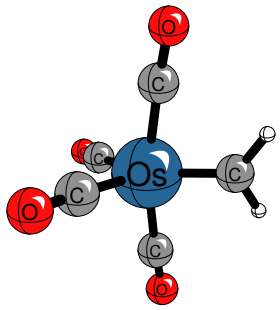

$(CO)_4Os{=}CH_2$

Figure 4.4: Optimized geometries (B3LYP/cc-pVTZ) of $(CO)_3M{=}CH_2$ (M = Ni, Pd, Pt) complexes. Relevant geometrical parameters are given in Table 4.3

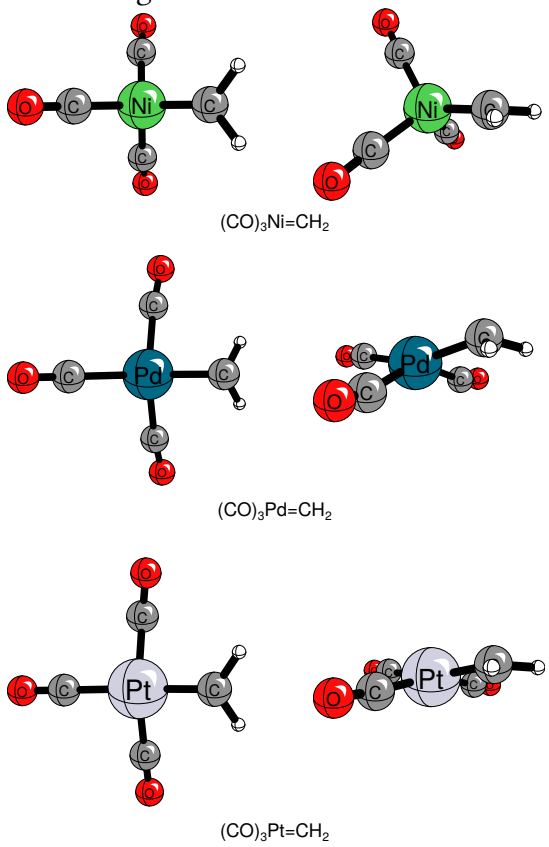

$(CO)_3Ni{=}CH_2$

$(CO)_3Pd{=}CH_2$

$(CO)_3Pt{=}CH_2$

Table 4.1: Optimized bond distances (angstroms) and methylene rotation dihedral angles (degrees) in $(CO)_5M{=}CH_2$ (M = Cr, Mo, W) complexes from five DFT functionals. Structures are shown in Figure 4.2. The subscript “cis" refers to the four equivalent carbonyls, while “trans" refers to the one carbonyl opposite the methylene.

	B3LYP	BP86	M06-L	ωB97X	ωB97X-D3
Cr–C_m	1.91	1.92	1.91	1.89	1.89
Cr–C_{cis}	1.93	1.91	1.92	1.92	1.91
Cr–C_{trans}	1.96	1.94	1.96	1.96	1.95
C_m–H	1.09	1.10	1.09	1.10	1.09
C_{cis}–O	1.14	1.15	1.14	1.14	1.14
C_{trans}–O	1.14	1.15	1.14	1.13	1.13
∠(H-C_m-Cr-C_{cis})	44.1	43.5	43.5	44.1	44.0
Mo–C_m	2.04	2.05	2.04	2.01	2.02
Mo–C_{cis}	2.08	2.07	2.08	2.08	2.07
Mo–C_{trans}	2.13	2.11	2.14	2.14	2.13
C–H	1.09	1.10	1.10	1.09	1.09
C_{cis}–O	1.14	1.15	1.14	1.14	1.14
C_{trans}–O	1.14	1.15	1.14	1.13	1.13
∠(H-C_m-Mo-C_{cis})	43.9	43.2	42.9	43.8	43.8
W–C_m	2.05	2.06	2.05	2.03	2.03
W–C_{cis}	2.08	2.07	2.08	2.07	2.07
W–C_{trans}	2.12	2.11	2.12	2.12	2.11
C–H	1.09	1.10	1.09	1.09	1.09
C_{cis}–O	1.14	1.16	1.15	1.14	1.14
C_{trans}–O	1.14	1.15	1.14	1.14	1.14
∠(H-C_m-W-C_{cis})	43.7	43.1	42.8	43.6	43.7

Table 4.2: Optimized bond distances (angstroms) in $(CO)_4M{=}CH_2$ (M = Fe, Ru, Os) complexes from five DFT functionals. Structures are shown in Figure 4.3. The subscript “cis" refers to the two equivalent axial carbonyls bent toward the methylene, while “trans" refers to the two carbonyls oriented away from the methylene.

	B3LYP	BP86	M06-L	ωB97X	ωB97X-D3
Fe–C_m	1.84	1.85	1.84	1.82	1.82
Fe–C_{cis}	1.82	1.80	1.82	1.81	1.81
Fe–C_{trans}	1.82	1.81	1.82	1.82	1.81
C_m–H	1.09	1.10	1.09	1.09	1.09
C_{cis}–O	1.14	1.15	1.14	1.13	1.13
C_{trans}–O	1.14	1.15	1.14	1.13	1.13
Ru–C_m	1.95	1.96	1.95	1.93	1.93
Ru–C_{cis}	1.96	1.95	1.96	1.96	1.95
Ru–C_{trans}	1.96	1.95	1.96	1.96	1.95
C_m–H	1.09	1.10	1.09	1.09	1.09
C_{cis}–O	1.14	1.15	1.14	1.13	1.13
C_{trans}–O	1.14	1.15	1.14	1.14	1.14
Os–C_m	1.97	1.97	1.97	1.95	1.95
Os–C_{cis}	1.97	1.96	1.96	1.96	1.96
Os–C_{trans}	1.96	1.95	1.95	1.95	1.95
C_m–H	1.09	1.09	1.09	1.09	1.09
C_{cis}–O	1.14	1.15	1.14	1.13	1.13
C_{trans}–O	1.14	1.16	1.15	1.14	1.14

Table 4.3: Optimized bond distances (angstroms) and angles (degrees) in $(CO)_3M{=}CH_2$ (M = Ni, Pd, Pt) complexes from five DFT functionals. Structures are shown in Figure 4.4. The subscript "trans" refers to the carbonyl lying in the reflection plane of symmetry, while "cis" refers to the two equivalent carbonyls lying outside the reflection plane.

	B3LYP	BP86	M06-L	ωB97X	ωB97X-D3
Ni–C_m	1.83	1.83	1.83	1.81	1.81
Ni–C_{trans}	1.82	1.81	1.82	1.82	1.81
Ni–C_{cis}	1.86	1.83	1.85	1.86	1.85
C_m–H	1.09	1.10	1.10	1.10	1.10
C_{trans}–O	1.14	1.15	1.14	1.13	1.13
C_{cis}–O	1.14	1.15	1.14	1.13	1.13
∠(C_m-Ni-C_{trans})	123.4	122.8	123.4	121.2	121.7
∠(H-C_m-Ni-C_{cis})	23.7	22.6	21.9	26.3	25.7
Pd–C_m	2.07	2.05	2.07	2.05	2.05
Pd–C_{trans}	2.16	2.10	2.17	2.19	2.17
Pd–C_{cis}	2.12	2.06	2.12	2.17	2.14
C_m–H	1.10	1.10	1.10	1.10	1.10
C_{trans}–O	1.13	1.15	1.14	1.13	1.13
C_{cis}–O	1.13	1.15	1.14	1.13	1.13
∠(C_m-Pd-C_{trans})	158.0	158.8	160.3	153.8	153.7
∠(H-C_m-Pd-C_{cis})	-7.9	-8.8	-11.3	-1.8	-2.1
Pt–C_m	1.96	1.96	1.97	1.93	1.94
Pt–C_{trans}	1.97	1.95	1.96	1.96	1.96
Pt–C_{cis}	1.93	1.92	1.93	1.93	1.93
C_m–H	1.08	1.09	1.09	1.09	1.09
C_{trans}–O	1.14	1.15	1.14	1.13	1.13
C_{cis}–O	1.14	1.15	1.14	1.13	1.13
∠(C_m-Pt-C_{trans})	166.4	165.8	166.5	165.7	165.7
∠(H-C_m-Pt-C_{cis})	-1.2	-0.3	-2.4	-0.7	-0.5

generated from B3LYP coordinates, but all five functionals gave the same general structures. The most relevant bond and angle parameters for the group 6, group 8, and group 10 complexes are given in Tables 4.1, 4.2, and 4.3, respectively.

The group 6 complexes of Cr, Mo, and W were found to exhibit C_{2v} minima where the methylene group is staggered with respect to the carbonyls. We distinguish between the carbonyl carbons by referring to the four equivalent carbonyl carbons as C_{cis} and the carbon in the rotational axis across from the methylene group as C_{trans}. There is little variation in the general structure between the complexes of the group 6 metals. The octahedral coordination remains largely unchanged moving to the metals lower on the periodic table. The largest difference between the complexes is in the bond distances. The M–C distances for the compounds of Mo and W are around 0.1-0.2 Å longer than the corresponding bonds from the Cr complex.

The group 8 complexes also have C_{2v} minimum energy structures. These complexes exhibit trigonal-bipyramidal-type structures, where the two axial carbonyls are slightly bent towards the methylene. The methylene group prefers the equatorial position where the hydrogens are rotated to be eclipsed with respect to the two nearest carbonyls. We label these two axial carbonyls as C_{cis} and the two equatorial carbonyls as C_{trans}. Similarly to the group 6 complexes, the structures are relatively unchanged as the metal center is changed. The main difference between the complexes is that the complexes of Ru and Os both have M–C bond distances that are about 0.10 to 0.15 Å longer than the Fe complex.

The group 10 minimum energy structures are of C_s symmetry. The methylene group in the Ni complex is rotated to be staggered with respect to all the carbonyls. We label the carbonyl carbon that lies in the plane of reflection as C_{trans}, and the carbons out of the plane of symmetry are labeled C_{cis}. In contrast to the group 6 and group 8 complexes, the group 10 complexes exhibit

significant structural changes as the metal center is changed. While the Ni complex has a roughly tetrahedral-type structure, the Pd and Pt complexes are significantly flatter, with the Pt complex being nearly planar. The methylene in these flatter complexes is rotated to be essentially eclipsed with respect to the cis carbonyls.

A referee has noted the existence of another conformer of the Pd complex with a shorter M–C_m bond and one long M–CO bond. We have found this conformer with four of the five DFT functionals (B3LYP, M06-L, ωB97X, ωB97X-D3). The Pd–C_{trans} bond in this conformer was found to range from 2.9-3.3 Å, and the relative electronic energy compared to the standard Pd conformer ranges from −1.8 to +0.5 kcal mol^{-1}.

The five functionals are in general agreement on the geometrical parameters in Tables 4.1, 4.2, and 4.3. For a given complex, the M=C distances never differ by more than a few hundredths of an angstrom between functionals. The inclusion of dispersion for the ωB97X-D3 functional does not appear to make a large difference; the bond distances from ωB97X and ωB97X-D3 are never more than 0.01 Å different. This result makes sense, as these complexes are not expected to exhibit significant long-range effects that would influence their bonding.

The metal–methylene bond distances for all nine complexes are compared in Table 4.4. The ωB97X and ωB97X-D3 functionals tend to be shorter than those obtained by the other functionals by around 0.02 Å, while the other three agree with each other. In general, the M=CH_2 bond distances increase going down a given group in the periodic table and decrease going to the right across a row. The big exception to these trends is the $(CO)_3$Pd=CH_2 complex, for which the longest M=CH_2 distance of 2.07 Å was found with B3LYP and M06-L.

Table 4.4: $M{=}CH_2$ bond lengths (Å) in transition metal carbene complexes from five DFT functionals.

	$Cr{=}CH_2$	$Fe{=}CH_2$	$Ni{=}CH_2$
B3LYP	1.91	1.84	1.83
BP86	1.92	1.85	1.83
M06-L	1.91	1.84	1.83
ωB97X	1.89	1.82	1.81
ωB97X-D3	1.89	1.82	1.81
	$Mo{=}CH_2$	$Ru{=}CH_2$	$Pd{=}CH_2$
B3LYP	2.04	1.95	2.07
BP86	2.05	1.96	2.05
M06-L	2.04	1.95	2.07
ωB97X	2.01	1.93	2.05
ωB97X-D3	2.02	1.93	2.05
	$W{=}CH_2$	$Os{=}CH_2$	$Pt{=}CH_2$
B3LYP	2.05	1.97	1.96
BP86	2.06	1.97	1.96
M06-L	2.05	1.97	1.97
ωB97X	2.03	1.95	1.93
ωB97X-D3	2.03	1.95	1.94

4.3.2 Dissociation Energies

Dissociation energies for the $M{=}CH_2$ bond in the nine transition metal carbenes are reported in Figure 4.5 and Table 4.5. These dissociation energies were computed using the ground state energies of each of the fragments involved. The transition metal carbenes and the transition metal carbonyl fragments were computed as singlets, while methylene was computed as a triplet. This method of computing dissociation energies agrees with the methods used by Taylor and Hall[144] and by Frenking,[149] but is different from the methods used by Márquez and Fernández Sanz[145] and by Ziegler,[146] who take into account conservation of spin for the dissociating fragments. Such methods compute the dissociation energy using the lowest singlet state of methylene, which lies around 9 kcal mol^{-1} higher in energy than the ground state triplet. Dissociation energies from

Figure 4.5: $M{=}CH_2$ dissociation energies (kcal mol^{-1}) in transition metal carbene complexes from five DFT functionals.

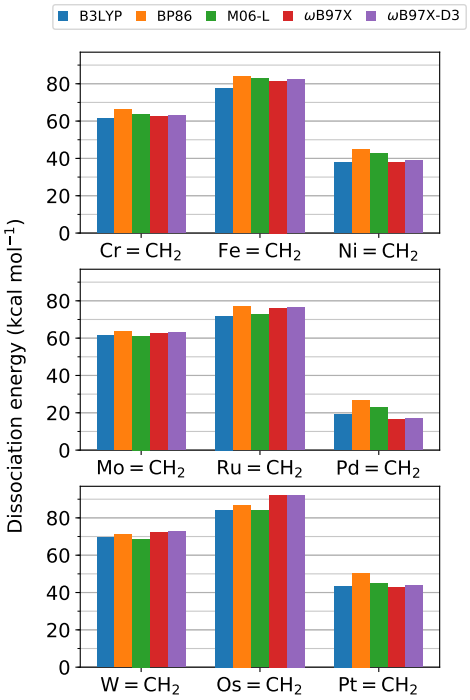

Table 4.5: $M{=}CH_2$ dissociation energies (kcal mol^{-1}) in transition metal carbene complexes from five DFT functionals.

	$Cr{=}CH_2$	$Fe{=}CH_2$	$Ni{=}CH_2$
B3LYP	61.3	77.6	37.8
BP86	66.4	83.8	45.0
M06-L	63.3	83.0	42.7
wB97X	62.3	81.5	37.8
wB97X-D3	63.2	82.5	38.7
	$Mo{=}CH_2$	$Ru{=}CH_2$	$Pd{=}CH_2$
B3LYP	61.4	71.9	18.9
BP86	63.5	76.8	26.7
M06-L	61.1	72.8	22.7
wB97X	62.4	75.9	16.4
wB97X-D3	62.9	76.6	17.0
	$W{=}CH_2$	$Os{=}CH_2$	$Pt{=}CH_2$
B3LYP	69.6	84.3	43.4
BP86	71.0	86.8	50.4
M06-L	68.7	84.0	44.8
wB97X	72.1	92.3	42.7
wB97X-D3	72.7	92.3	43.7

these spin-conserving methods will be inherently shifted around 9 kcal mol^{-1} higher than the dissociation energies reported here.

There is more variation between functionals for the computation of dissociation energies than for the geometrical parameters. While the five functionals give the same general trends and conclusions, the dissociation energies for a given system can vary by over 10 kcal mol^{-1} depending on the functional used. These discrepancies are most significant for the weakly bound $(CO)_3Pd{=}CH_2$ complex, the difference between the dissociation computed from ωB97X (16.4 kcal mol^{-1}) and BP86 (26.7 kcal mol^{-1}) is 10.3 kcal mol^{-1}, a significant variation for an energy on the order of 20 kcal mol^{-1}. The BP86 functional overall tends to produce the highest dissociation energies, while B3LYP tends to be the lowest. The ωB97X and ωB97X-D3 functionals produce

nearly the same energies. The dispersion effects included in ωB97X-D3 lead to slightly larger dissociation energies than ωB97X, but by no more than 1 kcal mol^{-1}.

The dissociation energies follow the trend of group 8 > group 6 > group 10 for a given row on the periodic table. In addition, the general trend of row 3 > row 1 > row 2 is followed. The $(CO)_3Pd{=}CH_2$ complex once again is an outlier here with a dissociation energy of around 20 kcal mol^{-1}, which is by far the lowest of all complexes reported here. This low dissociation energy combined with the relatively long $M{=}CH_2$ bond length suggest that this complex is the least likely to be synthesized in the near future. The $(CO)_4Os{=}CH_2$ complex has the overall highest dissociation energies computed with a value of up to 92.3 kcal mol^{-1} from ωB97X-D3.

4.3.3 Vibrational Frequencies

The $M{=}CH_2$ stretching frequencies are reported in Table 4.6. Two vibrational modes for the $(CO)_5Cr{=}CH_2$ and $(CO)_5Mo{=}CH_2$ complexes correspond to $M{=}CH_2$ stretching, and both are reported. In both of these complexes, neither of these vibrational modes is a pure $M{=}CH_2$ stretch; rather, this stretching mode is coupled to umbrella-type bending motions of the equatorial carbons. For the rest of the molecules, a single obvious mode corresponds to the $M{=}CH_2$ stretch.

The five functionals qualitatively agree with each other for the $M{=}CH_2$ stretching frequency. While the B3LYP, BP86, and M06-L frequencies are generally within around 10 cm^{-1} of each other, the ωB97X and ωB97X-D3 functionals are generally around 50 cm^{-1} higher.

The frequency results do not exhibit clear periodic trends as did the bond lengths and dissociation energies. The $(CO)_3Pd{=}CH_2$ complex does have the lowest $M{=}CH_2$ stretching frequency in the range of 505-532 cm^{-1}, which is unsurprising given its long $M{=}CH_2$ bond and low dissocia-

tion energy. The $(CO)_4Fe{=}CH_2$ complex is expected to have the largest frequency with a range of 710-770 cm^{-1}.

Insight into the bonding in transition metal carbene complexes may be gained also from considering the normal modes involving the carbonyls in these complexes. Tolman's electronic parameter (TEP), determined from the totally symmetric CO stretching mode of $(CO)_3Ni{-}L$ complexes, has been used as an estimator of the electron donating ability of a ligand.[158,172] The CO stretching frequency of the carbonyl in the *trans* position to the carbene ligand has also been used as a monitor of the electronic properties of the ligand.

Table 4.6: $M{=}CH_2$ stretching vibrational frequencies (cm^{-1}) in transition metal carbene complexes from five different DFT functionals. Values separated by a slash indicate cases where two $M{=}CH_2$ stretching frequencies were found.

	$Cr{=}CH_2$	$Fe{=}CH_2$	$Ni{=}CH_2$
B3LYP	599/695	718	644
BP86	597/690	710	649
M06-L	598/686	710	629
ωB97X	615/730	770	670
ωB97X-D3	618/732	765	670
	$Mo{=}CH_2$	$Ru{=}CH_2$	$Pd{=}CH_2$
B3LYP	572/623	691	505
BP86	564/615	678	532
M06-L	570/615	685	507
ωB97X	575/651	732	516
ωB97X-D3	578/650	729	520
	$W{=}CH_2$	$Os{=}CH_2$	$Pt{=}CH_2$
B3LYP	622	717	687
BP86	614	703	675
M06-L	610	713	673
ωB97X	661	758	726
ωB97X-D3	659	755	727

4.4 Conclusions

This work reports a theoretical study on nine prototypical transition metal carbenes. The five DFT functionals used generally agree for the quantities studied here. The largest discrepancies between functionals are in the dissociation energies, for which discrepancies of up to 10 kcal mol^{-1} were found. The $(CO)_3Pd{=}CH_2$ complex is an outlier in the group for every quantity studied, with the longest $M{=}CH_2$ bond length, lowest dissociation energy, and smallest $M{=}CH_2$ stretching frequency. It is expected to be the most weakly bound of all these compounds. $M{=}CH_2$ distances were found to increase down a column on the periodic table and decrease from left to right across a row. The dissociation energies, meanwhile, are largest for the group 8 complexes of Fe, Ru, and Os, followed by the group 6 and group 10 complexes. We hope this theoretical characterization of metal-carbene compounds incites interest in their synthesis from the experimental chemistry community.

Chapter 5

Conclusion

This work describes quantum chemical studies into molecular systems relevant to combustion chemistry, atmospheric chemistry, and organometallic chemistry. The reactions of O_2 with the unsubstituted vinoxy radical and the acetonyl radical are prototypes for the reactions of larger vinoxy radicals with O_2. These reactions have been studied to a high degree of accuracy using the rigorous focal point method. For the unsubstituted vinoxy + O_2 system, the lowest energy isomerization pathway forms a peroxy radical that undergoes a 1-4 H shift to form a hydroperoxyacyl radical. The hydroperoxyacyl radical is then predicted to dissociate into formaldehyde, carbon monoxide, and hydroxy radical. For the acetonyl + O_2 system, no submerged pathways to product formation were found. For both of these systems, the O_2 addition entrance channel was found to be barrierless from multireference computations.

The prototypical transition metal carbenes serve as models for examining the nature of the metal–carbon double bond in organometallic chemistry. Transition metal methylene complexes of group 6, 8, and 10 have been studied using five different DFT functionals. All five functionals show general agreement in regards to geometries, dissociation energies, and vibrational frequencies. The group 10 complexes are the most weakly bound with dissociation energies as low as ≈20 kcal

mol^{-1} for $(CO)_3Pd{=}CH_2$. The group 8 complexes are predicted to be the most worthy targets for experimental synthesis with dissociation energies as high as ≈90 kcal $mol^{-1}$for $(CO)_4Os{=}CH_2$.

Appendix A

Focal Point Tables for Vinoxy Radical + O_2 Molecules

Table A.1: Focal point table for **PRa**.

	HF	$+\delta$MP2	$+\delta$CCSD	$+\delta$CCSD(T)	NET
cc-pVDZ	−21.82	+16.98	−15.39	−0.16	[−20.40]
cc-pVTZ	−22.61	+14.46	−16.02	−0.41	[−24.59]
cc-pVQZ	−22.33	+13.49	−16.29	−0.52	[−25.64]
cc-pV5Z	−22.24	+13.03	−16.35	−0.55	[−26.10]
CBS LIMIT	[−22.21]	[+12.55]	[−16.41]	[−0.58]	[−26.64]

$$\Delta H_{0\mathrm{K}} = \Delta E_e + \Delta_{\mathrm{T(Q)}} + \Delta_{\mathrm{CORE}} + \Delta_{\mathrm{REL}} + \Delta_{\mathrm{DBOC}} + \Delta_{\mathrm{ZPVE}}$$

$$\Delta H_{0\mathrm{K}} = -26.64 + 0.298 + 0.228 + 0.329 - 0.050 + 3.938 = \mathbf{-21.9}$$

Table A.2: Focal point table for **PRb**.

	HF	$+\delta$MP2	$+\delta$CCSD	$+\delta$CCSD(T)	NET
cc-pVDZ	−21.23	+17.91	−15.37	+0.01	[−18.67]
cc-pVTZ	−22.07	+15.32	−15.99	−0.20	[−22.95]
cc-pVQZ	−21.82	+14.37	−16.28	−0.29	[−24.03]
cc-pV5Z	−21.74	+13.92	−16.34	−0.32	[−24.49]
CBS LIMIT	[−21.71]	[+13.45]	[−16.40]	[−0.36]	[−25.02]

$$\Delta H_{0\mathrm{K}} = \Delta E_e + \Delta_{\mathrm{T(Q)}} + \Delta_{\mathrm{CORE}} + \Delta_{\mathrm{REL}} + \Delta_{\mathrm{DBOC}} + \Delta_{\mathrm{ZPVE}}$$

$$\Delta H_{0\mathrm{K}} = -25.02 - 0.359 + 0.212 + 0.338 - 0.047 + 3.651 = \mathbf{-20.5}$$

Table A.3: Focal point table for **PRc**.

	HF	$+\delta$MP2	$+\delta$CCSD	$+\delta$CCSD(T)	NET
cc-pVDZ	−20.81	+17.20	−15.16	−0.11	[−18.88]
cc-pVTZ	−21.57	+14.85	−15.83	−0.34	[−22.89]
cc-pVQZ	−21.29	+13.94	−16.12	−0.43	[−23.90]
cc-pV5Z	−21.20	+13.51	−16.19	−0.47	[−24.34]
CBS Limit	[−21.15]	[+13.05]	[−16.26]	[−0.50]	[−24.86]

$$\Delta H_{0\mathrm{K}} = \Delta E_e + \Delta_{\mathrm{T(Q)}} + \Delta_{\mathrm{CORE}} + \Delta_{\mathrm{REL}} + \Delta_{\mathrm{DBOC}} + \Delta_{\mathrm{ZPVE}}$$

$$\Delta H_{0\mathrm{K}} = -24.86 + 0.355 + 0.215 + 0.329 - 0.048 + 4.009 = \mathbf{-20.0}$$

Table A.4: Focal point table for **PRd**.

	HF	$+\delta$MP2	$+\delta$CCSD	$+\delta$CCSD(T)	NET
cc-pVDZ	−19.27	+16.78	−15.14	−0.04	[−17.67]
cc-pVTZ	−20.24	+14.36	−15.77	−0.28	[−21.93]
cc-pVQZ	−20.05	+13.48	−16.07	−0.37	[−23.01]
cc-pV5Z	−19.97	+13.06	−16.14	−0.41	[−23.45]
CBS Limit	[−19.93]	[+12.63]	[−16.21]	[−0.44]	[−23.95]

$$\Delta H_{0\mathrm{K}} = \Delta E_e + \Delta_{\mathrm{T(Q)}} + \Delta_{\mathrm{CORE}} + \Delta_{\mathrm{REL}} + \Delta_{\mathrm{DBOC}} + \Delta_{\mathrm{ZPVE}}$$

$$\Delta H_{0\mathrm{K}} = -23.95 + 0.350 + 0.211 + 0.330 - 0.043 + 3.828 = \mathbf{-19.3}$$

Table A.5: Focal point table for **TS1**.

	HF	$+\delta$MP2	$+\delta$CCSD	$+\delta$CCSD(T)	NET
cc-pVDZ	31.32	−13.04	−8.99	−4.34	[+4.95]
cc-pVTZ	31.01	−16.58	−8.89	−5.41	[+0.13]
cc-pVQZ	31.43	−17.87	−8.93	−5.69	[−1.06]
cc-pV5Z	31.59	−18.42	−8.93	−5.78	[−1.53]
CBS LIMIT	[31.67]	[−18.99]	[−8.92]	[−5.88]	[−2.12]

$$\Delta H_{0\mathrm{K}} = \Delta E_e + \Delta_{\mathrm{T(Q)}} + \Delta_{\mathrm{CORE}} + \Delta_{\mathrm{REL}} + \Delta_{\mathrm{DBOC}} + \Delta_{\mathrm{ZPVE}}$$

$$\Delta H_{0\mathrm{K}} = -2.12 - 0.149 + 0.356 + 0.300 + 0.000 + 0.936 = \mathbf{-0.7}$$

Table A.6: Focal point table for **TS2**.

	HF	$+\delta$MP2	$+\delta$CCSD	$+\delta$CCSD(T)	NET
cc-pVDZ	42.49	−5.69	−9.27	−3.35	[+24.18]
cc-pVTZ	42.61	−10.44	−8.61	−4.16	[+19.41]
cc-pVQZ	43.21	−11.74	−8.57	−4.42	[+18.48]
cc-pV5Z	43.36	−12.28	−8.54	−4.49	[+18.05]
CBS LIMIT	[43.41]	[−12.84]	[−8.51]	[−4.58]	[+17.48]

$$\Delta H_{0\mathrm{K}} = \Delta E_e + \Delta_{\mathrm{T(Q)}} + \Delta_{\mathrm{CORE}} + \Delta_{\mathrm{REL}} + \Delta_{\mathrm{DBOC}} + \Delta_{\mathrm{ZPVE}}$$

$$\Delta H_{0\mathrm{K}} = +17.48 - 0.075 - 0.286 - 0.198 + 0.011 - 0.101 = \mathbf{+16.8}$$

Table A.7: Focal point table for **TS3**.

	HF	$+\delta$MP2	$+\delta$CCSD	$+\delta$CCSD(T)	NET
cc-pVDZ	63.89	−25.34	−3.94	−7.79	[+26.83]
cc-pVTZ	64.95	−29.47	−1.93	−9.17	[+24.38]
cc-pVQZ	65.20	−30.66	−1.48	−9.46	[+23.60]
cc-pV5Z	65.28	−31.08	−1.29	−9.55	[+23.36]
CBS Limit	[65.31]	[−31.53]	[−1.08]	[−9.64]	[+23.07]

$$\Delta H_{0\mathrm{K}} = \Delta E_e + \Delta_{\mathrm{T(Q)}} + \Delta_{\mathrm{CORE}} + \Delta_{\mathrm{REL}} + \Delta_{\mathrm{DBOC}} + \Delta_{\mathrm{ZPVE}}$$

$$\Delta H_{0\mathrm{K}} = +23.07 - 0.931 + 0.285 + 0.247 + 0.049 - 1.165 = \mathbf{+21.6}$$

Table A.8: Focal point table for **QR1a**.

	HF	$+\delta$MP2	$+\delta$CCSD	$+\delta$CCSD(T)	NET
cc-pVDZ	−11.41	+2.31	−7.61	−1.06	[−17.77]
cc-pVTZ	−12.66	−1.67	−7.21	−1.68	[−23.22]
cc-pVQZ	−12.49	−3.25	−7.17	−1.83	[−24.74]
cc-pV5Z	−12.40	−3.98	−7.09	−1.88	[−25.35]
CBS LIMIT	[−12.35]	[−4.75]	[−7.00]	[−1.93]	[−26.03]

$$\Delta H_{0\mathrm{K}} = \Delta E_e + \Delta_{\mathrm{T(Q)}} + \Delta_{\mathrm{CORE}} + \Delta_{\mathrm{REL}} + \Delta_{\mathrm{DBOC}} + \Delta_{\mathrm{ZPVE}}$$

$$\Delta H_{0\mathrm{K}} = -26.03 + 0.432 + 0.303 + 0.369 - 0.102 + 4.048 = \mathbf{-21.0}$$

Table A.9: Focal point table for **QR1b**.

	HF	$+\delta$MP2	$+\delta$CCSD	$+\delta$CCSD(T)	NET
cc-pVDZ	−10.38	+2.43	−7.66	−0.94	[−16.56]
cc-pVTZ	−11.96	−1.36	−7.28	−1.51	[−22.11]
cc-pVQZ	−11.89	−2.84	−7.24	−1.64	[−23.61]
cc-pV5Z	−11.83	−3.53	−7.16	−1.68	[−24.19]
CBS LIMIT	[−11.79]	[−4.26]	[−7.07]	[−1.72]	[−24.83]

$$\Delta H_{0\mathrm{K}} = \Delta E_e + \Delta_{\mathrm{T(Q)}} + \Delta_{\mathrm{CORE}} + \Delta_{\mathrm{REL}} + \Delta_{\mathrm{DBOC}} + \Delta_{\mathrm{ZPVE}}$$

$$\Delta H_{0\mathrm{K}} = -24.83 + 0.421 + 0.299 + 0.369 - 0.094 + 3.607 = \mathbf{-20.2}$$

Table A.10: Focal point table for **QR1c**.

	HF	$+\delta$MP2	$+\delta$CCSD	$+\delta$CCSD(T)	NET
cc-pVDZ	−9.55	+3.28	−7.98	−0.87	[−15.12]
cc-pVTZ	−11.11	−0.64	−7.55	−1.44	[−20.73]
cc-pVQZ	−11.07	−2.18	−7.49	−1.58	[−22.31]
cc-pV5Z	−11.02	−2.91	−7.39	−1.62	[−22.94]
CBS LIMIT	[−10.99]	[−3.67]	[−7.30]	[−1.67]	[−23.62]

$$\Delta H_{0\mathrm{K}} = \Delta E_e + \Delta_{\mathrm{T(Q)}} + \Delta_{\mathrm{CORE}} + \Delta_{\mathrm{REL}} + \Delta_{\mathrm{DBOC}} + \Delta_{\mathrm{ZPVE}}$$

$$\Delta H_{0\mathrm{K}} = -23.62 + 0.422 + 0.305 + 0.371 - 0.092 + 3.506 = \mathbf{-19.1}$$

Table A.11: Focal point table for **QR1d**.

	HF	$+\delta$MP2	$+\delta$CCSD	$+\delta$CCSD(T)	NET
cc-pVDZ	−7.91	+1.36	−7.20	−0.99	[−14.73]
cc-pVTZ	−9.54	−2.57	−6.76	−1.62	[−20.50]
cc-pVQZ	−9.51	−4.12	−6.71	−1.78	[−22.12]
cc-pV5Z	−9.48	−4.86	−6.61	−1.84	[−22.79]
CBS LIMIT	[−9.46]	[−5.63]	[−6.51]	[−1.90]	[−23.50]

$$\Delta H_{0\mathrm{K}} = \Delta E_e + \Delta_{\mathrm{T(Q)}} + \Delta_{\mathrm{CORE}} + \Delta_{\mathrm{REL}} + \Delta_{\mathrm{DBOC}} + \Delta_{\mathrm{ZPVE}}$$

$$\Delta H_{0\mathrm{K}} = -23.50 + 0.420 + 0.297 + 0.365 - 0.097 + 3.731 = \mathbf{-18.8}$$

Table A.12: Focal point table for **TS4**.

	HF	$+\delta$MP2	$+\delta$CCSD	$+\delta$CCSD(T)	NET
cc-pVDZ	1.38	+4.55	−10.98	−1.49	[−6.54]
cc-pVTZ	0.18	+1.79	−10.35	−2.07	[−10.46]
cc-pVQZ	0.41	+0.73	−10.29	−2.19	[−11.34]
cc-pV5Z	0.59	+0.12	−10.20	−2.23	[−11.72]
CBS LIMIT	[0.70]	[−0.52]	[−10.11]	[−2.27]	[−12.20]

$$\Delta H_{0\mathrm{K}} = \Delta E_e + \Delta_{\mathrm{T(Q)}} + \Delta_{\mathrm{CORE}} + \Delta_{\mathrm{REL}} + \Delta_{\mathrm{DBOC}} + \Delta_{\mathrm{ZPVE}}$$

$$\Delta H_{0\mathrm{K}} = -12.2 + 0.158 + 0.645 + 0.266 - 0.073 + 1.521 = \mathbf{-9.7}$$

Table A.13: Focal point table for **TS5**.

	HF	$+\delta$MP2	$+\delta$CCSD	$+\delta$CCSD(T)	NET
cc-pVDZ	27.69	−5.33	−8.62	−3.36	[+10.38]
cc-pVTZ	27.33	−10.97	−8.08	−4.36	[+3.92]
cc-pVQZ	27.55	−12.83	−7.97	−4.72	[+2.03]
cc-pV5Z	27.64	−13.64	−7.87	−4.87	[+1.26]
CBS LIMIT	[27.68]	[−14.50]	[−7.76]	[−5.02]	[+0.41]

$$\Delta H_{0\mathrm{K}} = \Delta E_e + \Delta_{\mathrm{T(Q)}} + \Delta_{\mathrm{CORE}} + \Delta_{\mathrm{REL}} + \Delta_{\mathrm{DBOC}} + \Delta_{\mathrm{ZPVE}}$$

$$\Delta H_{0\mathrm{K}} = 0.41 - 0.364 + 0.219 + 0.282 - 0.071 + 1.584 = \mathbf{+2.1}$$

Table A.14: Focal point table for $^{\bullet}CH_2OOH$ + CO.

	HF	$+\delta$MP2	$+\delta$CCSD	$+\delta$CCSD(T)	NET
cc-pVDZ	−15.05	+15.23	−12.36	+0.18	[−12.01]
cc-pVTZ	−16.85	+14.09	−11.96	+0.00	[−14.71]
cc-pVQZ	−16.96	+13.61	−11.94	+0.04	[−15.26]
cc-pV5Z	−16.88	+13.21	−11.86	+0.05	[−15.48]
CBS LIMIT	[−16.80]	[+12.79]	[−11.78]	[+0.06]	[−15.72]

$\Delta H_{0K} = \Delta E_e + \Delta_{T(Q)} + \Delta_{CORE} + \Delta_{REL} + \Delta_{DBOC} + \Delta_{ZPVE}$

ΔH_{0K} = −15.72 + 0.265 + 0.569 + 0.231 − 0.075 − 0.329 = **−15.1**

Table A.15: Focal point table for **QR2**.

	HF	$+\delta$MP2	$+\delta$CCSD	$+\delta$CCSD(T)	NET
cc-pVDZ	−8.84	+2.14	−9.04	−1.02	[−16.77]
cc-pVTZ	−10.28	−2.96	−8.34	−1.66	[−23.24]
cc-pVQZ	−10.11	−4.68	−8.21	−1.83	[−24.83]
cc-pV5Z	−10.10	−5.43	−8.09	−1.88	[−25.50]
CBS LIMIT	[−10.12]	[−6.22]	[−7.96]	[−1.94]	[−26.22]

$\Delta H_{0K} = \Delta E_e + \Delta_{T(Q)} + \Delta_{CORE} + \Delta_{REL} + \Delta_{DBOC} + \Delta_{ZPVE}$

ΔH_{0K} = −26.22 + 0.199 + 0.095 + 0.425 − 0.089 + 3.293 = **−22.3**

Table A.16: Focal point table for **KHC**.

	HF	$+\delta$MP2	$+\delta$CCSD	$+\delta$CCSD(T)	NET
cc-pVDZ	−12.16	+13.33	−11.42	−0.84	[−11.10]
cc-pVTZ	−13.30	+10.97	−12.29	−1.20	[−15.82]
cc-pVQZ	−13.15	+10.14	−12.56	−1.30	[−16.87]
cc-pV5Z	−13.01	+9.82	−12.57	−1.32	[−17.09]
CBS LIMIT	[−12.92]	[+9.48]	[−12.58]	[−1.34]	[−17.37]

$\Delta H_{0K} = \Delta E_e + \Delta_{T(Q)} + \Delta_{CORE} + \Delta_{REL} + \Delta_{DBOC} + \Delta_{ZPVE}$

ΔH_{0K} = −17.37 + 0.144 − 0.071 + 0.295 − 0.069 + 1.149 = **−15.9**

Table A.17: Focal point table for Glyoxal + $^{\bullet}OH$.

	HF	$+\delta$MP2	$+\delta$CCSD	$+\delta$CCSD(T)	NET
cc-pVDZ	−59.26	+27.57	−11.64	+1.18	[−42.15]
cc-pVTZ	−60.10	+26.33	−12.51	+1.63	[−44.65]
cc-pVQZ	−60.66	+25.57	−12.62	+1.71	[−46.01]
cc-pV5Z	−60.75	+25.18	−12.53	+1.74	[−46.36]
CBS LIMIT	[−60.76]	[+24.78]	[−12.44]	[+1.77]	[−46.65]

$\Delta H_{0K} = \Delta E_e + \Delta_{T(Q)} + \Delta_{CORE} + \Delta_{REL} + \Delta_{DBOC} + \Delta_{ZPVE}$

ΔH_{0K} = −46.65 − 0.856 + 0.123 + 0.333 − 0.026 − 0.382 = **−47.5**

Table A.18: Focal point table for CH_2O +CO + $^{\bullet}$OH.

	HF	$+\delta$MP2	$+\delta$CCSD	$+\delta$CCSD(T)	NET
cc-pVDZ	−68.81	+34.69	−14.17	+1.81	[−46.48]
cc-pVTZ	−69.84	+36.31	−14.95	+2.57	[−45.90]
cc-pVQZ	−70.61	+36.48	−15.06	+2.80	[−46.39]
cc-pV5Z	−70.64	+36.40	−14.97	+2.88	[−46.32]
CBS LIMIT	[−70.57]	[+36.32]	[−14.88]	[+2.97]	[−46.16]

$$\Delta H_{0\mathrm{K}} = \Delta E_e + \Delta_{\mathrm{T(Q)}} + \Delta_{\mathrm{CORE}} + \Delta_{\mathrm{REL}} + \Delta_{\mathrm{DBOC}} + \Delta_{\mathrm{ZPVE}}$$

$$\Delta H_{0\mathrm{K}} = -46.16 - 0.858 + 0.497 + 0.167 + 0.005 - 3.788 = \mathbf{-50.1}$$

Table A.19: Focal point table for Ketene + $HO_2^{\bullet}$.

	HF	$+\delta$MP2	$+\delta$CCSD	$+\delta$CCSD(T)	NET
cc-pVDZ	−10.41	+17.38	−12.52	−0.30	[−5.84]
cc-pVTZ	−12.33	+15.53	−13.44	−0.49	[−10.73]
cc-pVQZ	−12.46	+14.80	−13.73	−0.54	[−11.93]
cc-pV5Z	−12.45	+14.47	−13.72	−0.55	[−12.25]
CBS LIMIT	[−12.43]	[+14.14]	[−13.72]	[−0.55]	[−12.56]

$$\Delta H_{0\mathrm{K}} = \Delta E_e + \Delta_{\mathrm{T(Q)}} + \Delta_{\mathrm{CORE}} + \Delta_{\mathrm{REL}} + \Delta_{\mathrm{DBOC}} + \Delta_{\mathrm{ZPVE}}$$

$$\Delta H_{0\mathrm{K}} = -12.56 + 0.022 - 0.072 + 0.296 - 0.053 - 0.245 = \mathbf{-12.6}$$

Appendix B

Acetonyl Radical + O_2 Potential Energy Surface

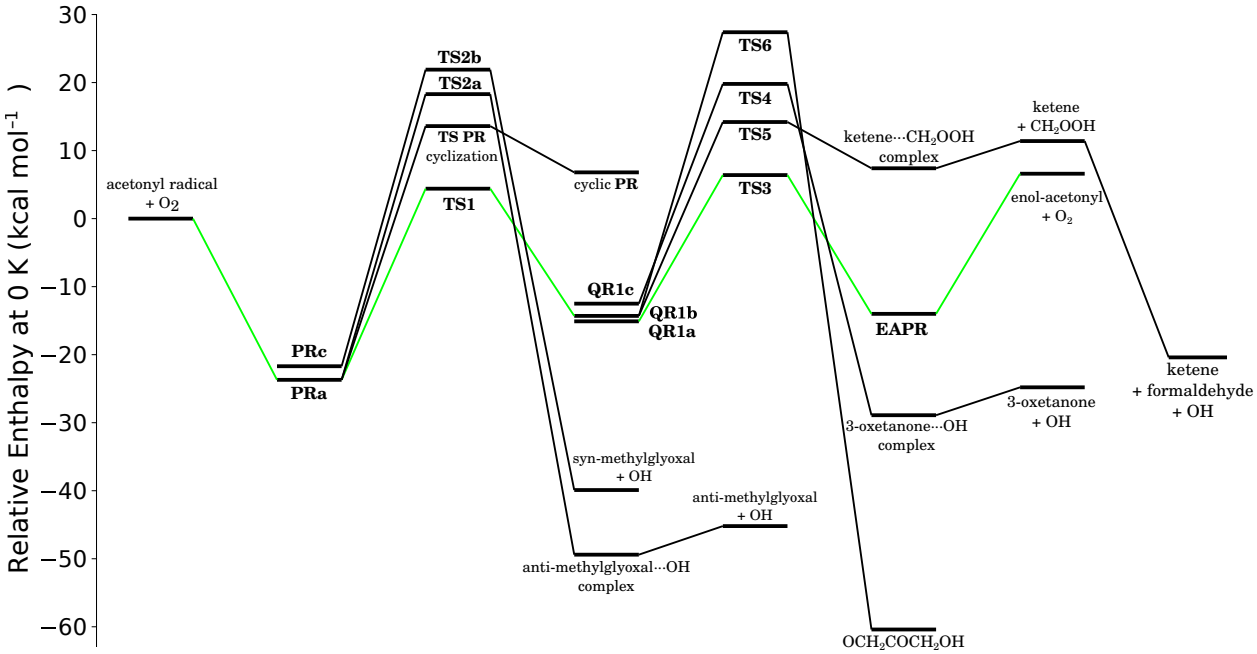

Figure B.1: Sketch of the potential energy surface for the acetonyl radical + O_2 reaction. For consistency, all of these stationary points are plotted based on structures and energies computed with the M06-2X/def2-TZVP method. Energies include a harmonic ZPVE correction at the same level of theory. Low-lying stationary points have been computed using more sophisticated methods, and these are shown in Figure 3.1 in the main text. The predicted minimum energy isomerization pathway of **PR** is shown in green.

Bibliography

(1) Schrödinger, E. *Phys. Rev.* **1926**, *28*, 1049–1070.

(2) Born, M.; Oppenheimer, R. *Annalen der Physik* **1927**, *389*, 457–484.

(3) Szabo, A.; Ostlund, N. S., *Modern Quantum Chemistry: Introduction to Advanced Electronic Structure Theory*; Courier Corporation: 2012.

(4) Pauli, W. *Z. Physik* **1925**, *31*, 765–783.

(5) Čížek, J. *J. Chem. Phys.* **1966**, *45*, 4256–4266.

(6) Lipkowitz, K. B.; Boyd, D. B., *Reviews in Computational Chemistry*; John Wiley & Sons: 2009.

(7) Raghavachari, K.; Trucks, G. W.; Pople, J. A.; Head-Gordon, M. *Chem. Phys. Lett.* **1989**, *157*, 479–483.

(8) East, A. L. L.; Allen, W. D. *J. Chem. Phys.* **1993**, *99*, 4638–4650.

(9) Császár, A. G.; Allen, W. D.; Schaefer, H. F. *J. Chem. Phys.* **1998**, *108*, 9751–9764.

(10) Dunning, T. H. *The Journal of Chemical Physics* **1989**, *90*, 1007–1023.

(11) Feller, D. *J. Chem. Phys.* **1992**, *96*, 6104–6114.

(12) Peterson, K. A.; Woon, D. E.; Dunning, T. H. *J. Chem. Phys.* **1994**, *100*, 7410–7415.

(13) Helgaker, T.; Klopper, W.; Koch, H.; Noga, J. *The Journal of Chemical Physics* **1997**, *106*, 9639–9646.

(14) Martin, J. M. L. *Chem. Phys. Lett.* **1996**, *259*, 669–678.

(15) Roos, B. O.; Taylor, P. R.; Sigbahn, P. E. M. *Chem. Phys.* **1980**, *48*, 157–173.

(16) Andersson, K.; Malmqvist, P. A.; Roos, B. O.; Sadlej, A. J.; Wolinski, K. *J. Phys. Chem.* **1990**, *94*, 5483–5488.

(17) Buenker, R. J.; Peyerimhoff, S. D. *Theoret. Chim. Acta* **1974**, *35*, 33–58.

(18) Hohenberg, P.; Kohn, W. *Phys. Rev.* **1964**, *136*, B864–B871.

(19) Kohn, W.; Sham, L. J. *Phys. Rev.* **1965**, *140*, A1133–A1138.

(20) Becke, A. D. *Phys. Rev. A* **1988**, *38*, 3098–3100.

(21) Lee, C.; Yang, W.; Parr, R. G. *Phys. Rev. B* **1988**, *37*, 785–789.

(22) Zhao, Y.; Truhlar, D. G. *Chem. Phys. Lett.* **2011**, *502*, 1–13.

(23) Perdew, J. P. *Phys. Rev. B* **1986**, *33*, 8822–8824.

(24) Vereecken, L.; Francisco, J. S. *Chem. Soc. Rev.* **2012**, *41*, 6259–6293.

(25) Zádor, J.; Taatjes, C. A.; Fernandes, R. X. *Prog. Energ. Combust.* **2011**, *37*, 371–421.

(26) Alam, M. S.; Rickard, A. R.; Camredon, M.; Wyche, K. P.; Carr, T.; Hornsby, K. E.; Monks, P. S.; Bloss, W. J. *J. Phys. Chem. A* **2013**, *117*, 12468–12483.

(27) Gutbrod, R.; Schindler, R. N.; Kraka, E.; Cremer, D. *Chem. Phys. Lett.* **1996**, *252*, 221–229.

(28) Johnson, D.; Marston, G. *Chem. Soc. Rev.* **2008**, *37*, 699.

(29) Kroll, J. H.; Donahue, N. M.; Cee, V. J.; Demerjian, K. L.; Anderson, J. G. *J. Am. Chem. Soc.* **2002**, *124*, 8518–8519.

(30) Zhang, D.; Zhang, R. *J. Am. Chem. Soc.* **2002**, *124*, 2692–2703.

(31) Zhang, D.; Lei, W.; Zhang, R. *Chem. Phys. Lett.* **2002**, *358*, 171–179.

(32) Atkinson, R. *Chem. Rev.* **1986**, *86*, 69–201.

(33) Gutbrod, R.; Kraka, E.; Schindler, R. N.; Cremer, D. *J. Am. Chem. Soc.* **1997**, *119*, 7330–7342.

(34) Liu, F.; Fang, Y.; Kumar, M.; Thompson, W. H.; Lester, M. I. *Phys. Chem. Chem. Phys.* **2015**, *17*, 20490–20494.

(35) Lorenz, K.; Zellner, R. *Berich. Bunsen. Gesell.* **1984**, *88*, 1228–1231.

(36) Zhu, L.; Johnston, G. *J. Phys. Chem.* **1995**, *99*, 15114–15119.

(37) Schmidt, V.; Zhu, G. Y.; Becker, K. H.; Fink, E. H. *Berich. Bunsen. Gesell.* **1985**, *89*, 321–322.

(38) Leonori, F.; Balucani, N.; Nevrly, V.; Bergeat, A.; Falcinelli, S.; Vanuzzo, G.; Casavecchia, P.; Cavallotti, C. *J. Phys. Chem. C* **2015**, *119*, 14632–14652.

(39) Barnhard, K. I.; Santiago, A.; He, M.; Asmar, F.; Weiner, B. R. *Chem. Phys. Lett.* **1991**, *178*, 150–156.

(40) Lam, C.-S.; Adams, J. D.; Butler, L. J. *J. Phys. Chem. A* **2016**, *120*, 2521–2536.

(41) Gutman, D.; Nelson, H. H. *J. Phys. Chem.* **1983**, *87*, 3902–3905.

(42) Lorenz, K.; Rhasa, D.; Zellner, R.; Fritz, B. *Berich. Bunsen. Gesell.* **1985**, *89*, 341–342.

(43) Maranzana, A.; Barker, J. R.; Tonachini, G. *J. Phys. Chem. A* **2008**, *112*, 3666–3675.

(44) Inoue, G.; Akimoto, H. *J. Chem. Phys.* **1981**, *74*, 425–433.

(45) Dupuis, M.; Wendoloski, J. J.; Lester, W. A. *J. Chem. Phys.* **1982**, *76*, 488–492.

(46) Jacox, M. E. *Chem. Phys.* **1982**, *69*, 407–422.

(47) Glowacki, D. R.; Pilling, M. J. *ChemPhysChem* **2010**, *11*, 3836–3843.

(48) Orlando, J. J.; Tyndall, G. S. *Chem. Soc. Rev.* **2012**, *41*, 6294.

(49) Finlayson-Pitts, B.; Pitts, J. *Air & Waste* **1993**, *43*, 1091–1100.

(50) Kuwata, K. T. In *PATAI'S Chemistry of Functional Groups*, Rappoport, Z., Ed.; John Wiley & Sons, Ltd: Chichester, UK, 2014, pp 1–50.

(51) Delbos, E.; Fittschen, C.; Hippler, H.; Krasteva, N.; Olzmann, M.; Viskolcz, B. *J. Phys. Chem. A* **2006**, *110*, 3238–3245.

(52) Lee, J.; Bozzelli, J. W. *J. Phys. Chem. A* **2003**, *107*, 3778–3791.

(53) Kuwata, K. T.; Templeton, K. L.; Hasson, A. S. *J. Phys. Chem. A* **2003**, *107*, 11525–11532.

(54) Kuwata, K. T.; Hasson, A. S.; Dickinson, R. V.; Petersen, E. B.; Valin, L. C. *J. Phys. Chem. A* **2005**, *109*, 2514–2524.

(55) Maranzana, A.; Ghigo, G.; Tonachini, G.; Barker, J. R. *J. Phys. Chem. A* **2008**, *112*, 3656–3665.

(56) Oguchi, T.; Miyoshi, A.; Koshi, M.; Matsui, H.; Washida, N. *J. Phys. Chem. A* **2001**, *105*, 378–382.

(57) CFOUR, Coupled-Cluster techniques for Computational Chemistry, a quantum-chemical program package by J.F. Stanton, J. Gauss, L. Cheng, M.E. Harding, D.A. Matthews, P.G. Szalay with contributions from A.A. Auer, R.J. Bartlett, U. Benedikt, C. Berger, D.E. Bernholdt, Y.J. Bomble, O. Christiansen, F. Engel, R. Faber, M. Heckert, O. Heun, C. Huber,

T.-C. Jagau, D. Jonsson, J. Jusélius, K. Klein, W.J. Lauderdale, F. Lipparini, T. Metzroth, L.A. Mück, D.P. O'Neill, D.R. Price, E. Prochnow, C. Puzzarini, K. Ruud, F. Schiffmann, W. Schwalbach, C. Simmons, S. Stopkowicz, A. Tajti, J. Vázquez, F. Wang, J.D. Watts and the integral packages MOLECULE (J. Almlöf and P.R. Taylor), PROPS (P.R. Taylor), ABACUS (T. Helgaker, H.J. Aa. Jensen, P. Jørgensen, and J. Olsen), and ECP routines by A. V. Mitin and C. van Wüllen. For the current version, see http://www.cfour.de.

(58) Harding, M. E.; Metzroth, T.; Gauss, J.; Auer, A. A. *J. Chem. Theory Comput.* **2008**, *4*, 64–74.

(59) Almlöf, J.; Taylor, P. R. *J. Chem. Phys.* **1987**, *86*, 4070–4077.

(60) Neese, F.; Valeev, E. F. *J. Chem. Theory Comput.* **2011**, *7*, 33–43.

(61) Gauss, J.; Lauderdale, W. J.; Stanton, J. F.; Watts, J. D.; Bartlett, R. J. *Chem. Phys. Lett.* **1991**, *182*, 207–215.

(62) Watts, J. D.; Gauss, J.; Bartlett, R. J. *J. Chem. Phys.* **1993**, *98*, 8718–8733.

(63) Schmidt, M. W.; Baldridge, K. K.; Boatz, J. A.; Elbert, S. T.; Gordon, M. S.; Jensen, J. H.; Koseki, S.; Matsunaga, N.; Nguyen, K. A.; Su, S.; Windus, T. L.; Dupuis, M.; Montgomery, J. A. *J. Comput. Chem* **1993**, *14*, 1347–1363.

(64) M. W. Schmidt and M. S. Gordon, in Theory and Applications of Computational Chemistry: The First Forty Years, edited by C. E. Dykstra, G. Frenking, K. S. Kim and G. E. Scuseria (Elsevier, Amsterdam, 2005, pp. 1167–1189).

(65) Schuurman, M. S.; Muir, S. R.; Allen, W. D.; Schaefer, H. F. *J. Chem. Phys.* **2004**, *120*, 11586–11599.

(66) Gonzales, J. M.; Pak, C.; Cox, R. S.; Allen, W. D.; Schaefer, H. F.; Császár, A. G.; Tarczay, G. *Chem.-Eur. J.* **2003**, *9*, 2173–2192.

(67) Feller, D. *The Journal of Chemical Physics* **1993**, *98*, 7059–7071.

(68) MOLPRO is a package of ab initio programs written by H.-J. Werner, P. J. Knowles, G. Knizia, F. R. Manby, M. Schütz, P. Celani, W. Györffy, D. Kats, T. Korona, R. Lindh, A. Mitrushenkov, G. Rauhut, K. R. Shamasundar, T. B. Adler, R. D. Amos, A. Bernhardsson, A. Berning, D. L. Cooper, M. J. O. Deegan, A. J. Dobbyn, F. Eckert, E. Goll, C. Hampel, A. Hesselmann, G. Hetzer, T. Hrenar, G. Jansen, C. Köppl, Y. Liu, A. W. Lloyd, R. A. Mata, A. J. May, S. J. McNicholas, W. Meyer, M. E. Mura, A. Nicklaß, D. P. O'Neill, P. Palmieri, D. Peng, K. Pflüger, R. Pitzer, M. Reiher, T. Shiozaki, H. Stoll, A. J. Stone, R. Tarroni, T. Thorsteinsson, M. Wang.

(69) Stopkowicz, S.; Gauss, J. *J. Chem. Phys.* **2008**, *129*, 164119.

(70) Martin, J. M. *Mol. Phys.* **2014**, *112*, 785–793.

(71) MRCC, a quantum chemical program suite written by M. Kállay, Z. Rolik, J. Csontos, P. Nagy, G. Samu, D. Mester, J. Csóka, I. Ladjánszki, L. Szegedy, B. Ladóczki, K. Petrov, M. Farkas, and B. Hégely. See also Z. Rolik, L. Szegedy, I. Ladjánszki, B. Ladóczki, and M. Kállay, J. Chem. Phys. 139, 094105 (2013), as well as: www.mrcc.hu.

(72) Knowles, P. J.; Werner, H.-J. *Chem. Phys. Lett.* **1985**, *115*, 259–267.

(73) Werner, H.; Knowles, P. J. *J. Chem. Phys.* **1985**, *82*, 5053–5063.

(74) Celani, P.; Werner, H.-J. *J. Chem. Phys.* **2000**, *112*, 5546–5557.

(75) Lindh, R. *Theor. Chim. Acta.* **1993**, *85*, 423–440.

(76) Celani, P.; Werner, H.-J. *J. Chem. Phys.* **2003**, *119*, 5044–5057.

(77) Eckert, F.; Pulay, P.; Werner, H.-J. *J. Comput. Chem* **1997**, *18*, 1473–1483.

(78) Goldsmith, C. F.; Harding, L. B.; Georgievskii, Y.; Miller, J. A.; Klippenstein, S. J. *J. Phys. Chem. A* **2015**, *119*, 7766–7779.

(79) Moradi, C. P.; Morrison, A. M.; Klippenstein, S. J.; Goldsmith, C. F.; Douberly, G. E. *J. Phys. Chem. A* **2013**, *117*, 13626–13635.

(80) Knowles, P. J.; Hampel, C.; Werner, H. *J. Chem. Phys.* **1993**, *99*, 5219–5227.

(81) Werner, H.; Knowles, P. J. *J. Chem. Phys.* **1988**, *89*, 5803–5814.

(82) Knowles, P. J.; Werner, H.-J. *Chem. Phys. Lett.* **1988**, *145*, 514–522.

(83) Meek, G. A.; Levine, B. G. *J. Chem. Phys.* **2016**, *144*, 184109.

(84) Rienstra-Kiracofe, J. C.; Allen, W. D.; Schaefer, H. F. *J. Phys. Chem. A* **2000**, *104*, 9823–9840.

(85) Moore, K. B.; Turney, J. M.; Schaefer, H. F. *J. Chem. Phys.* **2017**, *146*, 194304.

(86) Bartlett, M. A.; Liang, T.; Pu, L.; Schaefer, H. F.; Allen, W. D. *J. Chem. Phys.* **2018**, Submitted.

(87) Singh, H. B.; O'Hara, D.; Herlth, D.; Sachse, W.; Blake, D. R.; Bradshaw, J. D.; Kanakidou, M.; Crutzen, P. J. *J. Geophys. Res-Atmos.* **1994**, *99*, 1805–1819.

(88) Singh, H. B.; Kanakidou, M.; Crutzen, P. J.; Jacob, D. J. *Nature* **1995**, *378*, 50–54.

(89) Wennberg, P. O. et al. *Science* **1998**, *279*, 49–53.

(90) Wollenhaupt, M.; Carl, S. A.; Horowitz, A.; Crowley, J. N. *J. Phys. Chem. A* **2000**, *104*, 2695–2705.

(91) Vasvári, G.; Szilágyi, I.; Bencsura, Á.; Dóbé, S.; Bérces, T.; Henon, E.; Canneaux, S.; Bohr, F. *Phys. Chem. Chem. Phys.* **2001**, *3*, 551–555.

(92) Lester, M. I.; Klippenstein, S. J. *Acc. Chem. Res.* **2018**, *51*, 978–985.

(93) Washida, N.; Inomata, S.; Furubayashi, M. *J. Phys. Chem. A* **1998**, *102*, 7924–7930.

(94) Quandt, R.; Min, Z.; Wang, X.; Bersohn, R. *J. Phys. Chem. A* **1998**, *102*, 60–64.

(95) Balucani, N.; Leonori, F.; Casavecchia, P.; Fu, B.; Bowman, J. M. *J. Phys. Chem. A* **2015**, *119*, 12498–12511.

(96) Imrik, K.; Farkas, E.; Vasvári, G.; Szilágyi, I.; Sarzyński, D.; Dóbé, S.; Bérces, T.; Márta, F. *Phys. Chem. Chem. Phys.* **2004**, *6*, 3958–3968.

(97) Solly, R. K.; Golden, D. M.; Benson, S. W. *Int. J. Chem. Kinet.* **1970**, *2*, 11–21.

(98) King, K. D.; Golden, D. M.; Benson, S. W. *J. Am. Chem. Soc.* **1970**, *92*, 5541–5546.

(99) Bouchoux, G.; Chamot-Rooke, J.; Leblanc, D.; Mourgues, P.; Sablier, M. *ChemPhysChem* **2001**, *2*, 235–241.

(100) Espinosa-García, J.; Márquez, A.; Dóbé, S. *Chem. Phys. Lett.* **2003**, *373*, 350–356.

(101) El-Nahas, A. M.; Bozzelli, J. W.; Simmie, J. M.; Navarro, M. V.; Black, G.; Curran, H. J. *J. Phys. Chem. A* **2006**, *110*, 13618–13623.

(102) Cox, R. A.; Munk, J.; Nielsen, O. J.; Pagsberg, P.; Ratajczak, E. *Chem. Phys. Lett.* **1990**, *173*, 206–210.

(103) Hassouna, M.; Delbos, E.; Devolder, P.; Viskolcz, B.; Fittschen, C. *J. Phys. Chem. A* **2006**, *110*, 6667–6672.

(104) Kovács, G.; Zádor, J.; Farkas, E.; Nádasdi, R.; Szilágyi, I.; Dóbé, S.; Bérces, T.; Márta, F.; Lendvay, G. *Phys. Chem. Chem. Phys.* **2007**, *9*, 4142–4154.

(105) Tyndall, G. S.; Cox, R. A.; Granier, C.; Lesclaux, R.; Moortgat, G. K.; Pilling, M. J.; Ravishankara, A. R.; Wallington, T. J. *J. Geophys. Res-Atmos.* **2001**, *106*, 12157–12182.

(106) Kuwata, K. T. In *PATAI'S Chemistry of Functional Groups*, Rappoport, Z., Ed.; John Wiley & Sons, Ltd: Chichester, UK, 2014, pp 1–50.

(107) Savee, J. D.; Papajak, E.; Rotavera, B.; Huang, H.; Eskola, A. J.; Welz, O.; Sheps, L.; Taatjes, C. A.; Zádor, J.; Osborn, D. L. *Science* **2015**, *347*, 643–646.

(108) Bridier, I.; Veyret, B.; Lesclaux, R.; Jenkin, M. E. *J. Chem. Soc., Faraday Trans.* **1993**, *89*, 2993–2997.

(109) Sehested, J.; Christensen, L. K.; Nielsen, O. J.; Bilde, M.; Wallington, T. J.; Schneider, W. F.; Orlando, J. J.; Tyndall, G. S. *Int. J. Chem. Kinet.* **1998**, *30*, 475–489.

(110) Hasson, A. S.; Tyndall, G. S.; Orlando, J. J. *J. Phys. Chem. A* **2004**, *108*, 5979–5989.

(111) Dillon, T. J.; Crowley, J. N. *Atmos. Chem. Phys.* **2008**, *8*, 4877–4889.

(112) El-Nahas, A. M.; Simmie, J. M.; Navarro, M. V.; Bozzelli, J. W.; Black, G.; Curran, H. J. *Phys. Chem. Chem. Phys.* **2008**, *10*, 7139–7149.

(113) Jenkin, M. E.; Hurley, M. D.; Wallington, T. J. *Phys. Chem. Chem. Phys.* **2008**, *10*, 4274–4280.

(114) Emricha, M.; Warneck, P. *Z. Naturforsch Pt. A.* **2014**, *58*, 429–433.

(115) Weidman, J. D.; Allen, R. T.; Moore, K. B.; Schaefer, H. F. *J. Chem. Phys.* **2018**, *148*, 184308.

(116) Davis, M. M.; Weidman, J. D.; Abbott, A. S.; Douberly, G. E.; Turney, J. M.; Schaefer, H. F. *J. Chem. Phys.* **2019**, *151*, 124302.

(117) Neese, F. *WIRES Comput. Mol. Sci.* **2012**, *2*, 73–78.

(118) Knowles, P. J.; Hampel, C.; Werner, H.-J. *J. Chem. Phys.* **2000**, *112*, 3106–3107.

(119) Verma, P.; Derricotte, W. D.; Evangelista, F. A. *J. Chem. Theory Comput.* **2016**, *12*, 144–156.

(120) Parrish, R. M. et al. *J. Chem. Theory Comput.* **2017**, *13*, 3185–3197.

(121) Wagner, A. F.; Slagle, I. R.; Sarzynski, D.; Gutman, D. *J. Phys. Chem.* **1990**, *94*, 1853–1868.

(122) Wilke, J. J.; Allen, W. D.; Schaefer, H. F. *J. Chem. Phys.* **2008**, *128*, 074308.

(123) Goldsmith, C. F.; Green, W. H.; Klippenstein, S. J. *J. Phys. Chem. A* **2012**, *116*, 3325–3346.

(124) Anglada, J. M.; Crehuet, R.; Francisco, J. S. *Chem-Eur. J.* **2016**, *22*, 18092–18100.

(125) Du Toit, J.; van Sittert, C.; Vosloo, H. *J. Organomet. Chem.* **2013**, *738*, 76–91.

(126) Strassner, T. In *Metal Carbenes in Organic Synthesis*; Springer Berlin Heidelberg: Berlin, Heidelberg, 2004; Vol. 13, pp 1–20.

(127) Fischer, E. O.; Maasböl, A. *Angew. Chem. Int. Edit.* **1964**, *3*, 580–581.

(128) Schrock, R. R. *J. Am. Chem. Soc.* **1975**, *97*, 6577–6578.

(129) Frenking, G.; Fröhlich, N. *Chem. Rev.* **2000**, *100*, 717–774.

(130) Spangler, D.; Wendoloski, J. J.; Dupuis, M.; Chen, M. M. L.; Schaefer, H. F. *J. Am. Chem. Soc.* **1981**, *103*, 3985–3990.

(131) Davidson, E. R.; Kunze, K. L.; Machado, F. B. C.; Chakravorty, S. J. *Accounts Chem. Res.* **1993**, *26*, 628–635.

(132) Abel, E. W.; Stone, F. G. A. *Q. Rev. Chem. Soc.* **1969**, *23*, 325–371.

(133) Abel, E. W.; Stone, F. G. A. *Q. Rev. Chem. Soc.* **1970**, *24*, 498–552.

(134) Werner, H. *Angew. Chem. Int. Edit.* **1990**, *29*, 1077–1089.

(135) Jonas, V.; Thiel, W. *J. Chem. Phys.* **1995**, *102*, 8474–8484.

(136) Dötz, K. H.; Stendel, J. *Chem. Rev.* **2009**, *109*, 3227–3274.

(137) Herndon, J. W. *Coordin. Chem. Rev.* **2016**, *329*, 53–162.

(138) Künzi, S. A.; Sarria Toro, J. M.; den Hartog, T.; Chen, P. *Angew. Chem. Int. Edit.* **2015**, *54*, 10670–10674.

(139) Levine, D. S.; Tilley, T. D.; Andersen, R. A. *Organometallics* **2017**, *36*, 80–88.

(140) Wu, P.; Yap, G. P. A.; Theopold, K. H. *J. Am. Chem. Soc.* **2018**, *140*, 7088–7091.

(141) Stevens, A. E.; Beauchamp, J. L. *J. Am. Chem. Soc.* **1979**, *101*, 6449–6450.

(142) Stevens, A. E. Ph.D. Thesis, California Institute of Technology, 1981.

(143) Armentrout, P. B.; Halle, L. F.; Beauchamp, J. L. *J. Am. Chem. Soc.* **1981**, *103*, 6501–6502.

(144) Taylor, T. E.; Hall, M. B. *J. Am. Chem. Soc.* **1984**, *106*, 1576–1584.

(145) Márquez, A.; Fernández Sanz, J. *J. Am. Chem. Soc.* **1992**, *114*, 2903–2909.

(146) Jacobsen, H.; Schreckenbach, G.; Ziegler, T. *J. Phys. Chem.* **1994**, *98*, 11406–11410.

(147) Jacobsen, H.; Ziegler, T. *Organometallics* **1995**, *14*, 224–230.

(148) Jacobsen, H.; Ziegler, T. *Inorg. Chem.* **1996**, *35*, 775–783.

(149) Ehlers, A. W.; Dapprich, S.; Vyboishchikov, S. F.; Frenking, G. *Organometallics* **1996**, *15*, 105–117.

(150) Vyboishchikov, S. F.; Frenking, G. *Chem-Eur. J.* **1998**, *4*, 1428–1438.

(151) Chen, Y.; Petz, W.; Frenking, G. *Organometallics* **2000**, *19*, 2698–2706.

(152) Chen, Y.; Hartmann, M.; Frenking, G. *Z. Anorg. Allg. Chem.* **2001**, *627*, 985–998.

(153) Cases, M.; Frenking, G.; Duran, M.; Solà, M. *Organometallics* **2002**, *21*, 4182–4191.

(154) Frenking, G.; Solà, M.; Vyboishchikov, S. F. *J. Organomet. Chem.* **2005**, *690*, 6178–6204.

(155) Van Wüllen, C. *J. Comput. Chem.* **1997**, *18*, 1985–1992.

(156) Poater, J.; Cases, M.; Fradera, X.; Duran, M.; Solà, M. *Chem. Phys.* **2003**, *294*, 129–139.

(157) Barcs, B.; Kollár, L.; Kégl, T. *Organometallics* **2012**, *31*, 8082–8097.

(158) Kalescky, R.; Kraka, E.; Cremer, D. *Inorg. Chem.* **2014**, *53*, 478–495.

(159) Bender, C. F.; Schaefer, H. F. *J. Am. Chem. Soc.* **1970**, *92*, 4984–4985.

(160) Cramer, C. J.; Truhlar, D. G. *Phys. Chem. Chem. Phys.* **2009**, *11*, 10757–10816.

(161) Minenkov, Y.; Singstad, A.; Occhipinti, G.; Jensen, V. R. *Dalton T.* **2012**, *41*, 5526–5541.

(162) Zhao, Y.; Truhlar, D. G. *J. Chem. Phys.* **2006**, *125*, 194101.

(163) Chai, J.-D.; Head-Gordon, M. *J. Chem. Phys.* **2008**, *128*, 084106.

(164) Chai, J.-D.; Head-Gordon, M. *Phys. Chem. Chem. Phys.* **2008**, *10*, 6615–6620.

(165) Narendrapurapu, B. S.; Richardson, N. A.; Copan, A. V.; Estep, M. L.; Yang, Z.; Schaefer, H. F. *J. Chem. Theory Comput.* **2013**, *9*, 2930–2938.

(166) Peterson, K. A.; Figgen, D.; Dolg, M.; Stoll, H. *J. Chem. Phys.* **2007**, *126*, 124101.

(167) Figgen, D.; Peterson, K. A.; Dolg, M.; Stoll, H. *J. Chem. Phys.* **2009**, *130*, 164108.

(168) Neese, F. *WIRES Comput. Mol. Sci.* **2012**, *2*, 73–78.

(169) Wheeler, S. E.; Houk, K. N. *J. Chem. Theory Comput.* **2010**, *6*, 395–404.

(170) Neese, F. *J. Comput. Chem.* **2003**, *24*, 1740–1747.

(171) Neese, F.; Wennmohs, F.; Hansen, A.; Becker, U. *Chem. Phys.* **2009**, *356*, 98–109.

(172) Tolman, C. A. *J. Am. Chem. Soc.* **1970**, *92*, 2953–2956.